DISSERTATION

EFFECT OF LARGE-SCALE ANISOTROPY ON THE SMALL-SCALE STRUCTURE OF TURBULENCE

Submitted by

Khandakar Niaz Morshed

Department of Mechanical Engineering

In partial fulfillment of the requirements

For the Degree of Doctor of Philosophy

Colorado State University

Fort Collins, Colorado

Fall 2014

Doctoral Committee:

Advisor: Lakshmi Prasad Dasi

Allan Kirkpatrick
Xinfeng Gao
Subhas Karan Venayagamoorthy

ABSTRACT

EFFECT OF LARGE-SCALE ANISOTROPY ON THE SMALL-SCALE STRUCTURE OF TURBULENCE

Even though the small-scale structure of turbulence has been hypothesized to be locally isotropic with universal properties, numerous studies document the departure from local isotropy and universality in the presence of strong mean shear (or large-scale anisotropy). The goal of this work is to elucidate the effects of strong shear on the small-scale structure with emphasis on the physical mechanism through which mean shear deviates local structure from isotropy. Two dimensional time-resolved particle image velocimetry (PIV) experiments were performed in a stationary turbulent flow past a backward facing step at Reynolds numbers 13600 and 5500 based on the maximum velocity and step height. Large-scale anisotropic properties of the flow along with local turbulence characteristics were quantified in detail. Special points of interest distributed within the measurement domain for varying large-scale anisotropic characteristics were probed to analyze small-scale structure. Results show that velocity structure functions and their scaling exponents systematically align with the principal directions of deformation of the mean flow field. Furthermore, the probability density function (PDF) of the instantaneous dissipative scales indicate a potentially universal mechanism of how mean shear affects the distribution of dissipative scales captured through a local Reynolds number based on mean shear and dissipation rate. PDFs of the instantaneous dissipative scales in all directions demonstrate that mean shear strength and local principal axis directions dictate the behavior of structure functions, correlation functions, thereby influencing the dissipative scale PDFs in a directionally dependent manner.

ACKNOWLEDGEMENTS

I would like to express my gratitude to Dr. Lakshmi Prasad Dasi, my advisor, for his outstanding scholarly directions and remarkable coaching effort throughout my graduate studies. I also express my appreciations to my committee members Dr. Subhas Karan Venayagamoorthy, Dr. Allan Kirkpatrick and Dr. Xinfeng Gao for their time and guidance, that helped me to enrich the dissertation work. Special thanks to Efadul Haq, patiently read my dissertation and recommended linguistic and grammatical corrections.

I acknowledge the support from my fellow lab members at Cardio-vascular and bio-fluid mechanics laboratory, in particular Mike Gogarty for his support and exceptional ideas during my experimental setup fabrication, Brennan Johnson for his effort to teach me MATLAB, Marcio Forleo for helping me with PIV experiments.

Finally, to the three girls Maira Morshed, Zaina Morshed and Sultana Shanta for their sacrifice during the tenure of my PhD studentship.

TABLE OF CONTENTS

LIST OF TABLES

LIST OF FIGURES

LIST OF SYMBOLS

α= direction vector

β=direction vector

$\zeta_{\alpha\beta}$= logarithmic derivative of structure function

ρ = density of fluid

μ = dynamic viscosity of fluid

τ_0= time scale for largest eddy

τ_η= Kolmogorov time scale

λ = Taylor micro-scale

λ_f = Longitudinal Taylor micro-scale

λ_g = transverse Taylor micro-scale

Λ = lacunarity

ε = turbulent kinetic energy dissipation

$< \varepsilon >$ = mean turbulent kinetic energy dissipation rate

ε_r= local average dissipation rate

η = instantaneous fluctuation dissipation scale

η_K = Kolmogorov length scale

η_0 = Normalization parameter ($\eta_0 = LRe_L^{-0.72}$)

η_{peak} = Peak location of $Q(\eta)$ distribution

ν = kinematic viscosity of fluid

$\delta_\eta u = |u(x + \eta) - u(x)|$ = longitudinal velocity increment

σ_U = standard deviation of streamwise velocity

σ_V = standard deviation of wall normal velocity

b = width of the channel

D = hydraulic diameter as $2bH/(b+H)$

d = diameter of the pipe

e_1= unit vector in principal axis direction (stretch)

e_2= unit vector in principal axis direction (contraction)

F_U= flatness factor as $\langle u^4 \rangle / \langle u^2 \rangle^2$

H = inlet height of the channel

h = step height of backward facing step

i= unit vector in x direction

j= unit vector in y direction

k = Turbulent kinetic energy

L= integral length scale

$L_{\varepsilon,S}$= length scale based on energy dissipation rate and mean shear

$L_{S,\nu}$= length scale based on mean shear and kinematic viscosity

l_{DI}= length scale between dissipation range and inertial sub-range ($\eta < l_{DI} < r$)

l_{EI}= length scale between integral sub-range and integral length scale ($r < l_{EI} < L$)

l_0= length scale for the largest eddy

P = pressure

p = fluctuating pressure

$Q(\eta)$ = probability density function of η

$Q(\eta/\eta_0)$ = probability density function of η normalized by η_0

Re= Reynolds number

Re_τ = Reynolds number based on shear velocity

Re_η = Reynolds number based on Kolmogorov length scale

Re_λ = Taylor Reynolds number

Re_D = Reynolds number based on hydraulic diameter

Re_H= Reynolds number based on inlet height

Re_h= Reynolds number based on step height

Re_L = Reynolds number based on integral length scale

Re_S = Reynolds number based on mean shear dissipation rate

r = inertial sub-range

r= separation distance (also r_1, r_2, r_3, r_4)

S=Mean shear

T_L=turbulent time scale

U = velocity

U = streamwise velocity

U_0 = Maximum free stream velocity

U_i = mean velocity component

$< U_i >$ = ensemble average of mean velocity component

u_i = fluctuation velocity component of mean velocity

u_r= velocity difference between two position separated by r distance as $u(x + r) - u(x)$

V = wall normal velocity

Δx = spatial grid distance

y^+= distance from the wall (local Reynolds number)

Abbreviations:

2D= two dimensional

AR = aspect ratio (*b/H*)

CCD= charge-coupled device

CDF= cumulative density function

DNS=direct numerical simulations

ER = expansion ratio as *(H+h)/H*

HIT = homogeneous isotropic turbulence

IHAT=inhomogeneous anisotropic turbulence

K41= Kolmogorov hypothesis proposed in 1941

K62= Kolmogorov "refined similarity hypothesis" proposed in 1962

LDV= Laser Doppler velocimetry

PDFs = probability density functions

PIV = particle image velocimetry

PTV= particle tracking velocity

RSH= refined similarity hypothesis (also known as "K62")

SF = structure function

SO(2) = special orthogonal decomposition of structure function in two dimensions

SO(3) = special orthogonal decomposition of structure function in three dimensions

Chapter 1

INTRODUCTION

1.1 Introduction

Turbulent flow is present everywhere, in our everyday life we get the opportunity to observe turbulent flows i.e. smoke from the chimney, waterfalls, flow around aircraft, flow around building etc. Turbulence can happen both in internal flows (i.e. diffusers, combustion chambers) and external flows (i.e. flow around aerofoil, atmospheric flows)(Khandakar Niaz Morshed, 2010; Khandakar Niaz Morshed, Rahman, Molina, & Ahmed, 2013). Leonardo da Vinci depicted the details of turbulence by a realistic sketch around five hundred years ago. But it has been only hundred years since scientist seriously started thinking about the fascinating complexity of turbulent flows. Till today the "problem of turbulence" remains unanswered in classical physics. Understanding of turbulent flow is also very important for engineers, as turbulent flows are present in most of the engineering applications ranging from air fuel mixtures in engines cylinders, boilers & furnaces, flow through pipes, pumps, compressors, flow around airplanes, automobiles, marine vessels. From an engineering perspective the goal is to understand the nature of turbulence, predict the nature of the turbulence and control it to obtain maximum benefit. From a physical standpoint some interesting questions are: is there any universal small-scales structure for turbulent flows? Is there any boundary effect on the local turbulent structures? Is turbulence independent of the nature of the fluid or geometry (i.e. large-scale) of the problem? These questions remain unanswered in turbulence research and have become exciting research topics for engineers, physicists and

mathematicians with the ultimate goal of developing robust turbulence modeling approaches to tackle problems in energy (e.g. fuel efficiency) as well as healthcare (e.g. better medical devices such as heart valves.

In this study, we ask the question: what happens to the local structure in a strong shear zone? Given that kinematics of shear is fundamentally anisotropic with principal axis representing pure stretching and contraction of fluid elements (with no shear in these directions), how would the structure functions behave along these directions? Are the impacts of anisotropy different at different scales and different directions? To address these questions, we utilize a classical anisotropic turbulent flow presented by the flow past the backward facing step. The intense shear layer introduced into the turbulent channel flow is an ideal problem to probe the impacts of non-monotonic spatial anisotropy. Given that most previous studies investigating the small-scale structure of anisotropic flows limited their observations to cases where there was at least one direction of homogeneity, we believe that the complex non-monotonic and inhomogeneous field downstream of the backward facing step provides an ideal test bed to address the mechanistic questions that we have posed.

1.2 Hypothesis

The overall hypothesis is that large-scale shear fundamentally influences the small-scale even within the dissipative regions of the scale distribution. To test the influence of large-scale shear the following tasks will be addressed in this dissertation:

Task 1: Characterize structure function effects in the dissipative and non-dissipative regions for varying local mean shear strength.

Task 2: Characterize the behavior of local energy dissipation rate signal and the fluctuating dissipative scale probability density functions for varying local mean shear strength

Task 3: Relate the principal deformation directions to the anisotropic characteristics of structure functions and two point correlation functions for varying local mean shear strength

Task 4: Characterize local principal deformation properties to the local dissipative scales in all directions and their probability density function.

Chapter 2

LITERATURE REVIEW

Physicists, engineers and mathematicians are fascinated by the interesting nature of turbulence, and sense a huge challenge to solve the "unsolved" nature of turbulence. Since the inception of Navier-Stokes equations, a considerable extent of research has been conducted on turbulence over the last 150 years. Researchers have contributed to the knowledge base of turbulence by performing numerical studies, experimental studies and theoretical research. This chapter is organized to give a brief history on turbulence research covering from "classical era" (until the 1960s) to "modern era". This literature review will solely focus on the large-scale anisotropy of turbulent flows, small-scale structure of turbulent flows and dissipative scales in turbulent flows.

2.1 Turbulence research in "classical era"

Osborne Reynolds was the first to distinguish between laminar and turbulent flow, conducting his famous pipe-flow experiment (Reynolds, 1883, 1895). In his experiment he injected dye streak into the center of a flow through pipe while the flow transitioned from laminar to turbulent. From his experiment he proposed a non-dimensional number, widely known as Reynolds number, and depending upon this non-dimensional number flow can be categorized. Reynolds number is denote by *Re*,

$$Re = \frac{\rho U d}{\mu} \tag{2.1}$$

Where ρ = density of fluid, U = velocity (typically average velocity), d = diameter of the pipe (characteristics length) and μ = dynamic viscosity of fluid. Reynolds observed that in his pipe-flow experiment when the *Re* is less than 2300 the fluid velocity does not change with time and streamlines remain parallel to the axis of the pipe. And dye that was injected at center of the pipe keep the streak long with little increasing diameter at the downstream. This flow is known as laminar flow. On the other hand, when the Re is more than 4000 the flow is turbulent. The dye streak is jiggled by the turbulent motion. Dye eventually mixes with the water and is no longer visible in the downstream. This mixing phenomenon is very important in turbulent flows. He also noticed that when inlet disturbance is minimized flow remains laminar up to Re ~ 13,000. Reynolds introduces statistical methods in fluid turbulence by splitting the fluid velocity into fluctuating velocity and mean velocity. He also identified the non-linear terms in Navier-Stokes equations, now widely known as "Reynolds stress". Reynolds equations created "closure problem" in turbulent research. Even though Navier-Stokes equations are closed but incorporated with Reynolds equations, number of unknowns is more than number of equations. One has to make smart assumptions to equal the number of unknowns and number of equations.

$$U_i = < U_i > + u_i \tag{2.2}$$

$$P = < P > + p \tag{2.3}$$

$$\frac{\partial < U_i >}{\partial t} + < U_j > \frac{\partial < U_i >}{\partial x_j} = -\frac{1}{\rho}\frac{\partial < P >}{\partial x_i} + \frac{\partial}{\partial x_j}\left(\nu \frac{\partial < U_j >}{\partial x_j} - < u_i u_j >\right) \tag{2.4}$$

Equation 2.2 and 2.3 shows mean velocity and pressure decomposed into ensemble average and fluctuating component. Equation 2.4 is the incompressible Navier-Stokes equations incorporated with Reynolds equations. In the above equations second order moment term $<u_i u_j>$ is known as "Reynolds stress"

2.1.1 Phenomenological model- Kolmogorov's theory

Richardson introduced the idea of energy cascade for turbulent flows (Richardson, 1922). In energy cascade process kinetic energy is transferred from larger to smaller scales until energy is totally dissipated by viscosity. Turbulent flow comprised of different size eddies. Larger eddies are unstable and continuously undergo breaking process to become smaller eddies, these smaller eddies break up into even smaller eddies. As eddies break up to smaller eddies, energy is transferred. This process continues till Reynolds number becomes sufficiently small so that the eddy motion is stable and viscosity dominates the dissipation of kinetic energy. Scale of dissipation rate, ε can be calculated as $\frac{u_0^2}{\tau_0} = \frac{u_0^3}{l_0}$, where u_0 is the maximum velocity fluctuations, l_0 is the length scale for the largest eddy and τ_0 is the time scale for largest eddy. Experimental observation in free shear flows indicates similar time scale for ε (Pope, 2000) . Since introduction of energy cascade, several questions remain unanswered, like what is the smallest eddy size? Does characteristic length *l* have any impact on velocity and time scale? Kolmogorov postulates three hypotheses to answer some of the questions mentioned above (A. Kolmogorov, 1941). This is widely known as K41.

In the first hypothesis Kolmogorov argued that during energy transfer process from larger scale to smaller scale directional basis is lost, only energy is transferred to smaller eddies. Therefore small-scale motions become isotropic even though large-scale motions are anisotropic. The concept of isotropic turbulence was first introduced by Taylor(Taylor, 1935). He assumed turbulent flows as isotropic and homogeneous to simplify the complexity of turbulent problem. But in reality turbulent flows are always anisotropic and inhomogeneous. Kolmogorov also argued that other

information like mean velocity field, boundary condition are also lost during the cascading process; as a result statistics of small-scale motion is universal.

In the first similarity hypothesis Kolmogorov postulates motions of small-scale is universal at higher Reynolds number and truly becomes a function of viscosity, ν and dissipation rate, ε. Therefore, characteristics such as length scale and velocity length scale become function of ν and ε. Following scales can be derived based on the hypothesis.

$$\eta \equiv (\nu^3/\varepsilon)^{1/4} \tag{2.5}$$

$$u_\eta \equiv (\varepsilon\nu)^{1/4} \tag{2.6}$$

$$\tau_\eta \equiv (\nu/\varepsilon)^{1/4} \tag{2.7}$$

Where η is the Kolmogorov length scale (characteristic length scale), u_η is the velocity scale and τ_η is the time scale. Reynolds number calculated based on Kolmogorov length scale is unity $Re_\eta = \eta u_\eta/\nu = 1$.

A new range named "inertial sub-range" was introduced to postulate second similarity hypothesis. According to the hypothesis, at higher Reynolds number there exists a sub range $(\eta \ll r \ll L)$ where small-scale motions are universal and function of ε only, independent of ν. In the sub-range r, both viscous effects and anisotropic effects are negligible due to large-scale. Based on the second similarity hypothesis two ranges were proposed that lie in between dissipation range and integral length scale (Pope, 2000). Universal equilibrium range, l_{DI} lies between dissipation range and inertial sub-range while energy containing range lies between integral sub-range and integral length scale. Relations between the two can be established as:

$$\eta < l_{DI} < r \tag{2.7}$$

$$r < l_{EI} < L \tag{2.8}$$

Since the inception of K41 several experimental investigations have been carried out to validate the concept of universal structure of small-scale motion in turbulent flows. For the first few moments, there exists a universal scaling law. As the magnitude of order increases strong deportation was observed, which indicated wrong assumptions in K41 theory. Obukhov realized that intermittency changes in large-scales, causing the fluctuations in dissipation rate are the reason for K41 failure (Obukhov, 1962). Later in 1962 Kolmogorov refined his similarity hypothesis, which is known as "refined similarity hypothesis" or K62 (A. N. Kolmogorov, 1962). In refined similarity hypothesis he stated that at higher Reynolds number small-scale motions are universal and isotropic, truly is a function of ε_r and v. Where ε_r is local average dissipation rate. One key change with K41 is he replaced ε with ε_r, also added ε_r fluctuation is log-normal distribution.

There is no connection between K41 and Navier-stokes equations for incompressible flow. In classic era turbulence, research was totally focused on validating similarity hypothesis.

2.2 Turbulence research in "modern era"

Modern era of turbulent research began in early sixties. In this section we will cover research conducted after the K62 or RSH (refined similarity hypothesis) was proposed. Beginning of the modern era it was obvious that fluctuating large-scale motions are responsible for temporal dissipation rate fluctuation, while highly intermittent small-scales motions are responsible for spatial dissipation fluctuations. Backed by several observations small-scale statistics proposed by Kolmogorov in his K62 agrees well for longitudinal structure functions. Later it was observed by

simulations that when the order is greater than 10, longitudinal structure functions show significant deviations (Katepalli R Sreenivasan, 1998) and when the order is greater than 5, transverse structure function shows devastations in scaling exponents. However, K62 did not provide any explanation on directional dependency of scaling exponents.

In refined similarity hypothesis Kolmogorov replaced energy dissipation rate by local average dissipation rate, ε_r. He also assumed that this ε_r fluctuation in time follows log normal distribution. Lot of effort has been made to find the log normal distribution of local average dissipation, but till date disagreement prevails on log-normal conjecture. Gurvich et al. derived a mathematical model of energy cascade process of turbulent eddies break downs validated by experimental evidence (Gurvich & Yaglom, 1967). They observed that log normal distribution of local average dissipation rate can be achieved at higher Reynolds number along with scale similarity hypothesis. Others claimed log-normal conjecture as invalid (Mandelbrot, 1974; Novikov, 1971).

2.2.1 Recent advancement in turbulence research

Chen, Sreenivasan et al. observed that if they use local average enstrophy (square vorticity) instead of local dissipation rate, ε_r scaling of transverse structure function shows better correlation (Chen, Sreenivasan, Nelkin, & Cao, 1997). They confirmed this by performing numerical simulations of Navier-Stokes equations at moderate Reynolds number. Hence they proposed refined similarity hypothesis for the transverse direction (RHST) and this RHST is valid for transverse structure function only in inertial range. This closes the gap of original RSH that only tells about exponents of longitudinal structure function. Several researches were performed on small-scale intermittency mainly focusing on dissipation intermittency and inertial range intermittency (K. R. Sreenivasan & Antonia, 1997). This will be discussed later sections in this chapter.

Large-scale coherent structure is another fascinating area in turbulence research and brought new excitement to the fluid mechanics community. Coherent structures are well organized random motions naturally happening in fluid turbulence (Katepalli R Sreenivasan, 1999). Hussain provided a well-developed definition of coherent structure, according to him "a coherent structure is connected, large-scale turbulent fluid mass with a phase-correlated vorticity over its spatial extent. That is, underlying the three dimensional random vorticity fluctuations characterizing turbulence, there is an organized component of the vorticity which is phase correlated (i.e. coherent) over the extent of the structure " (Hussain, 1983). In fluid flow coherent structure plays vital role transporting mass, heat and momentum. Kline et al. first recognized the coherent structure in fully developed turbulent shear flows using flow visualization technique. (Kline, Reynolds, Schraub, & Runstadler, 1967) Liepmann (Liepmann, 1952) and Favre et al. (Favre, Gaviglio, & Dumas, 1967) experimentally measured the correlation functions that confirm the evidence of existence of coherent structures. Several theories (Holmes, Lumley, Berkooz, Mattingly, & Wittenberg, 1997; Kovasznay, Kibens, & Blackwelder, 1970) have been proposed regarding the coherent structure, basically indicating how they maintain coherence. Despite all findings and theories the community is still waiting for clear solutions to be proposed (Katepalli R Sreenivasan, 1999).

2.3 Probability Density Functions (PDFs)

Castaing et al. experimentally studied probability density functions (PDFs) of velocity differences between two successive points (Castaing, Gagne, & Hopfinger, 1990). Velocity differences were calculated using, $u_r = u(x + r) - u(x)$ where r is very short distances namely close to Kolmogorov dissipative scale. They performed their study at higher Reynolds number for two different experiments; jet flow ($Re_\lambda = 852$) and wind tunnel ($Re_\lambda = 2720$). They observed that

PDFs are non-Gaussian with exponential tails. From their experiments they developed two parameters PDF model closely following Kolmogorov's log normality ideas. They claimed when r is small, tails of experimental PDFs deviate from exponential behavior that clearly agrees with their proposed model. Kailasnath et al. measured PDFs of velocity increments in atmospheric boundary surfaces for a wide range of separation distances (Kailasnath, Sreenivasan, & Stolovitzky, 1992). They used hot-wire technique to measure the velocity fluctuations. Later they used Taylor's frozen hypothesis to convert the time intervals into space intervals. Stretching exponents were 0.5 when a separation distance was in dissipation range and 2, while the dissipation range in integral scale. Measured PDFs of velocity increments showed well agreements with theoretical multi-fractal notions. PDFs of longitudinal velocity increments in low temperature helium gas were experimentally measured for a wide range of Reynolds number (Re_λ = 150 to 5040) (Tabeling, Zocchi, Belin, Maurer, & Willaime, 1996). PDFs are independent of Reynolds number at higher Re_λ at inertial range of scale. Skewness and flatness of the velocity derivatives increase with the Reynolds number up to Re_λ= 700 and after that seems to remain same.

2.3.1 PDFs of fluctuations velocity

Probability density functions (PDFs) of single point velocity fluctuations are fundamental to understanding turbulent. Previously much attention has given to study PDFs of velocity differences. However, focus has shifted toward velocity fluctuations. It was believed that velocity fluctuations are Gaussian (Batchelor, 1953; Kendall & Stuart, 1977). The conclusion was drawn depending upon the turbulent data available at that time. Batchelor incorporated center limit theory with Fourier transformation of velocity fluctuations to explain Gaussian behavior of PDFs (Batchelor, 1953). Recently new measurement technique has revealed that velocity fluctuations

are not Gaussian. This was confirmed by several experiments. Flatness factor, $F_u = \langle u^4 \rangle / \langle u^2 \rangle^2$ can be calculated to test the Gaussianity of velocity fluctuations. When $F_u < 3$ velocity fluctuations becomes sub-Gaussian, $F_u > 3$ velocity fluctuations are hyper-Gaussian (Hideaki Mouri, Takaoka, Hori, & Kawashima, 2003).

Mouri et al. studied PDF of turbulent velocity function in grid turbulence. They observed that near to the gird the shape of the PDF was sub-Gaussian as opposed to the Gaussian shape in the fully developed region of the turbulence. The shape of the PDF later was found to be hyper-Gaussian in the decaying turbulence far downstream of the grid (H. Mouri, Takaoka, Hori, & Kawashima, 2002). In a separate study they measured PDFs of single point velocity fluctuations in a rough wall boundary layer using Fourier coefficients focusing in the energy containing range (Hideaki Mouri et al., 2003). Velocity fluctuations are Gaussian where the energy containing motions are random and independent i.e. ideal turbulence. Velocity fluctuations become sub-Gaussian where various sizes of eddies are generated and hover around randomly and independently. In the rough wall boundary layer where the wavy wakes is contaminated with the roughness of the wall, velocity fluctuations are hyper-Gaussian.

Ishirara et al. studied one point statistics of velocity gradients using DNS and observed the Reynolds number dependence of their PDFs. They considered the skewness and flatness factor to quantify the anisotropy in the fluctuating velocity gradient (Ishihara, Kaneda, Yokokawa, Itakura, & Uno, 2007).

2.3.2 PDFs of dissipative scale

The concept of calculating probability density functions in turbulent flow is half century old. Attempts were made to calculate PDFs of velocity increments, velocity fluctuations and log normal

PDFs of dissipation fluctuations. Several literatures can be found on this topic including experimental data to calculate PDFs of dissipation fluctuations. (Kurien & Sreenivasan, 2001; Yakhot, 2001). Yakhot derived dissipation scale η using Mellin's transformation combined with Gaussian large-scale boundary condition. He also calculated PDFs of dissipative scale $Q(\eta)$ (Yakhot, 2006). Later several attempts have been made to find the universality in local dissipation scale in wide range of flows, i.e. homogeneous isotropic turbulence, buoyancy-driven turbulence, turbulent pipe flows, channel flows, channel with backward facing step. Biferale (L Biferale, 2008) used multifractal technique to predict the fluctuation of local dissipation scale, η using multifractal relation provided by Paladin and Vulpiani (Paladin & Vulpiani, 1987). Predictions were compared for both intense velocity fluctuations and smooth velocity fluctuations; both trends are in agreements with DNS (Schumacher, 2007) study. It was suggested that refinements may be necessary if someone wants to distinguish between longitudinal and transverse dissipation scales. Previously it was found that longitudinal and transverse structure functions possess different scaling properties in isotropic turbulence (Gotoh, Fukayama, & Nakano, 2002).

Schumacher performed direct numerical simulations (DNS) of homogeneous isotropic turbulence (HIT) to investigate sub-Kolmogorov scale fluctuations. (Schumacher, 2007) Three dimensional Navier-Stokes equations for an incompressible flow were solved using pseudospectral method incorporating fast Fourier transformation. Spectral resolutions were one order of magnitude higher than standard simulations in order to capture fine-scale structures. Small-scale intermittency increases with Reynolds number causing increase of local dissipation range. Theoretical $Q(\eta/\eta_0)$ derived by Yakhot (Yakhot, 2006) was compared with numerical results for three different Reynolds number ($Re_\lambda = 107$, $Re_\lambda = 65$ and $Re_\lambda = 10$). Numerical results of PDFs (left tail) show Reynolds number dependence. In a separate DNS study HIT was performed at relatively

lower Reynolds number (Re_λ=10, 24, 42 and 64) (Schumacher, 2007). Instead of η_0 , η_k was used to normalize η. PDFs, $Q(\eta/\eta_k)$ agrees qualitatively with theoretical results. It was observed while $\eta > \eta_k$ tails agree better with theoretical results, $\eta < \eta_k$ tails starts to depart from theoretical predictions.

Bailey et al. conducted turbulent pipe flow experiment using Princeton University/ONR superpipe facility (Zagarola & Smits, 1998) for a wide number of Reynolds number ($Re_\lambda = 35$ to $Re_\lambda = 135$)(Bailey et al., 2009). Hot wire anemometer technique was used to measure streamwise velocity. They calculated local dissipation scales at center of the pipe, where the turbulence can be considered isotropic and at logarithmic layer of pipe wall, where turbulence becomes anisotropic. PDFs of η/η_0 , $Q(\eta/\eta_0)$ was calculated both at near the wall and center of the pipe, agree well with DNS study performed by Schumacher (Schumacher, 2007). Although deviation was observed for both tails with theoretical PDFs derived by Yakhot (Yakhot, 2006). This may be due to the saddle-point approximation used in Mellin transformation. Similar deviation was observed for DNS study by Schumacher (Schumacher, 2007). From the pipe flow experiment and pervious DNS results it was concluded that PDFs are independent of both Reynolds number and degree of anisotropy, although Re_λ for super pipe experiment was at moderate range.

Focusing on the same methodology and ideas (Bailey et al., 2009; Schumacher, 2007; Yakhot, 2006) Zhou and Xia conducted experimental investigation of local dissipation scale, η for buoyancy driven turbulence to confirm the concept of universality of PDFs of local dissipation scales(Q. Zhou & Xia, 2010). Particle image velocimetry (PIV) experiments were performed for convection cell (Sun, Ren, Song, & Xia, 2005) using water as working fluids. Spatial resolutions were reported 0.59 mm with hollow glass spheres seeding particles with mean diameter 10 μm. From the experiments it was observed that PDFs of η is independent of turbulent intensity, large-

scale inhomogeneity and anisotropy of the flow. $Q(\eta/\eta_0)$ was measured at three different locations; at center cell (flow is homogeneous and isotropic), near the sidewall (plume dominated region, in presence of coherent structures) and near bottom plate. One interesting phenomenon was observed in PDFs, on plume dominated region $Q(\eta/\eta_0)$ exhibit less steep tail comparing with $Q(\eta/\eta_0)$ measured at cell center. It was argued that near wall coherent structure may be the reason for such deviations. Measured $Q(\eta/\eta_0)$ was compared with $Q(\eta/\eta_0)$ of HIT box turbulence (Schumacher, 2007) and turbulent pipe flows (Bailey et al., 2009). Buoyancy-driven turbulence $Q(\eta/\eta_0)$ shows good agreement with right tails but deviated towards left for left tails. It explains that higher probabilities are due to increased small-scale intermittency caused by thermal turbulence.

Hamlington et al performed high-resolution DNS study in channel flow for higher Reynolds number. Friction Reynolds numbers, Re_τ was reported 180, 381 and 590. (P. E. Hamlington et al., 2012). Fourier-Chebyshev pseudospectral method was used to solve three dimensional incompressible Navier-Stokes equations. Resolutions of the study were improved approximately factor of five in spatial direction comparing with other recent DNS studies.(Hoyas & Jiménez, 2006; Kim, Moin, & Moser, 1987; Moser, Kim, & Mansour, 1999) $Q(\eta/\eta_0)$ was calculated at various y^+ locations and compared with previous studies. At center of the channel where y^+=90 PDFs shows good agreements in HIT case and pipe flow experiment. Interestingly it was observed for higher Reynolds number, Re_τ = 590 the peak locations of $Q(\eta/\eta_0)$ shifted towards rightward as y^+ locations move from center to wall of the channel. Near the wall, flow is highly anisotropic and flow is dominated by shear. They argued that this is due to the extended coherent vortices present near the wall, explained earlier by Adrian (Adrian, 2007). Despite the peak deviations near wall they optimistically concluded there may be universal behavior in dissipation scales.

2.4 Structure functions (SFs)

Turbulent flows in nature are inherently anisotropic due to the presence of mean shear as the primary mechanism of turbulent production. While there is a considerable body of literature focused on understanding the small-scale phenomenology of isotropic turbulence, the relative number of studies focused on characterizing the small-scale structure of turbulence in anisotropic flow is lower. Most of these studies addressing the small-scale structure of anisotropic flows have focused on testing the applicability of scaling predictions derived from either the refined similarity hypothesis, or the multi-fractal phenomenology of turbulence, both of which predict a universal small-scale structure. Nevertheless, it is well documented in literature that these classical predictions often appear to break down in most practical turbulent flows, particularly in those which possess strong anisotropy.

2.4.1 SO(2) and SO(3) decomposition

With respect to strongly anisotropic turbulence, one approach that has come forth, probes and dissects the small-scale structure in these flows by utilizing the concept of applying the special orthogonal decomposition of SF tensors in 2 or 3 dimensions, denoted as SO(2) and SO(3) respectively (L. Biferale, Calzavarini, Lanotte, Toschi, & Tripiccione, 2004). SFs refer to the statistical moments of fluctuating velocity differences across spatial separations and have been an integral statistical object to depict the spatial organization of turbulent eddies across varying lengths scales. Biferale et al. applied the SO(3) decomposition of SFs to turbulent channel flows to elucidate anisotropic and isotropic fluctuations at all scales (L. Biferale, Lohse, Mazzitelli, & Toschi, 2002) and uncovered that the coherent vortical structures cause strong effects of

anisotropic fluctuations near the channel wall. In a separate study Biferale et al. found that at the large-scale, forced system anisotropic fluctuations are anomalous in contrast to the intermediate and small-scales where these anisotropic fluctuations were found to be universal, and that such small-scale dynamics are originated from inertial evolution (L. Biferale et al., 2004).

2.4.2 Second order structure functions

Weitao et al studied the turbulent cylinder wake (as the source of anisotropy) to understand the scaling of longitudinal and transverse SFs. They found that the transverse velocity increments were more intermittent than the longitudinal velocity increments and that the transverse scaling exponents were smaller (i.e. more saturated) than longitudinal scaling exponents (Bi & Wei, 2003). Apart from the above studies using the SO(2) and SO(3) decomposition techniques, classical studies include the study of probability density functions and whole SFs in anisotropic flows. Arad et al. studied the anisotropic contributions in the turbulent atmospheric boundary layer. Second order SFs in both longitudinal and transverse directions were calculated and it was found that the anisotropic effect in the transverse direction was far more pronounced than in the longitudinal direction (Arad et al., 1998). Zhou and Antonia conducted another study investigating the small-scale structure in grid generated turbulence. By calculating the second and third order moments of spatial velocity differences, their study showed that the anisotropy at the small-scales decreased with increase in the Taylor Reynolds number, Re_λ (T. Zhou & Antonia, 2000). Tsuji conducted experiments to study the flow over a rough wall and examine the effect of large-scale anisotropy on small-scale statistics in a turbulent boundary layer (Tsuji, 2003). They investigated the effects of strong mean shear on the range of dissipation rate fluctuations and its spectrum in addition to analyzing the behavior of SFs. It was also observed that second order SFs do not exactly follow a

power law profile, and rather show a convex profile in the non-dissipative range implicating the significant presence of large-scale anisotropy in the transverse direction. Garg and Warhaft studied small-scale structure in homogeneous shear flow for Re_λ between 156 to 390(Garg & Warhaft, 1998). Based on the calculated skewness and kurtosis of the velocity derivative and probability density functions (PDFs) of velocity increments, the researchers reported strong anisotropic effects both in the inertial as well as dissipative scales.

Huang et al. studied second order SF in fully developed turbulent flow and found that the large-scale has a great influence in SFs (Y. X. Huang et al., 2010). They estimated the large-scale contribution at about 79%. Kaneda and Ishihara studied the turbulence using DNS neglecting the effect of small-scale turbulence statistics and realized that turbulence is not remote from the boundary hence there is some effect on small-scales that needed to be revealed(Kaneda & Ishihara, 2009).

2.5 Turbulence research on backward facing step

Separations and reattachments are very important in turbulent flows. These phenomenon are present in engineering applications like combustion chambers, diffusers, flow around airfoils and buildings. To understand above mentioned complicated flows one needs to understand and predict the nature of reattaching shear layers. Both separations and reattachments can be observed in simple channel flow with a backward facing step. Backward facing step became popular as laboratory experiments for its geometrical simplicity. Till date notable amount of experiments and numerical study have been performed on backward facing step(Alam, Walters, & Thompson, 2011; B. Armaly, Li, & Nie, 2003; B. F. Armaly, Durst, & Pereira, 1983; Sbra Jovic & Driver,

1994; S Jovic & Driver, 1995; Kim et al., 1987; Walters, Bhushan, Alam, & Thompson, 2013). In backward facing step flow experiences adverse pressure gradients causing boundary layer separating from wall. At the sharp step corner upstream boundary layer separates and forms shear layers. Figure 2.1 shows schematic of backward facing step with intense shear zone immediately after the step. Separated shear layer in backward facing step can be compared with ordinary plane mixing layer (J. Eaton & Johnston, 1981). In other literature it was argued that reattaching shear layer is different from plane mixing layer (Chandrasuda, 1975; Chandrsuda, Mehta, Weir, & Bradshaw, 1978). As moving away from the step the width of the share layer increases and intensity of shear decreases, it takes sometimes 50h distance from the step to fully recover from shear layer (Bradshaw & Wong, 1972; Smyth, 1979). Beneath the shear layer a big recirculation zone is formed. Often times a backflow of over 20% of free stream velocity is observed in this region (Chandrasuda, 1975; J. K. Eaton & Johnston, 1980).

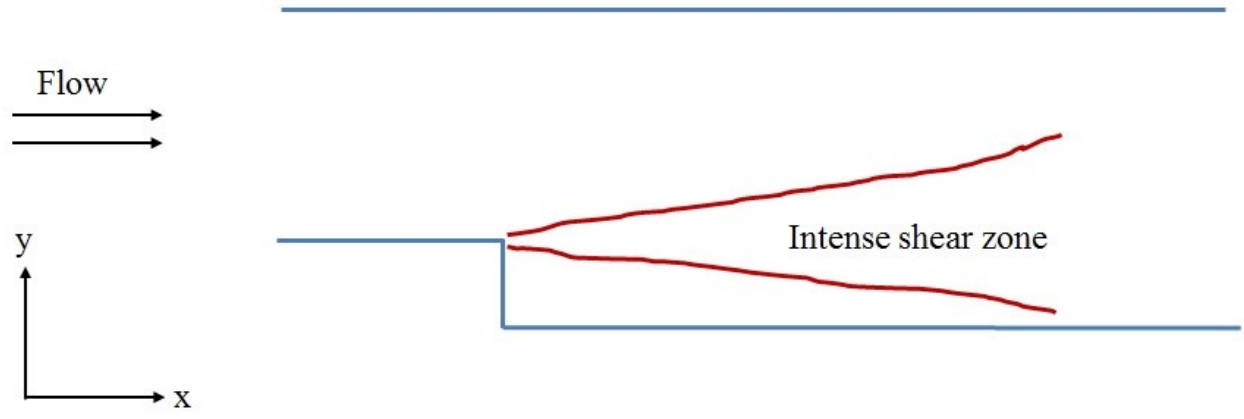

Figure 2.1: Schematic of backward facing step

Armaly et al. conducted both experimental and theoretical investigation on channel flow with backward facing step (B. F. Armaly et al., 1983), served a wide range of Reynolds number (Re_D from 70 to 8000) representing laminar, transitional and turbulent flows. Air was used as working fluids in two-dimensional backward facing step with 1:1.94 expansion ratios. Laser Doppler measurement technique with forward scattered light was used. Silicone-oil particle with mean diameter of 2 μm was used as seeding particles. Recirculation length immediately after the backward step depends on Reynolds number. Separation length increase with Reynolds number when the flow is laminar, during transition from laminar to turbulent initial strong decrease in separation length was noticed. It was observed when $Re > 1200$ flow remains laminar, when $1200 < Re < 6600$ flow is transitional and when $Re > 6600$ flow becomes fully turbulent. In the experiments at least three re-circulation regions was observed after the step. Numerical prediction showed good agreement with experiments up to Reynolds number 400. When $Re \geq 400$ numerical results start deviating from experiments.

2.6 Large-scale anisotropy

Le, Moin et al. performed direct numerical simulations on backward facing step at Re_h=5100 (Reynolds number based on step height). (Le, Moin, & Kim, 1997) Expansion ratio for the channel was 1.20. DNS results validated their results with Jovic & Driver's experiments (Sbra Jovic & Driver, 1994) performed almost at similar flow conditions with Re_h=5000. Le et al. was the first to report three dimensional DNS on backward-facing step. From simulation reattachment length was found to be 6.28h. which agrees within 3% of Jovic and Deiver's experimental measurements. Higher negative skin friction was observed in the recirculation region at lower Reynolds number. This was also confirmed by a different experiment by Jovic and Driver. (S Jovic & Driver, 1995).

In recovery region, they observed that mean velocity profile shifted downwards from universal log-law profile, which contradict previous findings. They argued that this is the combined effect of lower Reynolds number and adverse pressure gradient. Turbulent kinetic energy production and dissipations is peak in the shear layer after the step. Velocity pressure gradient and viscous diffusion was found to be negligible in the shear layer, but dominating close to the wall. At the exit of the computational domain x=20h, the flow was not fully recovered.

Earlier day's measurement in backward facing step was challenging specially in recirculation and reattachment region since hot wire anemometer was not suitable for reverse flow measurement. With development of image based measuring techniques (PIV, PTV, LDV) researchers got the momentum to perform more experiments at higher Reynolds numbers Piirto estimated turbulence energy in a backward facing step using three component (three dimensional) PIV experiments (M. Piirto, Saarenrinne, Eloranta, & Karvinen, 2003). Expansion ratio for their experiment was 1.5 and water was used as working fluid with 5 microns mean diameter polyamide seeding particles. Reynolds number for their experiments was reported 15000 (Re_h). They reported that peak values of rms and Reynolds stress are 20% less compared to DNS study (Le et al., 1997). This reduction is the effect of low pass filtering inherited in PIV algorithm. Higher expansion ratio causes turbulent energy budget peak shift towards the wall. Several literatures are available (B. Armaly et al., 2003; Kasagi & Matsunaga, 1995; Kostas, Soria, & Chong, 2002; Mika Piirto, Karvinen, Ahlstedt, Saarenrinne, & Karvinen, 2007; Pilloni, Schram, & Riethmuller, 2000; Tinney & Ukeiley, 2009) on backward facing step that experimentally studied large-scale at different configurations i.e. expansion ratio, aspect ratio, with double steps.

2.7 Summary

In summary, a brief description of turbulent research from classical era to modern era was provided in this chapter. Details and in-depth literature review on instantaneous dissipation scales, probability density functions of velocity fluctuations, second order structure functions, SO(2) & SO(3) decompositions were discussed. Separation and reattachment flow phenomenon observed in a channel flow with a backward facing step were also discussed. Due to its simple and easy experimental setup and capability to produce inhomogeneous and anisotropic turbulence in vicinity of the backward facing step, it became popular for turbulent research.

Chapter 3

EXPERIMENTAL METHODS

3.1 Introduction

To study the small-scale structure of turbulent flows in presence of strong mean shear, experiments were performed in channel flow with backward facing step. Backward facing step is a widely used, classical method to study the fluid flow (B. F. Armaly et al., 1983; Bradshaw & Wong, 1972; Sbra Jovic & Driver, 1994; Le et al., 1997). In backward facing step strong shear is generated immediately after the step. To capture the velocity fluctuations in channel particle image velocimetry (PIV) technique was used. 2D time-resolved experiment was performed at higher Reynolds number to capture the smallest scale behavior in turbulent flows. This chapter provides an overview of experimental setup, details of particle image velocimetry systems, advantages of PIV technique, data processing and error calculation.

3.2 Experimental Setup

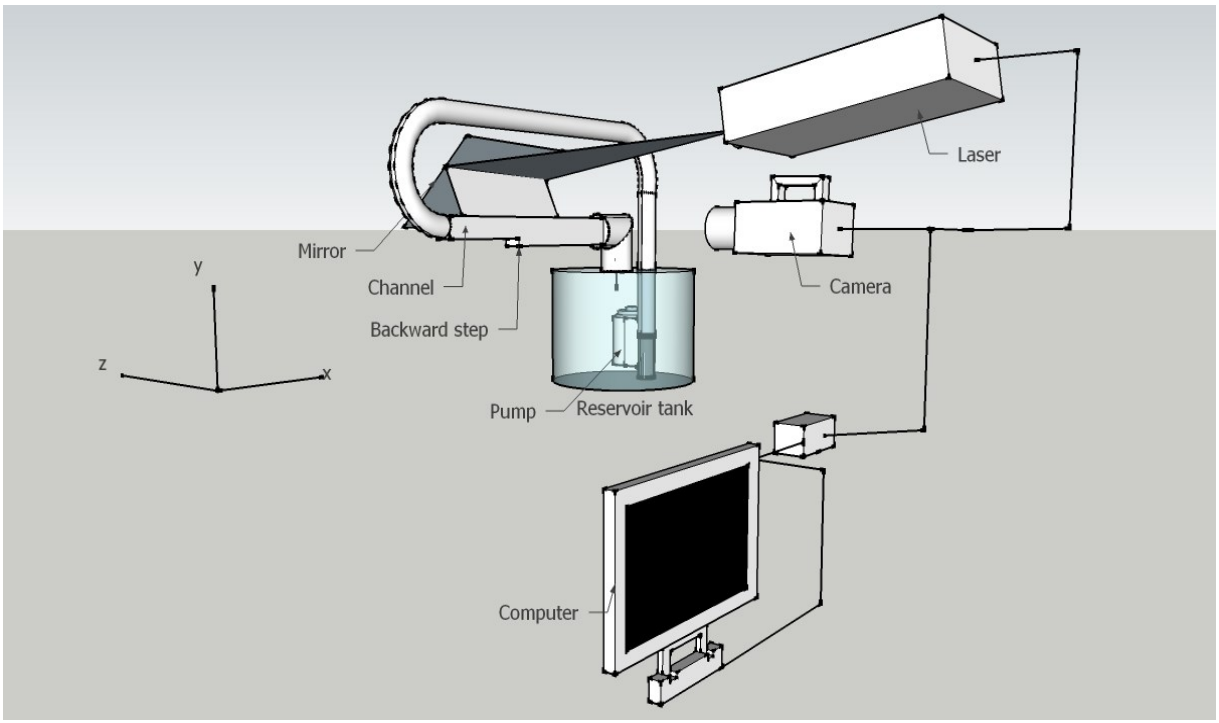

Figure 3.1: Perspective schematic of the experimental setup

3.2.1 Backward facing step

Two dimensional time-resolved particle image velocimetry (PIV) experiments were conducted to capture the turbulent velocity field along the centerline of a rectangular channel flow with a backward facing step. The step size, h, was 5 mm with the total channel length being 172h. The inlet and outlet cross sections of the rectangular channel were 6h×13h and 7h×13h respectively. The fetch length upstream of the backward step was 120h. A honey-comb section at the inlet conditioned the flow to break away large-scale cross stream eddies. The honey comb section was a plastic section of approximate length 5h and cell size of approximately 1h. The expansion ratio

(ER) defined as (H+h)/H, was 1.172 with an aspect ratio (AR) defined as b/H, equal to 2.24, where b is the channel width and H is the channel height. The acrylic channel was transparent thereby allowing high resolution PIV measurements.

3.2.2 Flow facility

Figure 3.1 shows a schematic of the flow facility that enabled PIV measurements in the above described rectangular channel with a backward facing step. Water at room temperature was circulated through the acrylic channel driven by a submersible pump in a closed loop manner. A bend-meter connected to a manometer recorded pressure difference that was pre-calibrated to obtain the bulk flow rate in the channel. Experiments were performed corresponding to two Reynolds numbers, $Re_{h,}$ based on the step height h, and maximum free-stream velocity U_o namely: 13600 and 5500. The corresponding Reynolds numbers based on channel inlet height H, or hydraulic diameter of the inlet, $D = 2bH/(b+H)$ are provided in Table 3.1. Table 3.1 also reports Reynolds numbers based on the upstream shear velocity, denoted Re_τ. The table also includes comparison to Reynolds numbers of the most relevant backward facing step data from literature.

Table 3.1: Reynolds number comparison

	Reynolds number based on inlet height, Re_H	Reynolds number based on step height, Re_h	Reynolds number based on inlet hydraulic diameter, Re_D	Reynolds number based on upstream shear velocity, Re_τ
Case I	78880	13600	108800	2055
Case II	31900	5500	44000	870
Jovic & Driver (1994)	-	5000	-	-
Le et al (1997)	-	5100	-	-

3.3 Particle Image Velocimetry (PIV)

Particle image velocimetry (PIV) is a non-intrusive and indirect velocity measurement technique which allows measuring the fluid motions by illuminating a two dimensional thin light sheet. Camera captures the motions of "seeding particles" and estimates the kinematics of local fluid. "Seeding particles" are required to be neutrally buoyant and to efficiently scatter light. This optical technique provides accurate measurement of instantaneous velocity field. In the last 20 years PIV technique has developed and gained popularity among the fluid mechanics community(Adrian, 2005). Certainly PIV techniques provided more degree of freedom than other velocity measuring techniques (i.e. hot wire anemometer, classical Pitot tube, laser doppler velocimetry (Albrecht, 2003; Goldstein, 1996)). Pressure probes or hot wires are inserted in flow field to measure the flow data for hot wire anemometer method, the flow experience disturbed by presence of external elements. In PIV technique flow can be measuree without disturbing the flow, and most importantly, instead of a single point (for hot wire anemometer) velocity data is available for the whole region. On the other hand pointwise measurement techniques are fully developed and

capable of capturing tiny or rapid changes of flow. Using an array of single point probes one can get a good idea about the entire flow field. Citriniti and George used 138 synchronized hot wire anemometers to study the large-scale and coherent structure of a round jet nozzle (Citriniti, 2000). Using an array of single point probes is always cumbersome. It not only increases the complexity of the experiment but also other issues like locations of the probes, cost and calibration issues need to be taken care of.

Local velocity data is very important for turbulent research; additionally having the data of global velocity field is also very exciting to turbulent researchers and applied research & development community. PIV helps to understand the complex flow behavior by visualization and helps designers to quickly adjust their fluid machinery to gain desired output. PIV experiments can be very quick compared to conventional flow measurements methods that can save resources due to running expensive flow facility. Image post processing and image analysis can be done separately at convenience. With PIV systems images can be captured at very higher temporal and spatial resolutions. Recent developments in high speed lasers, camera and powerful lenses are making PIV system more and more appropriate for any flow visualization.

Seeding particles or tracer particles in PIV system should be tiny enough so that it has no effect on flow dynamics and it should have better light scattering efficiency so that video sensors can easily capture the motion of the particle. A thin laser sheet, generated by passing double pulsed laser beam with optical arrangement, caused tiny seeding particles to be illuminated twice with a very small time gap in between. A high speed CCD camera is placed perpendicular to the laser sheet. The time of particle displacement is recorded as either a single image exposed twice or a pair of two single exposed images. Time difference between two pulses is chosen depending upon the flow velocity and magnification of the camera. Later on velocity vector is calculated from

known pulse difference and seeding particles displacements. In order to calculate velocity vector PIV images are divided into small subsections – commonly known as "interrogation windows". Auto-correlation, a statistical correlation technique is used to calculate local velocity vectors at each interrogation window. The size of the interrogation window needs to be chosen dexterously so that all the particles move homogenously in the same direction and same distance and also there should be sufficient number of particles in each interrogation window.

3.3.1 Laser and Camera

Time resolved PIV experiments measured the instantaneous turbulent 2D velocity field in the streamwise (x) × wall normal (y) directions along the channel centerline immediately downstream of the step. The PIV system used was built by LaVision Inc., equipped with a diode-pump Q-switched Nd:YLF laser (Photonics Industries, Bohemia, NY) coupled with external spherical and cylindrical lenses to illuminate the measurement region with a thin laser sheet. The $1/e^2$ thickness of the laser sheet was estimated at < 0.1 mm. A mirror was used to position the laser sheet aligned with the channel centerline as shown in Figure 3.1. Raw PIV images were captured using a synchronized high speed camera (Photron, San Diego, CA,Model: FASTCAM SA3) with a 50 mm Nikon lens. Figure 3.2 shows Photron FASTCAM SA3 camera used in the experiments. Figure 3.4 shows raw image capture by high speed camera. The camera was equipped with a 12-bit CMOS sensor of 1024 x 1024 pixel resolution with each pixel physically measuring 17 x 17 μm^2. For each of the two Reynolds number cases (Table 4.1), double frame images were captured at a sampling rate of 2 kHz. The total number of samples obtained was 4,215 per case.

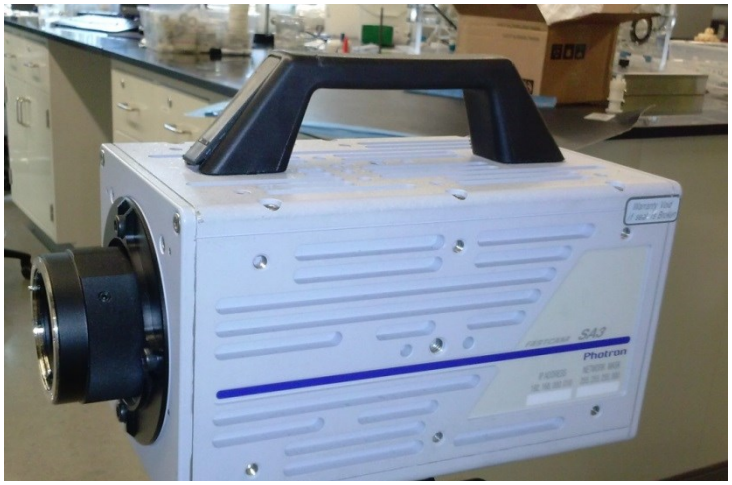

Figure 3.2: Photron high speed camera (Model: FASTCAM SA3) used in experiment

3.3.2 Seeding Particles

The fluid was seeding with polyamide seeding particles (Dantec Dynamic Inc.) with a mean particle size of 20 μm. The distribution of particles was such that 5% of the particles had a diameter less than 10 μm, and another 5% with diameter greater than 30μm. The laser pulse separation was in the range of 50 to 300 μs in order to obtain a gross particle displacement in the range of 5 to 10 pixels. The resulting spatial resolution after in-situ calibration of the images was 27.8 μm/pixel.

3.3.3 Resolutions

In order to assess the influence of large-scale anisotropy on the small-scale structures, we demonstrate that the above described measurements of the instantaneous turbulent velocity field do resolve at least a sizeable portion of the dissipative regime. Note that this study does not aim to resolve the Kolmogorov scale or sub-Kolmogorov features within the measured instantaneous

turbulent fields. Given that the objective of this study is to investigate how the effects of strong anisotropy (mean shear) influence the dissipative regime of second order structure functions, it is required that current measurements at least resolve well below the Taylor micro-scale, which is regarded as the conventional cut-off length scale separating the dissipative regime and the scales where inertia is more dominant (non-dissipative scales). As demonstrated below, it was shown that current experiments not only resolve the Taylor micro-scale but also capture a sizeable portion of the dissipative regime. This is done through the analysis of the probability density function of the instantaneous dissipative scale fluctuations derived from our dataset at each of the points of interest chosen in this study.

Table 3.2 lists the Taylor micro-scale in microns calculated from the longitudinal 2-point correlation function at each point of interest for all Reynolds number cases. As can be seen, the magnitude of the Taylor micro-scales is far greater than the velocity resolution (one vector every four pixels).

Table 3.2: Taylor micro-scale (λ), integral length scale (L), Taylor Reynolds number (Re_λ), Reynolds number based on integral length scale (Re_L) at seven different location for all three cases

Position	Case I					Case II				
	λ (μm)	L (mm)	τ_0 (mS)	Re_λ	Re_L	λ (μm)	L (mm)	τ_0 (mS)	Re_λ	Re_L
1	628.8	5.9	2.18	142	1339	1117.1	6.6	6.03	89	529
2	715	5	1.84	105	733	1068.1	5	4.55	70	329
3	490.7	4.3	1.57	131	1142	623.3	2.7	2.44	64	277
4	545.2	4.4	1.63	122	996	1072.6	6.8	6.21	96	608
5	639.2	6.9	2.55	162	1759	915.4	5.8	5.31	96	611
6	409.6	4.5	1.67	166	1839	713.2	5.4	4.87	113	848
7	501.4	5	1.84	150	1491	864	5.4	4.94	94	594

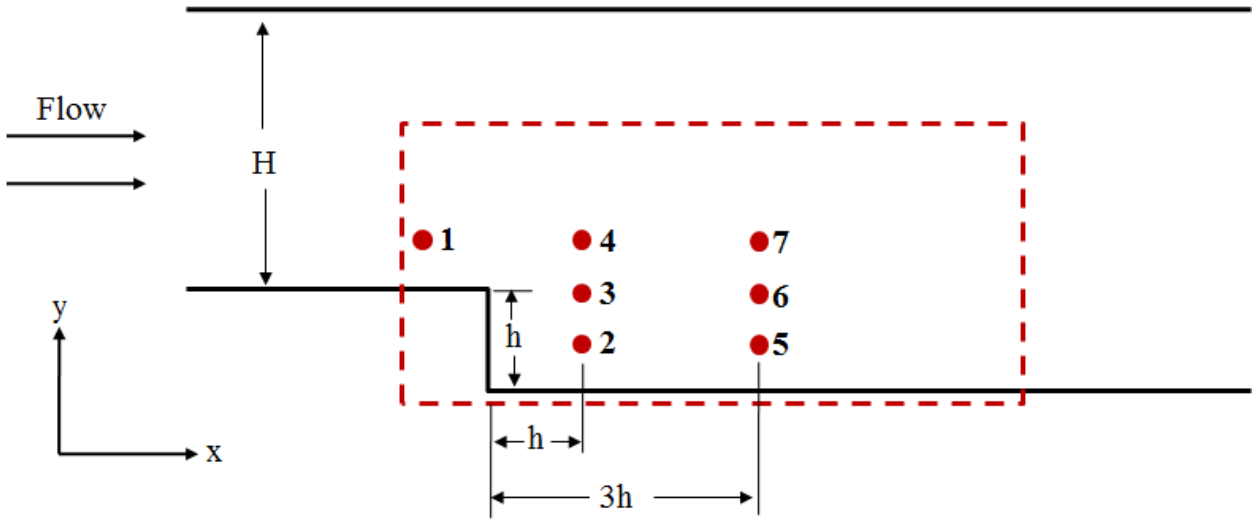

Figure 3.3: Schematic diagram of backward facing step. Red dashed line indicating the measurement region

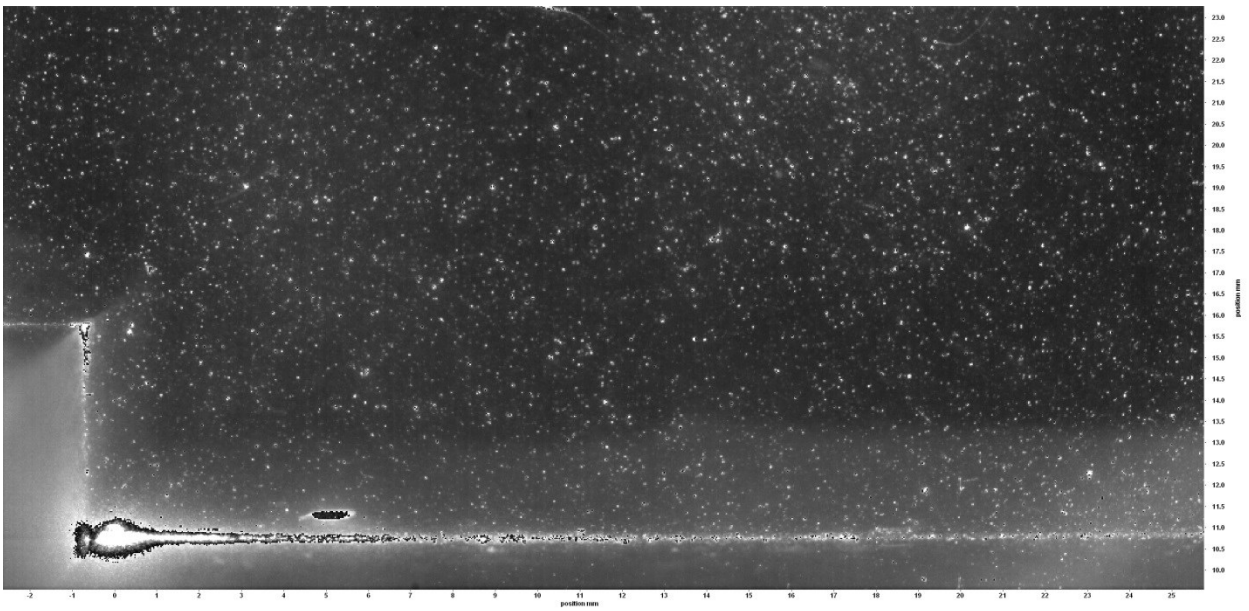

Figure 3.4: Raw image of flow passed the backward facing step captured by PIV

To address resolution issues related to the size of the seeding particles, it is noted here that the particles are indeed quite a bit smaller compared to the Taylor micro-scale thus again supporting the argument that the experiments can indeed resolve some portion of the dissipative scales. In addition, the neutrally buoyant characteristic of polyamide particles satisfies the most ideal conditions noted in Ref. (Mei, 1996) . Another parameter to confirm minimal interference by the seeding particles in affecting turbulence characteristics relates to the mass loading ratio (defined as the ratio of the seeding mass flow rate to the working fluid mass flow rate) (Raffel, Willert, & Kompenhans, 1998). Fluid mass ratio estimate is 4.8×10^{-4} based on the total mass of polyamide particles introduced into the flow circuit. This is very low to have a physical effect on turbulence characteristics based on earlier work by Longmire et al (Longmire & Eaton, 1992).

3.3.4 Image post processing

The measurement field-of-view was a rectangular region of size 5*h* in the streamwise direction and 2.6*h* in the wall normal direction. Figure 3.3 shows a diagram of the field of view relative to the step position. This field of view was specifically chosen to capture the intense free shear region that exists downstream of the step. The Figure also shows seven interrogation points (numbered 1 through 7) the local structure of turbulence through the calculation of probability density functions (PDFs) and second order SFs were probed. These points of interest correspond to regions of varying characteristics of the large-scale anisotropy.

This raw image sequences were pre-processed prior to vector calculations by subtracting a sliding background image, conducting particle intensity normalization, and performing high-pass filtering. This enhanced the image contrast and nearly eliminated spurious vectors. It was found that there were occasional spurious vectors without the pre-processing, which were absent with

the presence of pre-processing. The percentage of accepted vectors was > 95%. Cross-correlation and multi-pass iterative algorithms were chosen to yield a final interrogation window size of 8×8 pixels with 50% overlap to calculate the turbulent 2D time-resolved instantaneous velocity vectors. An in-house Matlab code was developed to post-process these raw velocity measurements to derive statistical properties, specifically PDFs, second order SFs and dissipative scales.

3.4 Error calculations

To further address the issue about how sizeable is the dissipative regime resolved in current experiment, take a look at the probability density function of the local dissipative scale η defined as {η: such that the local Reynolds number $\delta u_\eta \eta/\nu \sim 1$) at each of the points of interest in this experiment for all cases. These computed PDFs, $Q(\eta)$ were then compared to published PDFs available for shear flows and homogenous turbulence. Figure 3.5 shows normalized PDFs of $Q(\eta/\eta_{peak})$ calculated at each of the seven interrogation points for all Reynolds number cases, where η_{peak} is the mode of the distribution. The methodology to compute the PDF was identical to that described by Bailey et al. (Bailey et al., 2009) . Detailed descriptions are also provided later in this chapter. Also included in this figure are published PDFs of the dissipative scales normalized by η_{peak} for homogenous isotropic turbulence by Schumacher (Schumacher, 2007) and those in pipe flow experiments (Bailey et al., 2009). As can be seen, the PDFs measured in current experiment agree well with the known behavior of dissipative scales, further demonstrating that the experiments presented in this work does capture the physical nature of dissipative scales. We also note that when the PDFs are normalized with $\eta_O = LRe_L^{-0.72}$ (L being the local integral length scale and $Re_L = k^{1/2}L/\nu$, where k is the measured turbulent kinetic energy), we observed that

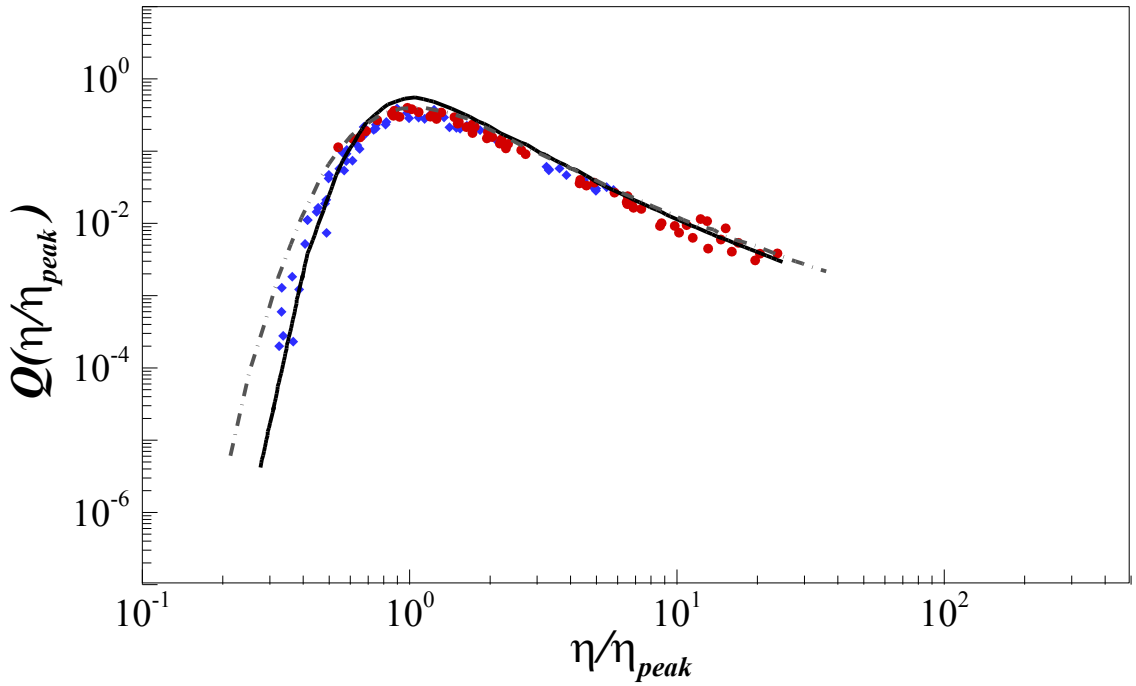

Figure 3.5: Local dissipation scale PDF $Q(\eta/\eta_{peak})$ presented at the seven interrogation points for all three Reynolds number cases. Red circle represents Case I, green inverted triangle represents case II, and blue diamond represents case III. Solid line

the location of the peak consistently scaled with mean shear. Details will be discussed in later chapters.

Table 3.3: Percent error associated with the second-order structure function in the streamwise direction at various r distances

	% Error			
	r_1(0.4 mm)	r_2(2.7 mm)	r_3(4.9 mm)	r_4(7.1 mm)
Position 1	1.5	2.7	2.82	2.32
Position 2	2.55	3.68	1.63	1.6
Position 3	1.01	1.78	2.17	1.17
Position 4	1.17	0.65	2.53	2.94
Position 5	2.25	0.86	2.66	2.53
Position 6	4.16	3.5	3.14	3.99
Position 7	1.28	2.63	3.07	2.09

With respect to errors from statistical convergence based on the finite size of velocity ensembles measured, Table 3.3 lists the percent error in the second order SF in streamwise direction evaluated at four different separations, for each of the seven interrogation points, based the standard deviation of the arithmetic mean of randomly selected sub-set of ensembles. As shown in the Table, the maximum error in the structure function due to statistical convergence is estimated to be less than 5 percent.

3.5 Limitations

Two dimensional particle image velocimetry (PIV) experiments were carried out for current research. To explain more elaborately, in channel with backward facing step fluid was flowing in three dimensional spaces. Two dimensional high speed images were captured at the middle of *z*-axis of the channel. Even though flow dynamics in the channel is three dimensional, two dimensional measurements were performed. These measurements meet the goal of current project, to study the velocity co-relations in *x* and *y* directions.

3.6 Probability Density Functions (PDFs)

3.6.1 Introduction to PDFs

Probability density function (PDF) is continuous random variable that describes the statistical behavior of fluctuating velocity differences. In other words it tells us the probability of a random variable at a certain value range. PDF of a random variable is integral of random variables density

function over a given range. PDF of random variable *X* can be calculated by using equation no 3.1. *X* has range $-\infty < X > \infty$. Probability of *X* was calculated over the interval [a,b]. $f(x)$ is the density function is derivative of cumulative density function (CDF).

$$PDF(a < X > b) = \int_a^b f(x)dx \tag{3.1}$$

3.6.2 Methodology

Probability density function of streamwise velocity, *U* and wall normal velocity, *V* was calculated. Streamwise velocity, $(U-\langle U\rangle)/\sigma_U$ and wall normal velocity, $(V-\langle V\rangle)/\sigma_V$ were normalized using their respective ensemble average and standard deviation. Where $\langle U\rangle$ and $\langle V\rangle$ are the ensemble average; σ_U and σ_V are respective standard deviation. PDF was calculated at seven interrogation points to understand the influences at varying large-scale anisotropy. A matlab code was developed to calculate PDFs.

3.7 Structure Functions (SFs)

3.7.1 Introduction to SFs

Structure function can be defined in terms of velocity increments between two points. Second order structure function covariance is the velocity difference between two successive $x + r$ and x (Pope, 2000). Structure function is widely used to understand the scaling exponent of turbulent flows (Y. Huang et al., 2010; K. R. Sreenivasan & Antonia, 1997) since Kolmogorov's hypothesis (A. Kolmogorov, 1941). Equation 3.2 shows n^{th} order structure function at streamwise direction.

$$\Delta u^n = (U(x + r) - U(x))^n \tag{3.2}$$

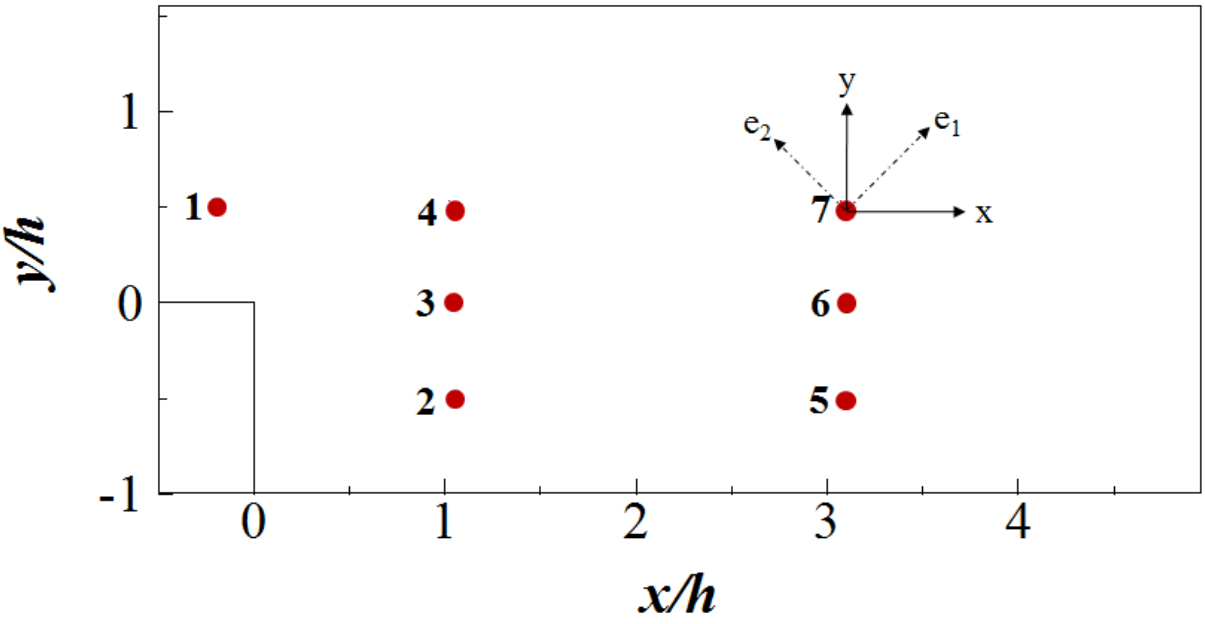

Figure 3.6: Measurement region in Backward facing step with all seven interrogation position. Position 7 shows direction of where second order structure functions were calculated.

3.7.2 Methodology

The second order SFs calculated are defined by the following equation:

$$\langle \Delta u'^2_{\alpha\beta} \rangle (r) = \langle \left(u'(\vec{p} + r\hat{e}_\beta) \cdot \hat{e}_\alpha - u'(\vec{p}) \cdot \hat{e}_\alpha \right)^2 \rangle \tag{3.3}$$

Where $\vec{p}$ is the position of any of the seven interrogation points, $r\hat{e}_\beta$ is the separation vector from the interrogation point to a point r distance away in the $\hat{e}_\beta$ direction. The dot product with $\hat{e}_\alpha$ denotes the velocity component utilized for the SF. Thus $\langle \Delta u'^2_{\alpha\beta} \rangle (r)$ is the second order SF of the α component of the fluctuating velocity in the β direction.

Second order SFs as defined above were computed at the seven interrogation points along four directions namely *i*, *j*, e_1, and e_2, where *i* and *j* are the unit vectors in the *x* and *y* directions, while

e_1 and e_2 represent the calculated principal directions of the symmetric 2D strain rate tensor. Thus eight SFs per interrogation point for each of the Reynolds numbers cases were computed. The logarithmic derivative for each of the SF, defined as $\zeta_{\alpha\beta} = r\frac{d\ ln\ \langle \Delta u'^2_{\alpha\beta} \rangle}{dr}$ was also calculated to represent the spatial variation of the "exponent" characteristics of the calculated SF. Figure 3.6 shows four directions of i, j, e_1, and e_2 for position 7.

Second orders SFs were also calculated in 360° directions at all seven interrogation positions. Figure 3.7 shows schematic of backward facing step and 360° directions where second order structure functions were calculated. Structure functions at 360° directions were only calculated for higher Reynolds number case (Case I) and were calculated for V_r and V_θ velocity component, where r indicates parallel direction of β while θ indicates perpendicular direction of β. β range from 0° to 360°.

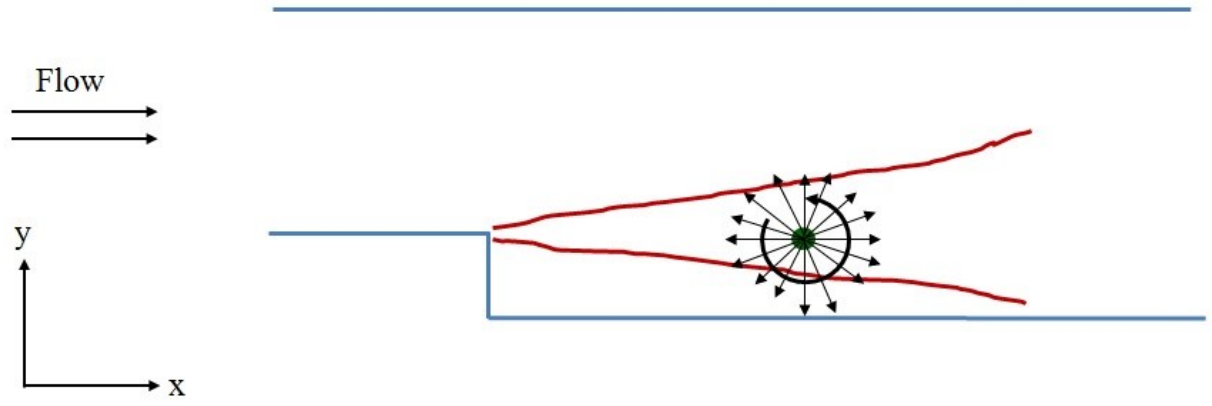

Figure 3.7: Schematic of backward facing step showing position 6 and 360° directions where second order structure functions and two point correlation functions were calculated.

3.8 Two Point Correlation Functions (TPCFs)

3.8.1 Introduction to TPCFs

Two point correction functions is the simplest statistic containing turbulent information on the spatial directions of the random field (Pope, 2000). Attempts were made (De Karman & Howarth, 1938; Taylor, 1935) using two point correlation to understand the energy cascade process in Navier-Stokes equations. Second order structure functions, $\langle(u_1 - u_2)^2\rangle$ can be derived shown in equation 3.4, if we observe the right hand side of the equation 3.4 first two terms, $\langle u_1^2\rangle$ and $\langle u_2^2\rangle$ has impact on large-scale anisotropy. The remaining part is $\langle u_1 u_2\rangle$, that is two point correlation functions. To understand the influence of small-scale contribution it is necessary to calculate the two-point correlation functions.

$$\langle(u_1 - u_2)^2\rangle = \langle u_1^2\rangle + \langle u_2^2\rangle - 2\langle u_1 u_2\rangle \tag{3.4}$$

3.8.2 Methodology

Two point correlations functions are defined by following equations:

$$\rho_{\alpha\beta}(m) = \langle\left(u'\left(\vec{p} + m\hat{e}_\beta\right) \cdot \hat{e}_\alpha \,.\, u'(\vec{p}) \cdot \hat{e}_\alpha\right)\rangle \tag{3.5}$$

Where $\vec{p}$ is the position of any of the seven interrogation points, $m\hat{e}_\beta$is the separation vector from the interrogation point to a point m distance away in the $\hat{e}_\beta$ direction. The dot product with $\hat{e}_\alpha$ denotes the velocity component utilized for the structure function. Thus $\rho_{\alpha\beta}(m)$ is the two point correlation of the α component of the fluctuating velocity in the β direction.

Two point correlation functions were also calculated in 360° directions at all seven interrogation positions. Figure 3.7 shows schematic of backward facing step and 360° directions where two point correlation functions were calculated. Two point correlations functions at 360° directions were only calculated for higher Reynolds number case (Case I) and were calculated for V_r and V_θ velocity component, where r indicates parallel direction of β while θ indicates perpendicular direction of β. β range from 0° to 360°.

3.9 Lacunarity & Intermittency

3.9.1 What is Lacunarity?

Lacunarity, $\Lambda(\lambda)$ means gap or pool, which was derived from the word "lake". The distribution of gap size has been termed as lacunarity by Mandelbrot (Mandelbrot, 1983) . Measurement of "gappiness" or "hole-iness" in geometric structure is lacunarity (Kaye, 1989). A geometric structure is considered more lacunar if the gap sizes are distributed over a greater range (Plotnick, Gardner, & O'Neill, 1993). Lacunarity analysis is a multi-scaled method for describing patterns of spatial dispersion that can be used for both binary and quantitative data set in one dimension, two dimensions or even three dimensions. For this current study lacunarity was calculated for one dimensional data set of turbulent kinetic energy dissipations, ε. Lacunarity analysis is applicable for both non-fractal and multi-fractal distributions (Plotnick, Gardner, Hargrove, Prestegaard, & Perlmutter, 1996). Low lacunarity means objects are homogeneously and translationally invariant as the gap sizes are same, whereas higher lacunarity means objects are heterogeneous and not translationally invariant as gap sizes are wide (Gefen, Meir, Mandelbrot, & Aharony, 1983). Lacunarity is scale dependent measurements technique; a heterogeneous object at small-scales can

be homogenous when the scale is large. Alternately a homogenous object can turn to heterogeneous when the scale is decreased.

Several methods have been proposed for lacunarity calculations by Mandelbrot (Mandelbrot, 1983), Gefen et al(Gefen et al., 1983) , Lin and Yang (Lin & Yang, 1986), Allain & Cloitre (Allain & Cloitre, 1991). Among all the methods gliding-box algorithm method is most straightforward which was proposed by Allain & Cloitre. This method was adapted for current study to calculate lacunarity of instantaneous dissipation rate signals. Sliding-box methods can be easily described for one dimensional data set. Let's assume we have a data set *x* that has 10 variables. λ is the radius (here length, as 1D) of the box, the values can be 1, 2, 3…… . *C* = mean × standard deviation of series x. Later on, a new binary series qualifying criteria is >= *C* was established. From that series sum all the binary inside each radius. This new series is *m* or mass series. Then calculating standard deviation and mean of the mass series lacunarity can be calculated using equations 3.4. The ratio of second moment to the square of the average of the spatial mass-distribution function is defined as lacunarity. Similarly, lacunarity can be calculated varying the λ sizes. Later on lacunarity, Λ can be plotted at varying box radius, λ. For current study the raw dissipation signal is converted into a binary signal via a pre-set threshold. Given a box radius (time scale) λ, the mass signal is obtained as the integral of the binary signal within the window. As the window slides across the entire time-series, the mass signal fluctuates. Lacunarity $\Lambda(\lambda)$ is then calculated using equation 3.4. Physically, $\Lambda(\lambda)$ reflects the level of inhomogeneity and intermittency in the signal.

$$\Lambda(\lambda) = \frac{\int_{m=0}^{\infty} m^2 \, pdf_{\lambda}(m)dm}{(\int_{m=0}^{\infty} m^2 \, pdf_{\lambda}(m)dm)^2} = 1 + \frac{\sigma_m^2}{\mu_m^2} \tag{3.6}$$

Where, σ is the standard deviation and μ is the mean of mass series.

3.9.2 What is Intermittency?

A signal becomes intermittent when it stops from time to time and starts again. It can be also defined as irregular alternation of phases of signals. Intermittency is very common in turbulent flows and also one of the most challenging problems in turbulence. Physically lacunarity, $\Lambda(\lambda)$ reflects the level of inhomogeneity and intermittency in signals. Lower lacunarity means mass signal fluctuates less relative to its mean and alternately higher lacunarity means mass signal fluctuates more relative to its mean in higher lacunarity case.

3.9.3 Intermittency in turbulent flows

Intermittent spatio-temporal fluctuations of the instantaneous velocity gradient field are canonical to all turbulent flows. Probability density function of velocity gradient in turbulent flow is not Gaussian, tails of PDF becomes stronger with increase of Reynolds number (Jiménez, 2007; Lohse & Grossmann, 1993). Intermittency of turbulent flows is not only limited to velocity gradient but also present in the turbulent kinetic energy dissipation rate field ε. Intermittency of energy dissipation rate can also be described in terms of a corresponding instantaneous fluctuating dissipation scale η. Detailed description of dissipation scale is provided in the next section. Several techniques like cascade model, breakdown coefficient model can be used to describe intermittency in turbulent flows (Jiménez, 2007). Cascade model includes multi-fractal model, (She & Orszag, 1991) multiplicative models, (Benzi, Biferale, & Toschi, 2003) limiting distribution model. Imperfect multiplicative process (Jiménez, 2000; Jiménez & Wray, 1998) can be an example of breakdown coefficient models (Meneveau & Sreenivasan, 1991).

Intermittency of velocity differences increases in turbulent channel flow traveling from center to wall of the channel where vertical structure and strong mean shear are present. This was confirmed by Toschi et al, they studied direct numerical simulation of channel flow (Toschi, Amati, Succi, Benzi, & Piva, 1999). In their study they used scaling exponents of longitudinal streamwise structure function as quantitative indicator of intermittency. Characteristic length scale L_s was proposed. L_s can be defined as square root of the mean energy dissipation and the mean shear rate. Intermittency increases when scales $r \geq L_s$ compared with homogeneous isotropic turbulence. Intermittency of shear dominated flows was also observed by Gualtieri et al. (Gualtieri, Casciola, Benzi, Amati, & Piva, 2002) . They proposed a new approach to classical Kolmogorov-Obukhov refined similarity hypothesis (A. N. Kolmogorov, 1962) that was able to predict the intermittency in dissipation field. Instantaneous production of turbulent kinetic energy is solely responsible for intermittency of velocity increments in shear-dominated flows.

Intermittency generation is observed in three dimensional Navier-Stokes turbulence, which can be well defined using cascade model (Jiménez, 2007). Different systems are available either to qualitative understanding or quantitative understanding of the physical process of intermittency behavior. Intermittency is also observed in turbulent mixing of a passive scalar. Turbulent mixing is pretty common phenomenon in turbulent heat transfer and in atmospheric pollutants dispersion.

3.10 Dissipative scales

3.10.1 Overview

Intermittency of energy dissipation rate can also be described in terms of a corresponding instantaneous fluctuating dissipation scale η. This fluctuating dissipation scale may be defined as

η. This fluctuating length scale η as the cut-off scale is different from the classical dissipative scale $\eta_K = (\nu^3/\langle\varepsilon\rangle)^{1/4}$ proposed by Kolmogorov (A. Kolmogorov, 1941). Where ν is kinematic viscosity of fluid and $\langle\varepsilon\rangle$ is the mean kinetic energy dissipation energy rate. Physically, η is the instantaneous cut-off scale where viscosity overwhelms inertia. Paladin and Vulpiani proposed dissipation length scale η to bridge connections between dissipative scales and localized turbulent flows (Paladin & Vulpiani, 1987). The local Reynolds number corresponding to dissipative scale η is 1: $Re_\eta = \eta\delta_\eta u/\nu \approx 1$; where $\delta_\eta u = |u(x + \eta) - u(x)|$ is the longitudinal velocity increment (Yakhot, 2006; Yakhot & Sreenivasan, 2005).

3.10.2 Methodology

Two paradigms can be used to capture the dynamics of dissipative structures: (1) through a continuous distribution of dissipative scales represented by its probability density function (PDF) $Q(\eta)$, or (2) of a single dissipative scale η_K; both predict a form of universal structure of turbulence at the small-scales provided that the intermittency characteristics of ε is universal (i.e., independent of the large-scale). Equivalently, the small-scale structure of turbulence is universal if the distribution $Q(\eta)$ has a form independent of the large-scales. Identifying this universal form has been the quest of the statistical theory of turbulence for sufficiently large Reynolds numbers. Yakhot derived an analytical form for $Q(\eta)$ by applying the Mellin transform properties to the structure function exponent relationships for moments of $\delta_\eta u$, combined with the Gaussian assumption (Yakhot, 2006, 2008). This analytical estimate for high Reynolds number was constructed by utilizing an experimental fit to the measured behavior of the scaling exponent, $\xi_n(n)$ in isotropic flows, where n is the order of the moment. η range was proposed $0 < \eta < L$ to calculate probability density function $Q(\eta)$ of η, where L is the integral length scale of turbulence.

Established methodology published previously was closely followed to calculate PDF of dissipative scale, η (Bailey et al., 2009; P. E. Hamlington et al., 2012; Schumacher, 2007; Q. Zhou & Xia, 2010) . Qualification criteria were set $0.9 \leq \frac{(u_r-u_0)(x_r-x_0)}{\nu} \geq 2$ to calculate η, where u_r-u_0 is velocity differences and x_r-x_0 is spatial differences. Once this criteria was satisfied $\eta = x_r$-x_0 was calculated. $\eta_0 = LRe_L^{-0.72}$ was calculated to normalized η, where Re_L is the Reynolds number based on integral length scale. Following series of equations were used to calculateRe_L.

$$\lambda_f = \left[\frac{f(x_0)-f(x_2)}{4\Delta x^2}\right]^{-\frac{1}{2}} \tag{3.7}$$

$$\lambda_g = \frac{\lambda_f}{\sqrt{2}} \tag{3.8}$$

$$Re_\lambda = \frac{\sqrt{k}\,\lambda_g}{\nu} \tag{3.9}$$

$$Re_L = \frac{3Re_\lambda^2}{20} \tag{3.10}$$

Where λ_f is longitudinal Taylor microscale, Δx is spatial grid distance, λ_g is transverse Taylor mixrocalse, Re_λ is Taylor Reynolds number, k is turbulent kinetic energy. With this η_0 probability density function $Q(\eta/\eta_0)$ was calculated to measure the intermittency effect in presence of strong mean shear, this is described in detail in chapter 6.

3.11 Summary

In summary, experimental details performed for current study were discussed. Two dimensional particle image velocimetry experiments were performed for two different Reynolds number cases. Polyamide seeding particles were used with mean diameter of 20 μm. Image post processing

technique was discussed briefly. Error calculation was performed and PDF of dissipative scales was compared with previous published results to boost the confidence of current experiment. Introduction and details methodology of Probability density functions, Structure functions, and dissipations scales were discussed. Dissipation scales were calculated using Yakhot's derived (Yakhot, 2006) analytical forms that uses Mellin transformation. Lacunarity measures the homogeneity of any signals. Gliding box method was used to calculate the lacunarity of turbulent kinetic energy dissipation. Lacunarity measurement provides the physical understanding of intermittent nature of turbulent flows. Intermittency nature of turbulent flow was discussed and short literature review on intermittency in turbulent flows was provided in this chapter.

Chapter 4

MEAN FLOW & ANISOTROPY

4.1 Introduction

As mentioned earlier, classical case of turbulent flow past a backward facing step was utilized for current study. While this case has been utilized primarily to study and model separated turbulent flows, the simplicity of the geometry and its strong anisotropic nature particularly in the free shear layer downstream of the step provides an opportunity to interrogate the local properties of the small-scale structure of turbulence. The experiments described in Chapter 4 provide a well-defined strongly anisotropic turbulent flow over a modest range of Reynolds numbers. In this chapter mean flow characteristics of backward facing step along with anisotropy behavior of large-scale were discussed.

4.2 Mean flow characteristics

4.2.1 Mean velocity

Figure 4.1 shows the comparison of the normalized mean streamwise velocity profiles extracted at $x/h = 4$ for both Reynolds numbers with those from the previous work of Jovic and Driver (Sbra Jovic & Driver, 1994) and Le, Moin et al.(Le et al., 1997). As can be seen, the agreement is good, and any deviation observed may be attributed to the difference in Reynolds number. Figure

4.2 and 4.3 compare the corresponding standard deviation profiles of the streamwise and wall-normal velocity components again depicting reasonable agreement.

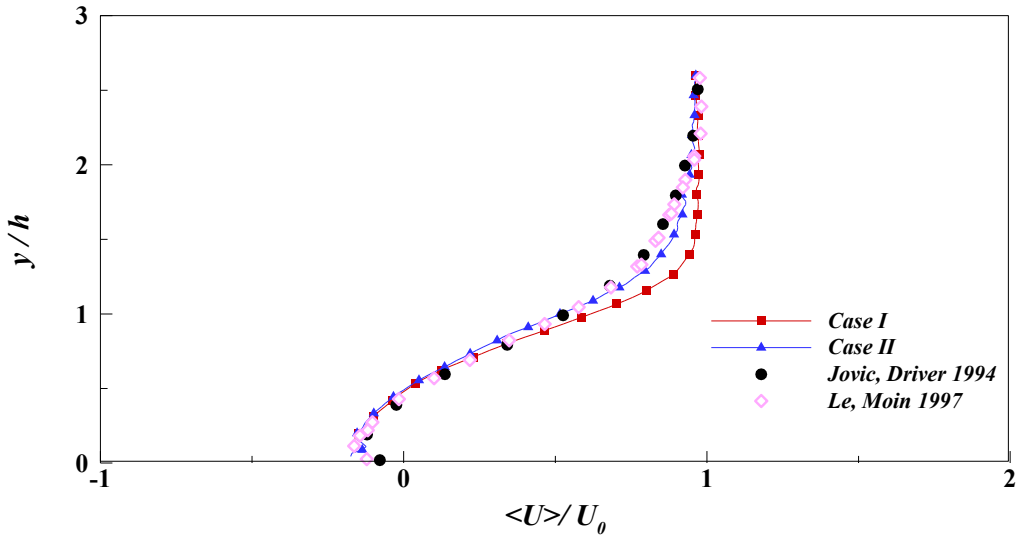

Figure 4.1: Mean streamwise velocity profile comparison at x/h = 4. Profiles are shown for Case I (Red square) , Case II (blue triangle) of current study. Profiles are compared with revious published results of Jovic and Driver (1994)(Re_h = 5,000) (Black circle) and Le et al. (1997) (Re_h = 5,100) (pink diamong)

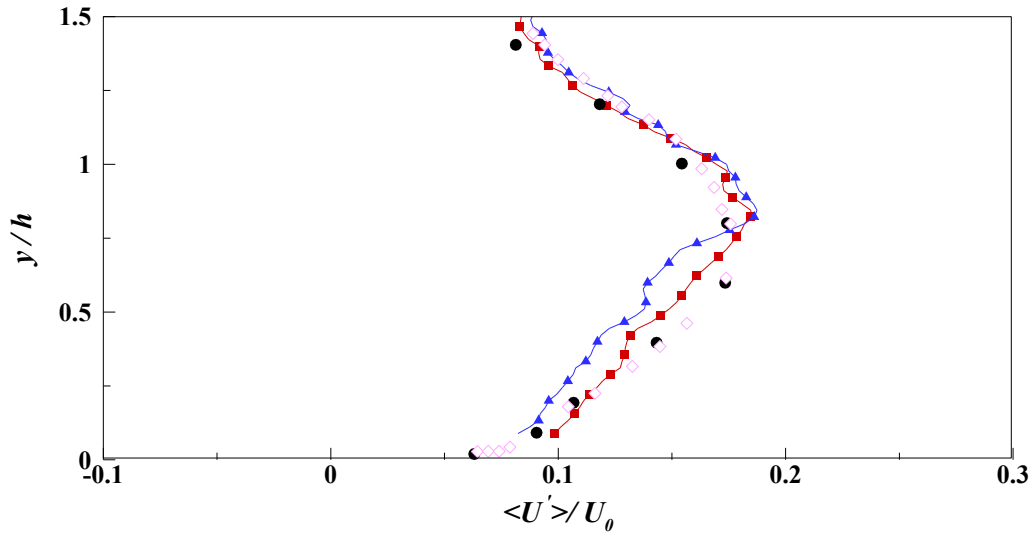

Figure 4.2: RMS streamwise velocity profile comparison at x/h = 4. Profiles are shown for Case I (Red square), Case III (blue triangle) of current study. Profiles are compared with previous published results of Jovic and Driver (1994) (Re_h = 5,000) (Black circle) and Le et al. (1997) (Re_h = 5100) (pink diamond)

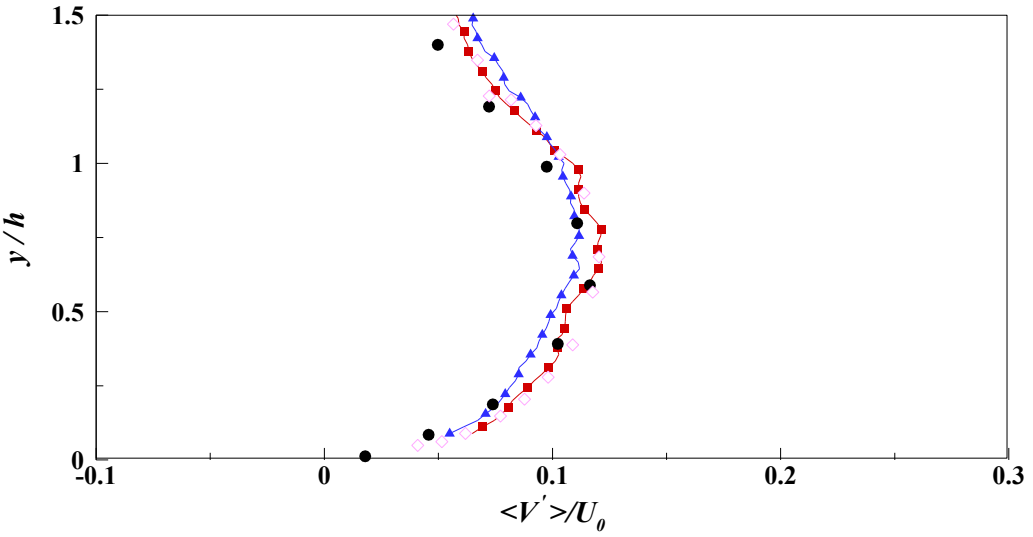

Figure 4.3: RMS wall-normal velocity profile comparison at x/h = 4. Profiles are shown for Case I (Red square), Case III (blue triangle) of current study. Profiles are compared with previous published results of Jovic and Driver (1994) (Re_h = 5,000) (Black circle) and Le et al. (1997) (Re_h = 5,100) (pink diamond)

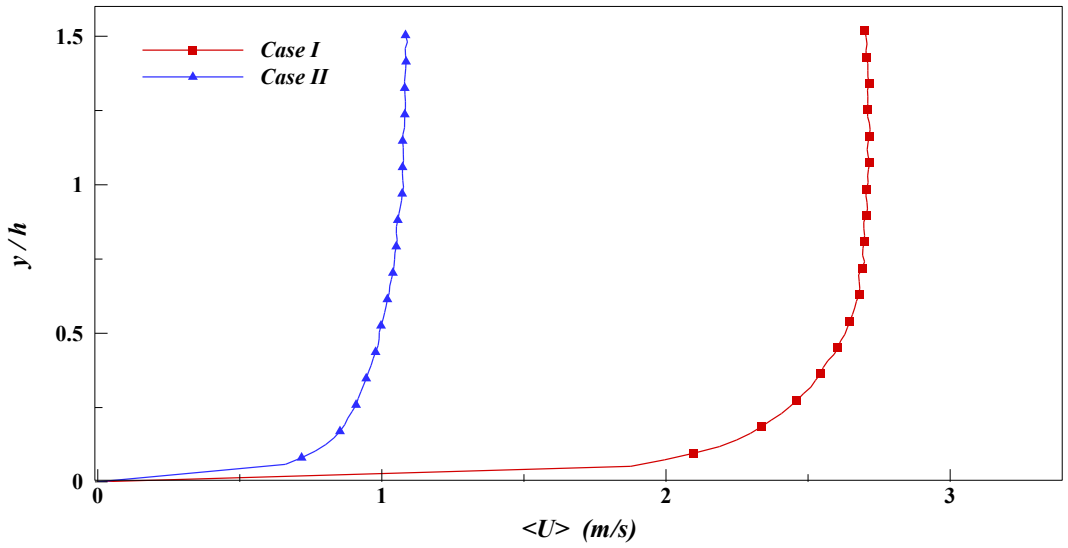

Figure 4.4: Mean streamwise velocity profile comparison before the step at x/h = -0.3. Profiles are shown for Case I (Red square), Case (blue triangle) of current study

To better define the upstream conditions for the three Reynolds number cases, Figure 4.4 shows the mean streamwise velocity profiles extracted immediately upstream of the backward step (at $x/h = -0.3$). These profiles correspond to fully developed channel flow profiles with a well-developed logarithmic layer (Figure 4.5). Based on these profiles and application of the Clauser plot technique to determine shear velocity, we report the boundary layer Reynolds number, Re_τ corresponding to each of both cases in Table 3.1. From the near wall velocity profile (Figure 4.5) it was observed that both the Reynolds number cases clearly follow log-law profile at inner layer.

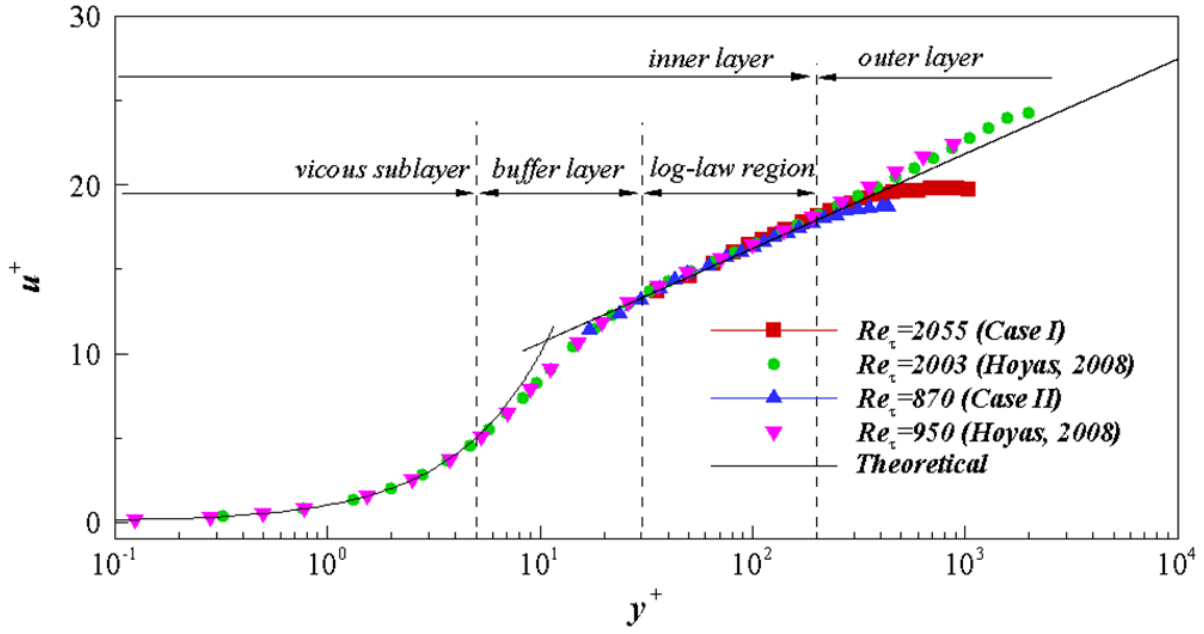

Figure 4.5: Near wall velocity profile comparison before the step at x/h = -0.3. Profiles are shown for Case I (Red square), Case II (blue triangle) of current study and compares with theoretical study, channel flow DNS done by Hoyas et. al. at comparable Re_τ. Black line indicates theoretical profile, green circle indicates Re_τ =2003(Hoyas et. al. 2008) and pink triangle indicates Re_τ =950 (Hoyas et. al. 2008)

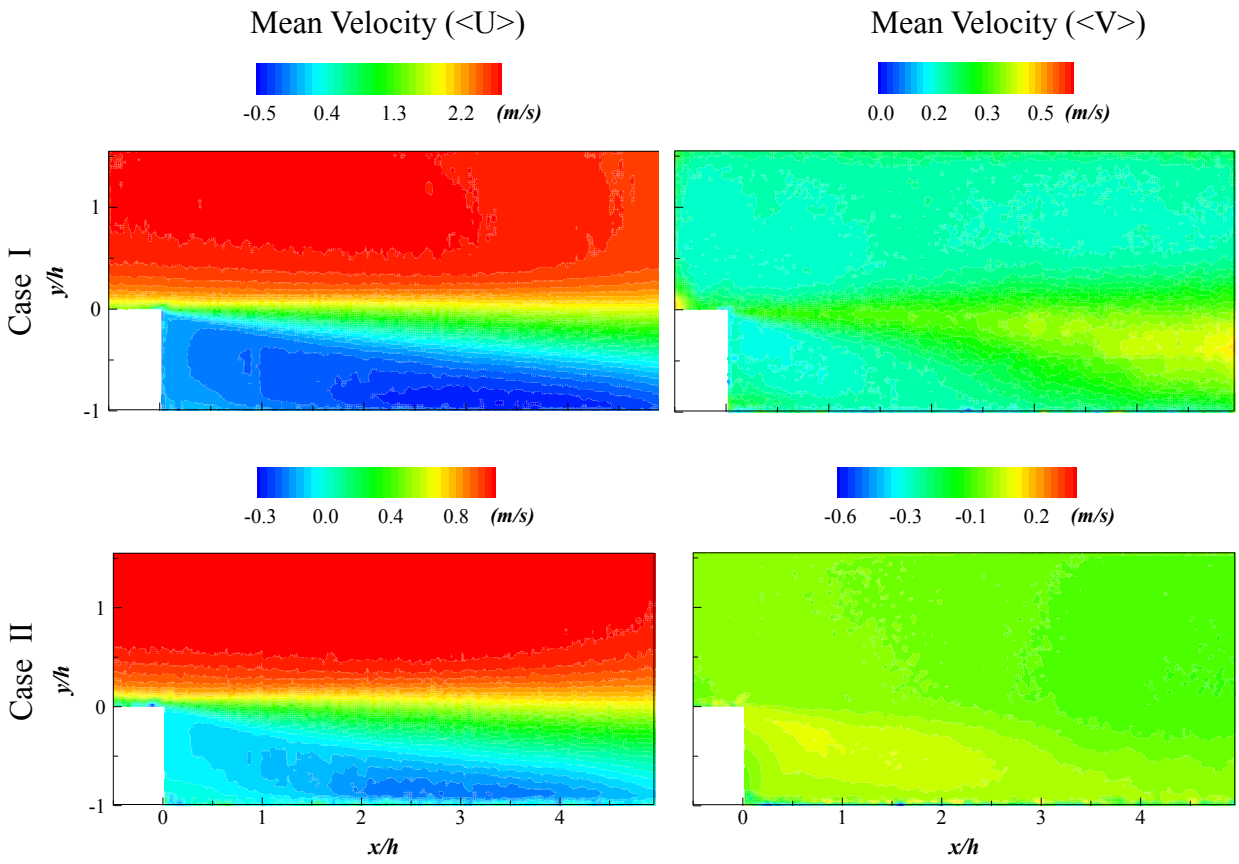

Figure 4.6: Mean velocity contours presented for all Reynolds number cases

4.2.2 RMS of fluctuation velocity

Figure 4.6 shows mean velocity contour plots of the streamwise and wall-normal and figure 4.7 shows root mean square (rms) of the velocity components for both Reynolds number cases. As seen in the figure, the maximum measured streamwise velocity, U occurs in the free-stream region above the step while the maximum wall-normal velocity, V occurs in the recirculation region. As expected, the shear layer starts at the edge of the step and increases in its wall-normal extent in the streamwise direction.

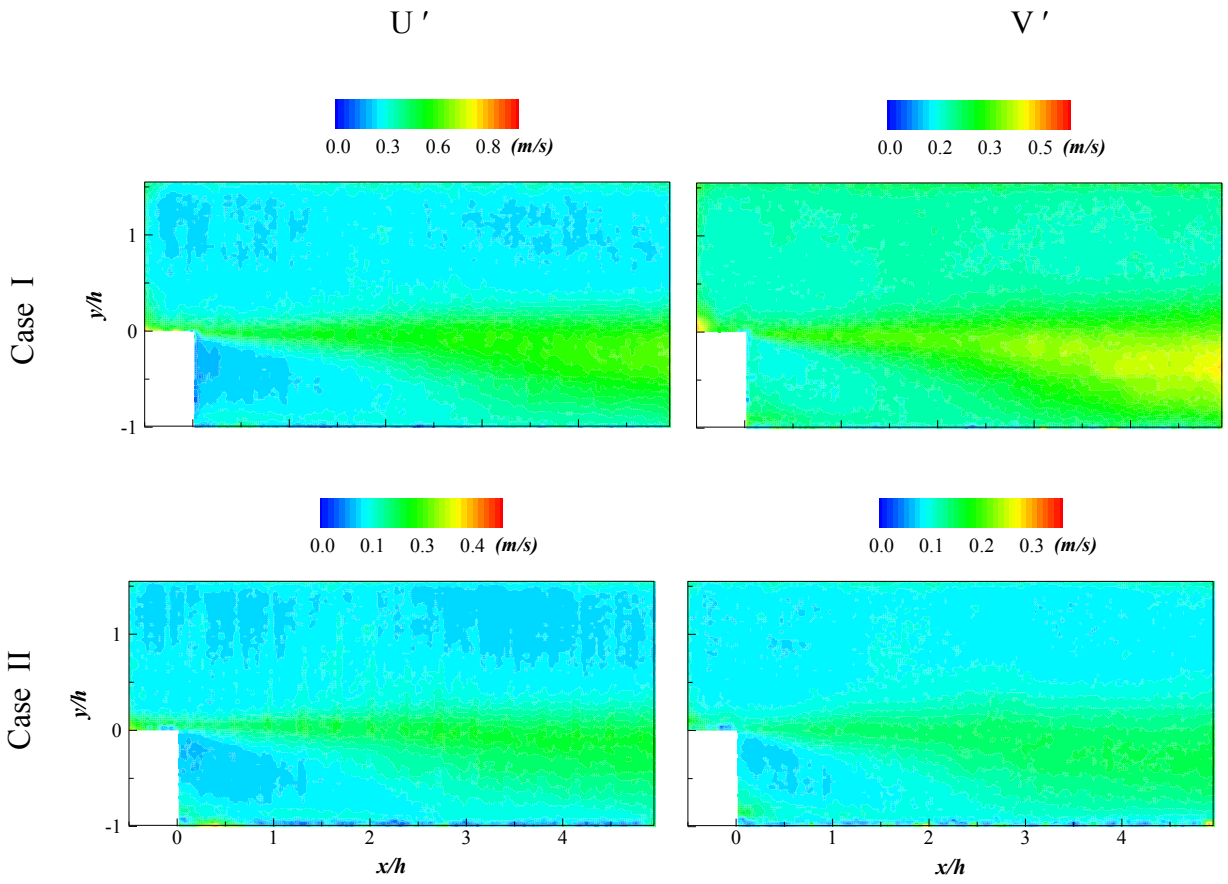

Figure 4.7: RMS velocity contours presented for all Reynolds number cases

The region between the wall and the shear layer contains a large primary vortex region. While the mean flow showed a large vortex region, instantaneous time-resolved measurements showed a highly unsteady recirculation region with many coherent vortices. This is consistent with previous work of Huang et al. (Y. X. Huang et al., 2010). Increase in Reynolds number intensifies the recirculation region. From all two Reynolds number measurements, the reattachment length is

found to be $> 5h$ distance consistent with the findings from previous researchers (Sbra Jovic & Driver, 1994).

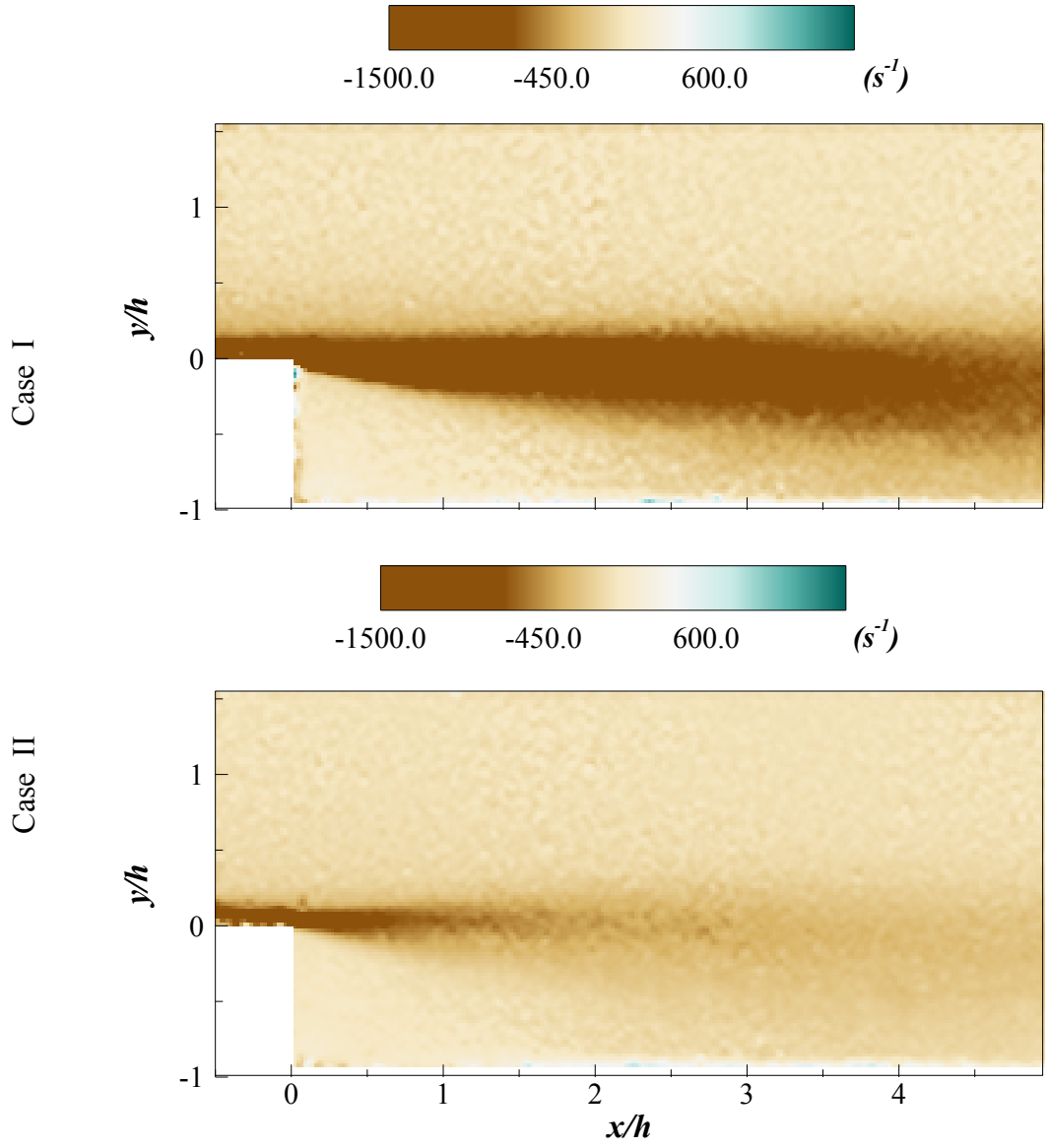

Figure 4.9: Mean vorticity contours presented for all Reynolds number cases

From the contours of rms fluctuations velocities U' and V' (Figure 4.7), it can be easily seen that the turbulent fluctuations are most intense in the shear layer and the width of shear layer increases in wall-normal span in the downstream direction. At both Reynolds number cases U' and V' possess higher values towards the reattachment region. This phenomenon was also found by Le, Moin et al. (Le et al., 1997) and is attributed to large-scale fluctuations associated with the highly unstable nature of the re-attachment region expected due to adverse pressure gradient resulting from the channel expansion. Figure 4.8 represents mean vorticity contours for both Reynolds number cases. It can be observed clearly that at higher Reynolds number vorticity intensity is more pronounced than at lower Reynolds number.

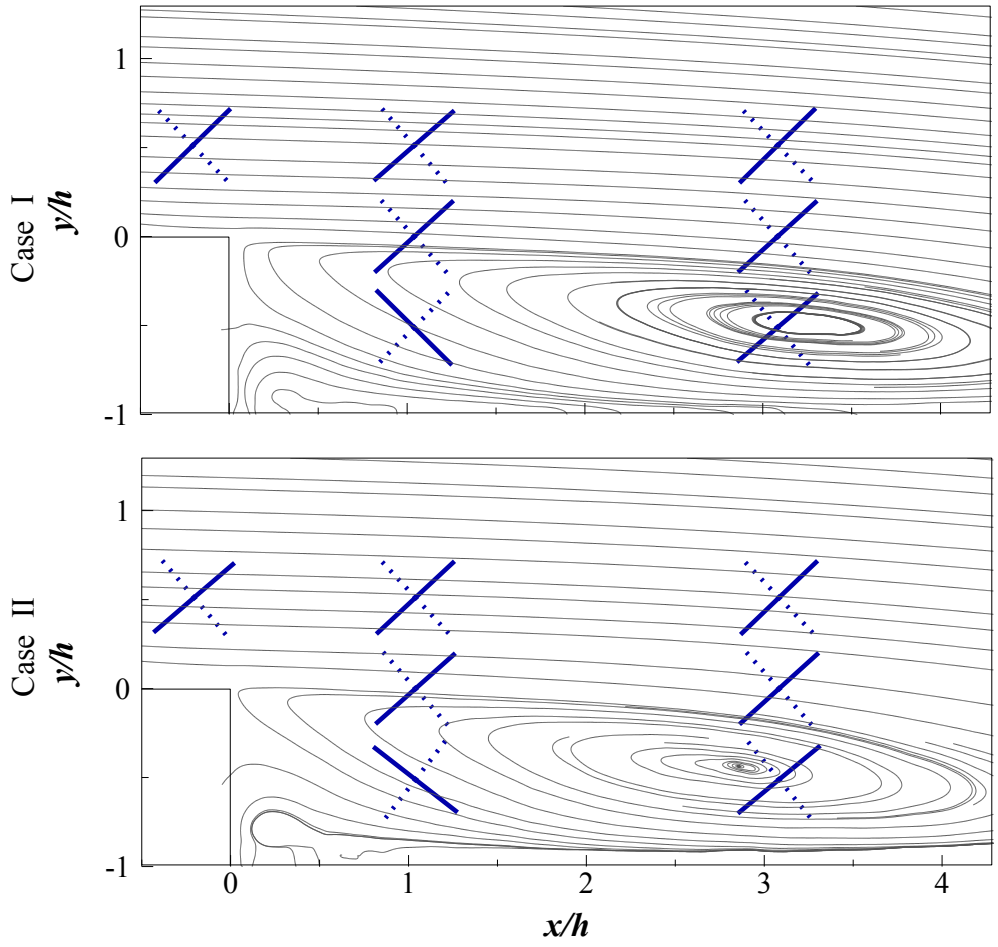

Figure 4.10: Principal axis along stretch (solid line) and contraction (dashed line) at the seven interrogation points.

Table 4.1: Magnitude of eigenvectors (λ_1) in s^{-1}

	Position 1	Position 2	Position 3	Position 4	Position 5	Position 6	Position 7
Case I	80.56	70.00	428.68	67.57	193.14	319.06	45.73
Case II	54.49	17.41	153.71	41.88	69.40	118.69	35.35

Table 4.2: Angle in degrees of e_1 and e_2 unit vectors with respect to x axis

	Position 1		Position 2		Position 3		Position 4		Position 5		Position 6		Position 7	
	e_1	e_2	e_1	e_2	e_1	e_2	e_1	e_2	e_1	e_2	e_1	e_2	e_1	e_2
Case I	45.68	-44.32	-45.36	44.64	47.80	-42.20	48.96	-41.04	49.74	-40.25	47.88	-42.12	45.56	-44.43
Case II	49.39	-40.61	-52.15	37.84	48.42	-41.57	47.05	-42.95	50.59	-39.41	47.94	-42.06	46.28	-43.72

4.3 Large-scale anisotropy

4.3.1 Mean shear effects on deformation axis

To characterize the large-scale anisotropy, we rely on the characteristics of local mean shear field. Given that the measurements are along the channel centerline, the mean shear only exists in the measurement plane from symmetry arguments. Presence of mean shear imposes a local deformation through the pure shear in action as well as rotation of the turbulent eddies. The eigen vectors of the mean strain rate tensor therefore define the principal axis of stretching and contraction of the advected turbulent eddies. Figure 4.9 shows the calculated principal directions of the mean strain rate tensor at the seven positions for the three cases. The solid line (e_1 direction) represents the stretching direction while the dashed line (e_2 direction) represents contraction. Notice that the direction of principal axis is consistent between the six positions 1, 3, 4, 5, 6 & 7 for the three Reynolds numbers. Given that position 2 is located in the separated vortex region, stretching occurs along the azimuthal direction of the vortex. The magnitude of the eigen values is Reynolds number dependent with increasing magnitude noted for increasing Reynolds number. Table 4.1 provides the magnitude of the eigen value corresponding to the principal stretch direction. In addition, Table 4.2 provides the angles e_1 direction and e_2 direction make with respect to the x axis. As noted in the table the greatest stretching occurs at position 3 and 6 relative to the other five positions for any Reynolds number. It may therefore be hypothesized that the turbulent eddies passing through these shear layers undergo the most influence of the mean deformation fields than at any of the other points. Comparing position 2 and 5, position 5 experiences the more stretch which can be explained by its proximity to the much wider nature (in the wall-normal direction) of the shear layer at its corresponding streamwise location.

4.4 Summary

In summary, Mean flow characteristics and large-scale anisotropy in channel flow with a backward facing step were investigated and explained. Velocity profile shows very good agreement with previous DNS (Le et al., 1997) and experimental results (Sbra Jovic & Driver, 1994). At upstream of the channel fully developed turbulent flow was observed. Well-developed log-law profile was observed at the same location. Primary vortex region is located beneath the intense shear region, this was inconsistent with previous literature (Y. X. Huang et al., 2010). Principal axes directions of seven interrogations positions were calculated and found consistent with each other except position 2. This position is located in the recirculation region.

Chapter 5

STRUCTURE FUNCTIONS AND TWO POINT CORRELATION FUNCTIONS

5.1 Introduction

The goal of this chapter is to elucidate variations in the local structure of turbulence, through second order structure functions and two point correlations functions, in the presence of strong large-scale anisotropy. The large-scale anisotropic properties of the measured flow fields followed by the local structure of turbulence at the seven points of interest shown in Figure 3.6 was described in details. Emphasis is on characterizing the variations in the local structure as described by second order structure functions in the dissipative as well as non-dissipative length scale regime. Exponents of second order structure functions were also analyzed at all seven interrogation positions.

5.2 Probability density function (PDFs)

Normalized probability density functions of velocity components for the seven positions for both Reynolds numbers were calculated and are shown in Figure 5.1. Figure also shows the normal distribution. As can be seen, a subtle difference was observed in PDFs in relation to the skewness in the tails. While it is clear that the shape of velocity PDFs are influenced by varying large-scale anisotropy, understanding the mechanism behind this effect requires closer investigation with respect to the local structure via structure functions.

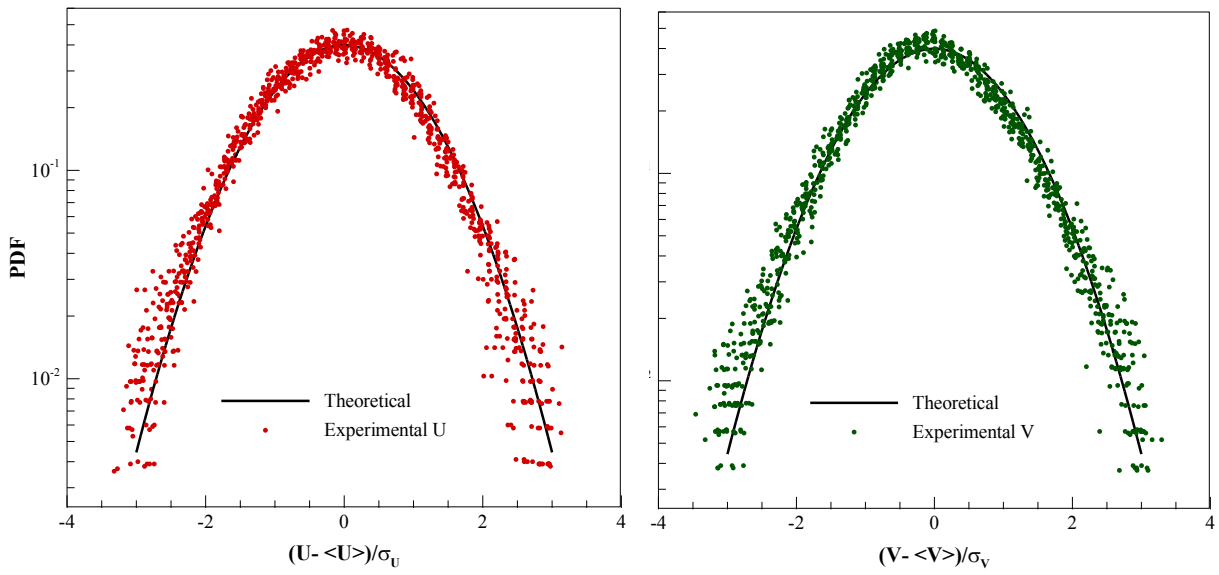

Figure 5.1: Normalized probability density function of streamwise velocity (a) and wall-normal velocity (b). Solid line indicates normal distribution. σ_U and σ_V correspond to the respective standard deviation

5.3 Second order structure function (SFs)

Figure 5.2 – 5.4 show the second order structure functions (SFs) in the *i* and *j* directions for the seven interrogation points. Figure 5.5 – 5.7 show the corresponding second order SFs in the e_1 and e_2 directions for the same points. All plots include the Taylor micro-scale as well as another length scale based on energy dissipation rate, ε and mean shear rate, S, denoted $L_{S,\varepsilon} = (\langle\varepsilon\rangle/S^3)^{1/2}$. The dissipation rate was estimated as $\varepsilon \cong \langle 3\nu(s_{11}^2 + s_{22}^2) + 12\nu s_{12}^2\rangle$, with the isotropic assumptions $\langle s_{13}^2\rangle = \langle s_{23}^2\rangle = \langle s_{12}^2\rangle$, and $\langle s_{33}^2\rangle = 0.5(\langle s_{11}^2\rangle + \langle s_{22}^2\rangle)$. This length scale has been previously implicated to play a role in anisotropic contributions from the large-scale to the small-scale (Khandakar Niaz Morshed, Venayagamoorthy, & Dasi, 2013; Toschi et al., 1999). All functions in general increase with spatial separation distance at the small-scales as expected for SFs. The

variations at larger spatial separations however appear dependent between different points presumably due to growing impacts of discrepancies from the anisotropic effects. Nevertheless, it is clear that increasing Reynolds number increases the overall magnitude of the SFs due to increased turbulence intensities as would be anticipated.

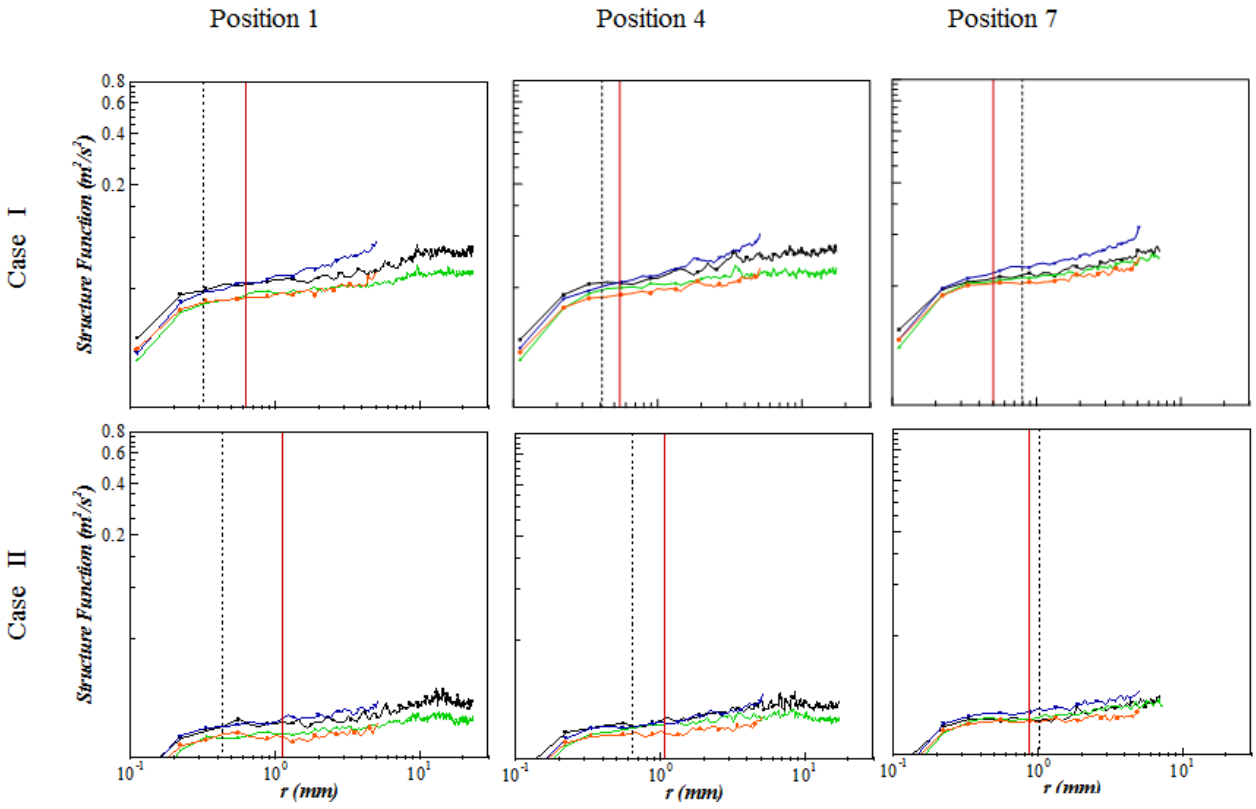

Figure 5.2: Second-order structure function in streamwise and wall normal directions. Black square represents $\langle \Delta u_{ii}^2 \rangle$*, green triangle represents* $\langle \Delta u_{ji}^2 \rangle$*, blue inverted triangle represents* $\langle \Delta u_{ij}^2 \rangle$*, and orange circle represents* $\langle \Delta u_{jj}^2 \rangle$*. Red solid line corresponds to Taylor micro-scale,* λ *while black dash line corresponds to* $L_{S,\varepsilon}$*.*

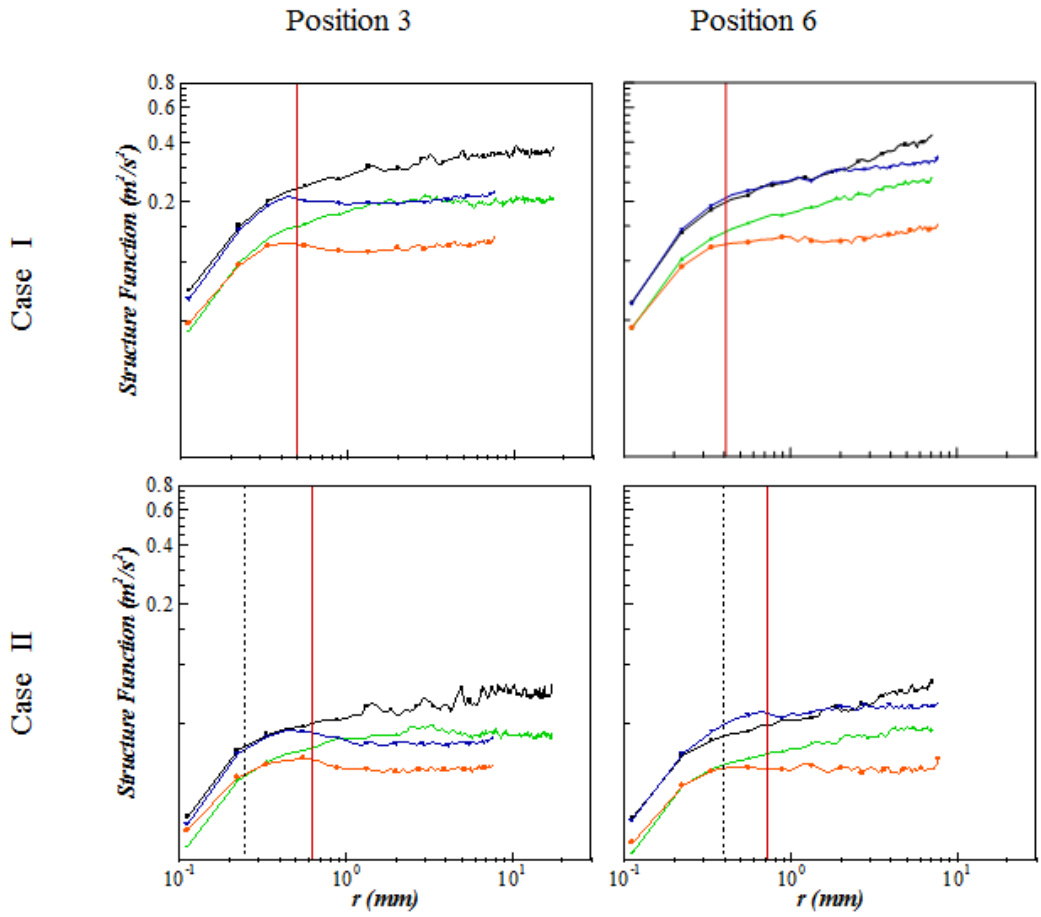

Figure 5.3: Second-order structure function in streamwise and wall normal directions. Black square represents $\langle \Delta u_{ii}^2 \rangle$*, green triangle represents* $\langle \Delta u_{ji}^2 \rangle$*, blue inverted triangle represents* $\langle \Delta u_{ij}^2 \rangle$*, and orange circle represents* $\langle \Delta u_{jj}^2 \rangle$*. Red solid line corresponds to Taylor micro-scale,* λ *while black dash line corresponds to* $L_{S,\varepsilon}$*.*

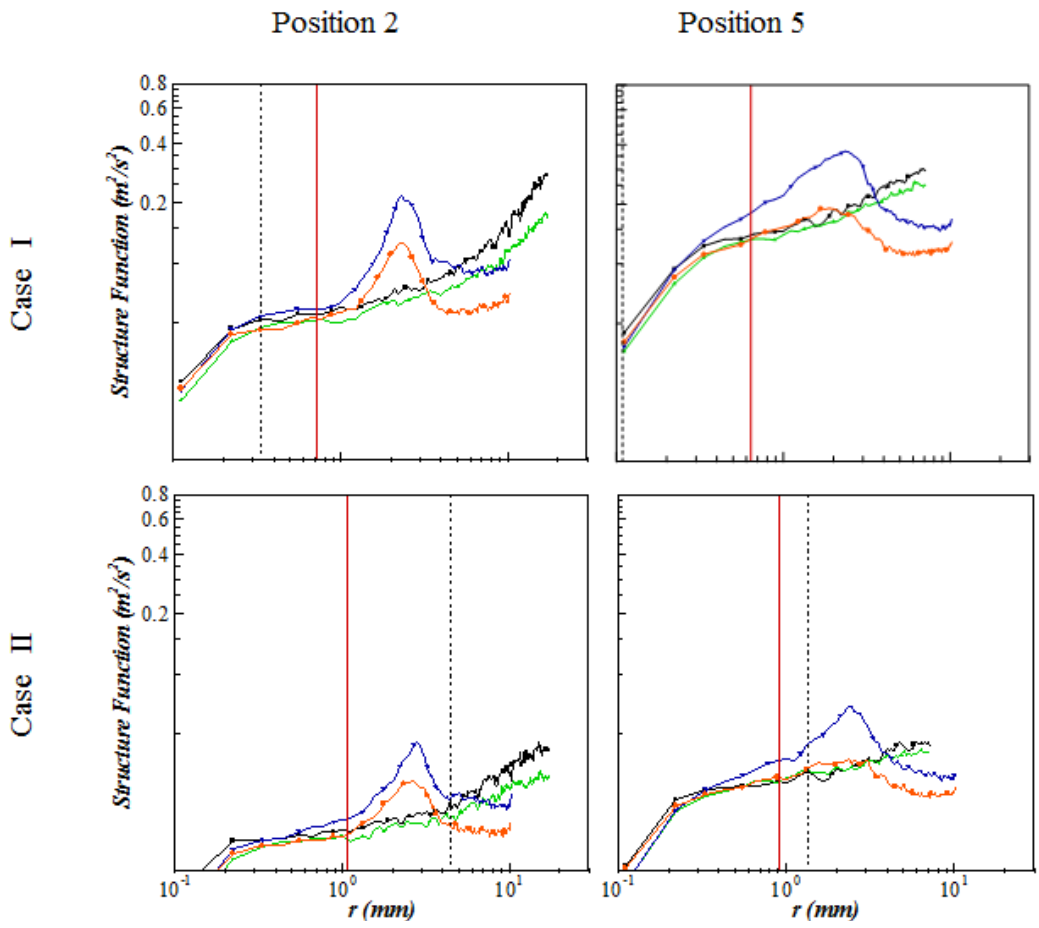

Figure 5.4: Second-order structure function in streamwise and wall normal directions. Black square represents $\langle \Delta u_{ii}^2 \rangle$*, green triangle represents* $\langle \Delta u_{ji}^2 \rangle$*, blue inverted triangle represents* $\langle \Delta u_{ij}^2 \rangle$*, and orange circle represents* $\langle \Delta u_{jj}^2 \rangle$*. Red solid line corresponds to Taylor micro-scale,* λ *while black dash line corresponds to* $L_{S,\varepsilon}$

5.3.1 SFs & their exponents of points in free stream

The second order SFs in *i* and *j* directions of the streamwise and wall-normal velocity component are roughly unchanged between points 1, 4, and 7 (Figure 5.2). For each of these points, the SF for the streamwise component is noted to be of higher magnitude than the wall-normal SF. For separations above the Taylor micro-scale there appears to be a power law scaling as seen by the approximately linear variation on the logarithmic axes. The corresponding logarithmic derivative

which represents the scaling exponent as a function of separation distance is shown in Figure 5.8. The scaling exponent is noted to decrease from a value of 2 at the smallest resolvable scale and appears to reach a constant value < 0.5 at a separation distance ~1 mm. With respect to Reynolds number, the SF exponents appear significantly different at the smallest separation distance with an exponent value close to 3. The difference in exponents with respect to Reynolds number variation is not apparent for separations above the Taylor scale.

.

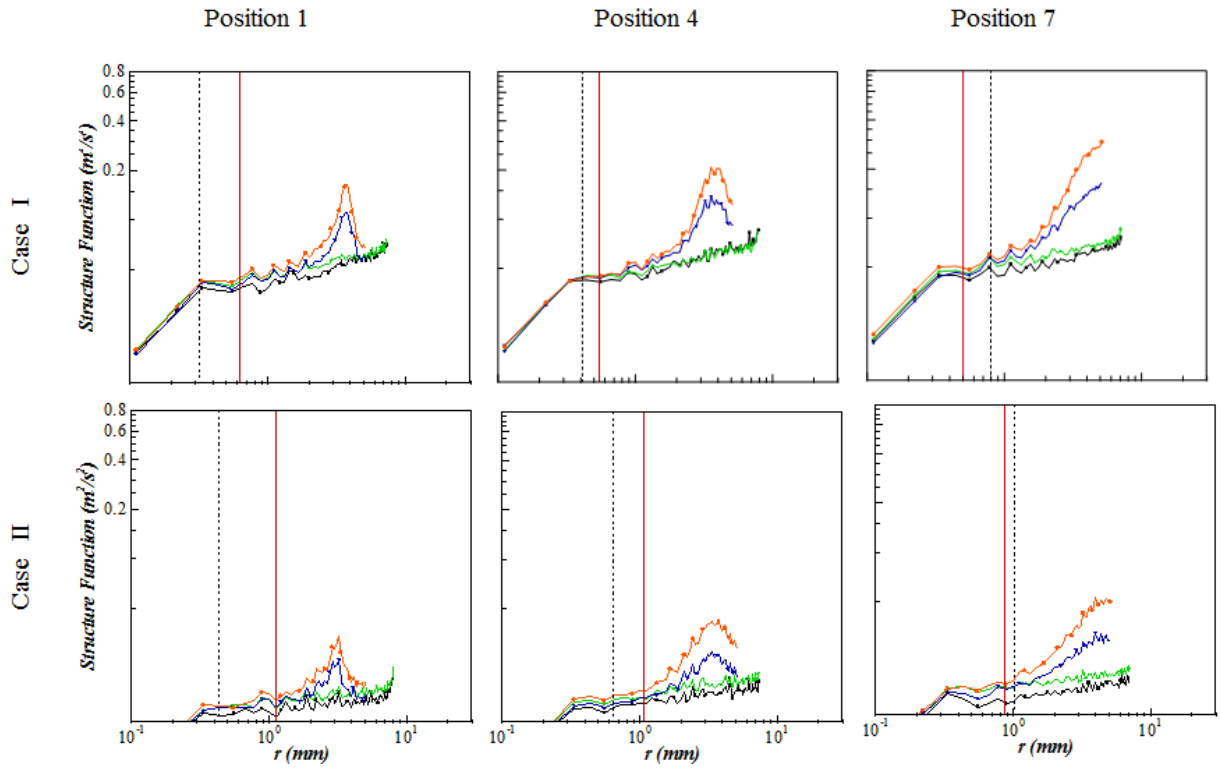

Figure 5.5: Second-order structure function along principal deformation axis. Black square represents $\langle \Delta u^2_{e_1 e_1} \rangle$*, green triangle represents* $\langle \Delta u^2_{e_2 e_1} \rangle$*, blue inverted triangle represents* $\langle \Delta u^2_{e_1 e_2} \rangle$*, and orange circle represents* $\langle \Delta u^2_{e_2 e_2} \rangle$*. Red solid line corresponds to Taylor micro-scale,* λ *while black dash line corresponds to* $L_{S,\varepsilon}$*.*

The SFs in e_1 and e_2 directions of the e_1 and e_2 velocity components are shown in Figure 5.5. Note that the e_2 component SFs has a higher magnitude than the corresponding e_1 component SF. The SFs in the direction toward the shear layer are noted to depart from the typical monotonic behavior. These functions that cross through a region of strongly space dependent shear increase in magnitude through the shear layer followed by a decrease after crossing over the shear region.

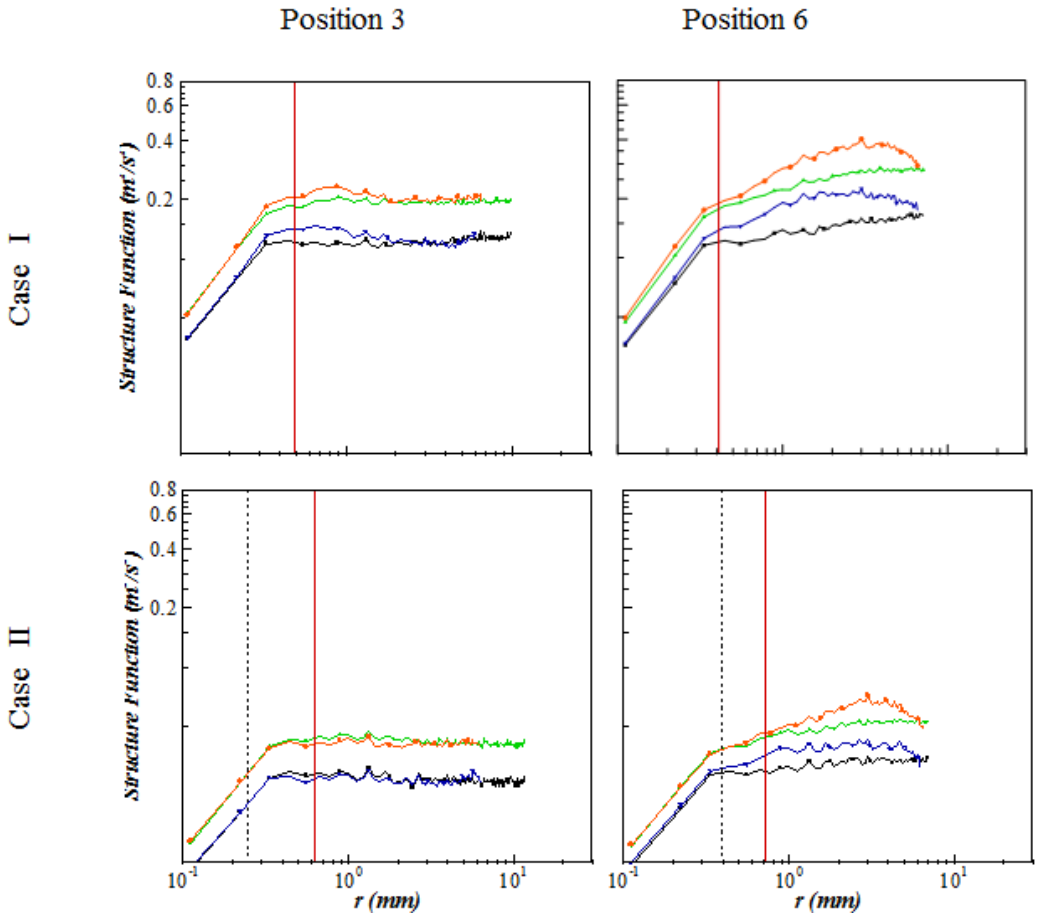

.

Figure 5.6: Second-order structure function along principal deformation axis. Black square represents $\langle \Delta u^2_{e_1 e_1} \rangle$*, green triangle represents* $\langle \Delta u^2_{e_2 e_1} \rangle$*, blue inverted triangle represents* $\langle \Delta u^2_{e_1 e_2} \rangle$*, and orange circle represents* $\langle \Delta u^2_{e_2 e_2} \rangle$*. Red solid line corresponds to Taylor micro-scale,* λ *while black dash line corresponds to* $L_{S,\varepsilon}$*.*

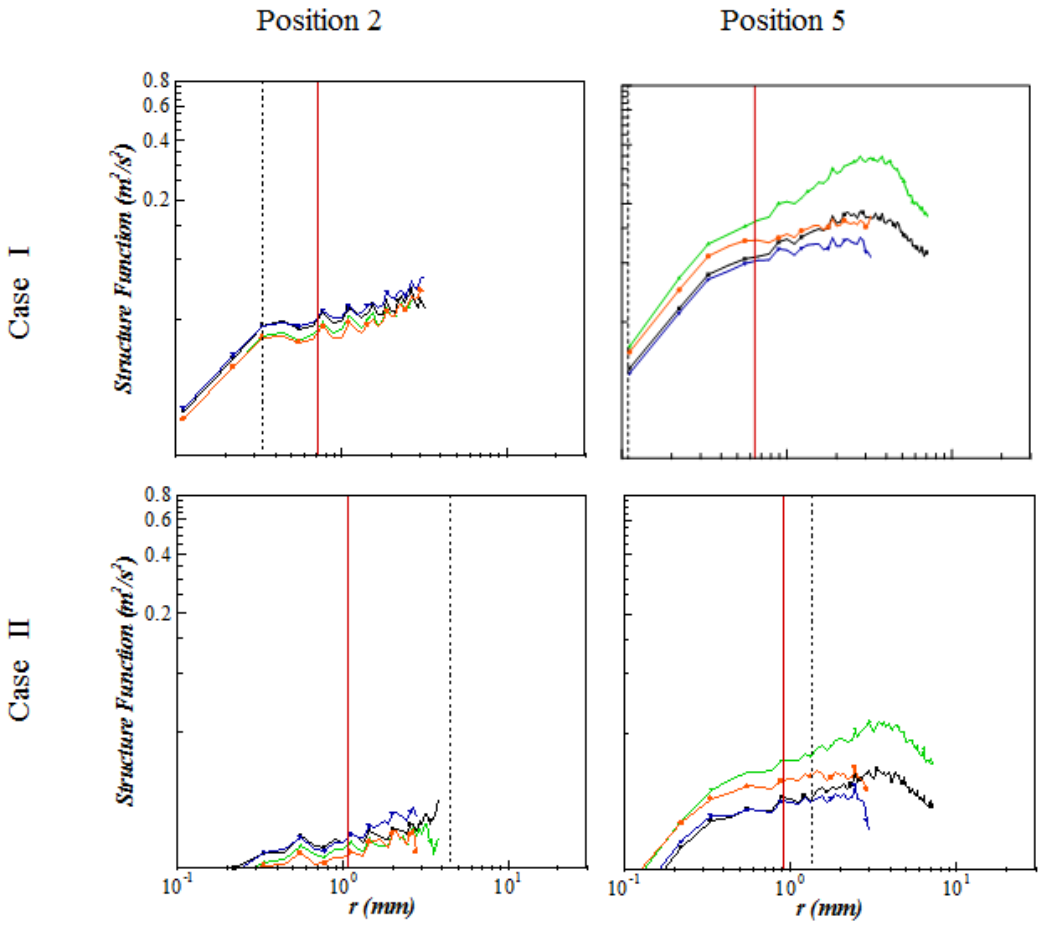

Figure 5.7: Second-order structure function along principal deformation axis. Black square represents $\langle \Delta u^2_{e_1 e_1} \rangle$*, green triangle represents* $\langle \Delta u^2_{e_2 e_1} \rangle$*, blue inverted triangle represents* $\langle \Delta u^2_{e_1 e_2} \rangle$*, and orange circle represents* $\langle \Delta u^2_{e_2 e_2} \rangle$*. Red solid line corresponds to Taylor micro-scale,* λ *while black dash line corresponds to* $L_{c,s}$*.*

This is clearly evident from the local maxima in the SF with the approximate width of this feature proportional to the distance the function takes to traverse through the shear layer in its given direction. The SF in this direction for point number 7 does not traverse long enough to cross over and thus terminates before a local maxima is reached. SFs in the e_1 direction that do not traverse the shear layer are void of this behavior. The exponents for these SFs(Figure 5.11) have a slightly higher magnitude than those in the *i* and *j* direction for separation distances < Taylor micro-scale.

In this regime a noticeable inflection of the exponent curve is seen for exponent values between 0.5 and 1.0. Reynolds number dependence is consistent with that observed in the *i* and *j* direction SFs.

5.3.2 SFs & their exponents of points in the shear layer

Figure 5.3 shows the SFs in the *i* and *j* directions of the streamwise and wall-normal velocity components for interrogation points 3 and 6 that are located within the intense free shear layer. As with the other interrogation points, the magnitude of the SF increases with increasing Reynolds number. In addition, the magnitude of these SFs is significantly higher than the corresponding SFs at points in the free stream as anticipated from the higher turbulence levels of the shear layer relative to the free stream (Figure 4.6 and 4.7). Also the SF of the streamwise velocity component is of higher magnitude than the respective SF of the wall-normal component consistent with the same observation for the interrogation points in the free stream. While the SFs in the streamwise direction are monotonic, those in the wall-normal direction are noted to be non-monotonic. At point 3, the wall-normal direction SF of both the velocity components have a local maxima at the separation distance ~0.35 mm with no observable Re dependence in the location of the maxima. At point 6, however, the corresponding maxima occurs consistently only in the wall-normal component SF at a larger separation distance ~ 1 mm. The streamwise component has a local maxima only observed for the lower Reynolds number case. Based on the non-monotonic trends in SFs and the differences in characteristics of the SF between points 3 and 6, it is clear that local non-homogeneous shear with the imposed spatial variation in turbulence intensities significantly influences the SF characteristics in the small-scale regime. Wall normal SFs at point 3 traverses

the intense shear layer out into the free stream. The distance to cross the shear layer is significantly lesser at point 3 than at point 6 thus correlating with the shift in the local maxima of the wall-normal SFs. SFs in the *i* direction also have significantly different characteristic when compared between points 3 and 6. At point 3, the streamwise SFs appear convex and asymptotes to a constant. However at point 6, the streamwise SFs are monotonically increasing and do not approach a constant.

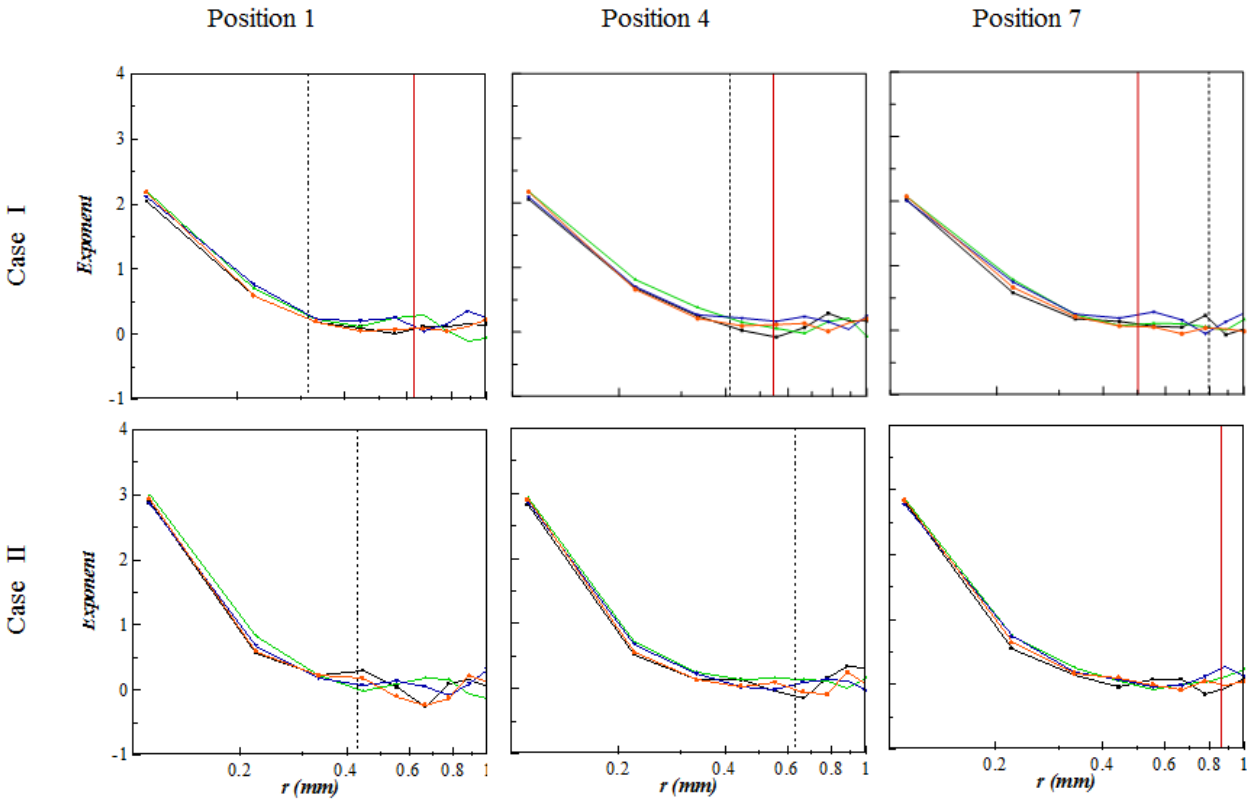

Figure 5.8: Log derivative of second-order structure function in streamwise and wall-normal direction. Black square represents ζ_{ii}, green triangle represents ζ_{ji}, blue inverted triangle represents ζ_{ij}, and orange circle represents ζ_{jj}. Red solid line corresponds to Taylor micro-scale, λ while black dash line corresponds to $L_{S,\varepsilon}$

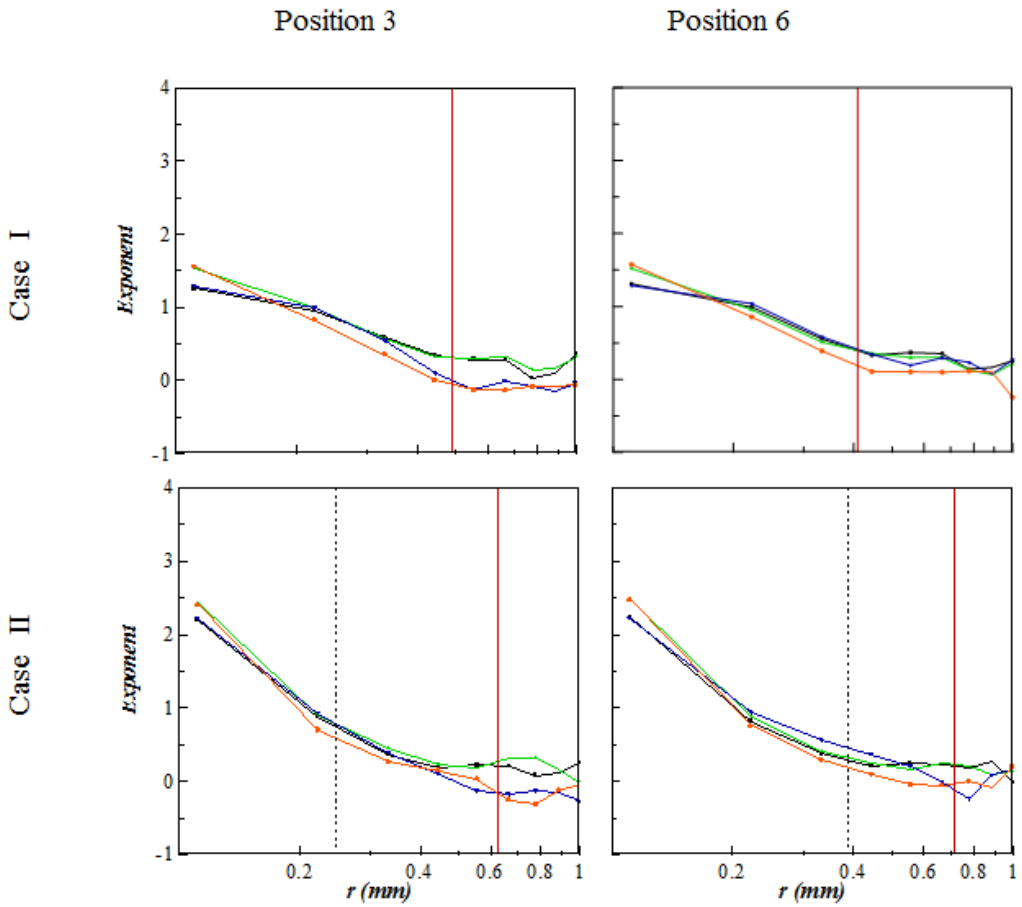

Figure 5.9: Log derivative of second-order structure function in streamwise and wall-normal direction. Black square represents ζ_{ii}, green triangle represents ζ_{ji}, blue inverted triangle represents ζ_{ij}, and orange circle represents ζ_{jj}. Red solid line corresponds to Taylor micro-scale, λ while black dash line corresponds to $L_{S,\varepsilon}$

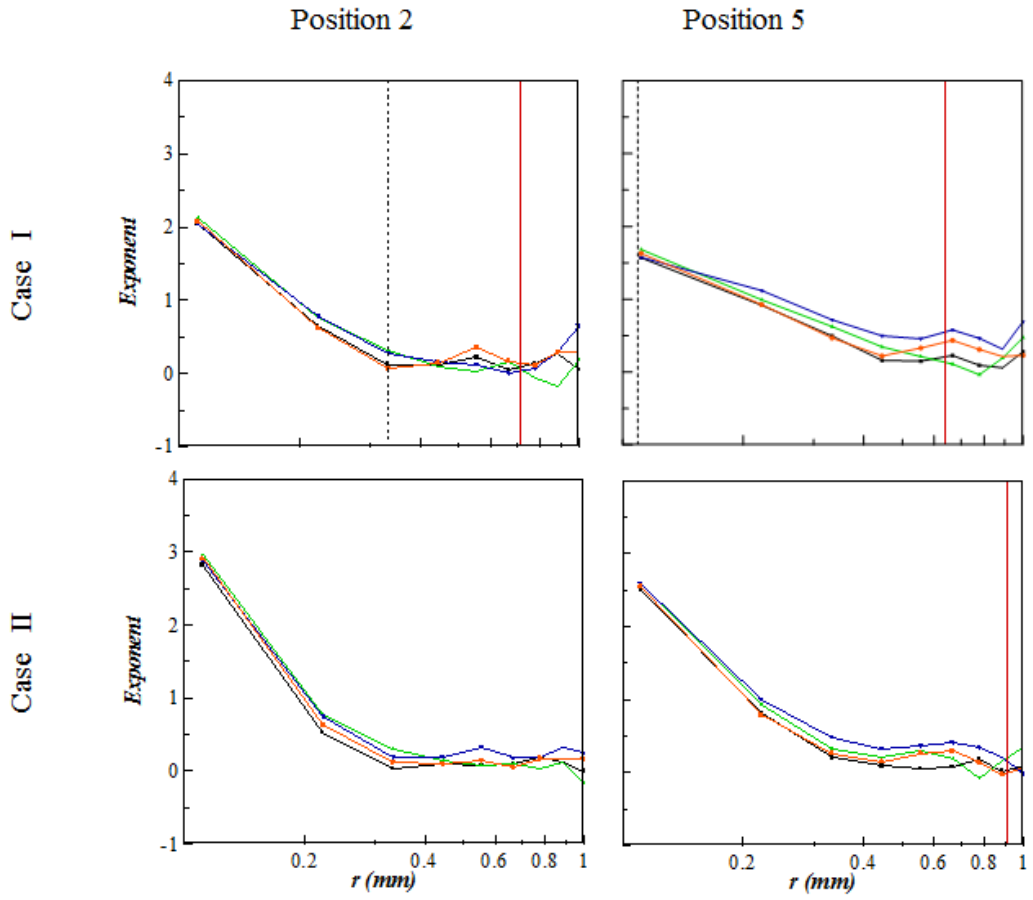

Figure 5.10: Log derivative of second-order structure function in streamwise and wall-normal direction. Black square represents ζ_{ii}, green triangle represents ζ_{ji}, blue inverted triangle represents ζ_{ij}, and orange circle represents ζ_{jj}. Red solid line corresponds to Taylor micro-scale, λ while black dash line corresponds to $L_{S,\varepsilon}$

The scaling exponents of the SFs at points 3 and 6 in *i* and *j* direction are shown in Figure 5.9. When compared with the scaling of SFs located in the free stream, the exponents at the smallest resolvable separation distances are significantly lower. The exponent for the highest Re case begins around a value of 1.5, roughly 0.5 lower than the exponents for the highest Re case in the free stream (position 1, 4, or 7). When compared between corresponding velocity components, at the smallest separation distance the exponent for the streamwise velocity component SFs is

significantly lower than that of the wall-normal velocity component. This significant difference between velocity components switches to a significant difference between SF directions with increasing separation distance (particularly prominent at point 3). The exponent for the streamwise direction SF for both velocity components approaches a positive constant for separation distances ~ 0.5 mm. However, SF exponents for those in the wall-normal direction approach a constant lesser than that of the streamwise direction SF exponents. At point 3 this value is negative. A comparison of exponents of SFs between point 3 and any point in the free stream shows that the exponent for the streamwise direction SF at point 3 is higher than when the wall normal direction SF is decreased. This separation in exponents in the presence of strong shear is slightly diminished at point 6. The stark difference in characteristics between the SF exponent at point 3 and those in the free stream are significantly diminished at point 6 particularly at separation distances around 0.5 mm. Here the significant difference in exponent values between streamwise direction and wall-normal direction at point 3 is no longer as significant.

The SFs in the e_1 and e_2 directions for the points in the shear layer are shown in Figure 5.6. As noted for the SFs in the free stream, the e_2 component SFs has a higher magnitude than the corresponding e_1 component SFs. The SFs in the e_2 direction are clearly non-monotonic with a peak corresponding to the relatively shorter distance to cross the shear layer in this direction. The function in the e_1 direction appears relatively less non-monotonic. The e_1 direction functions at point 3 appear to saturate rapidly while that at point 6 have a nearly power law variation.

The exponents of the SFs in e_1 and e_2 direction are shown in Figure 5.12. At the smallest resolvable scale the exponent for the e_2 component SF is significantly smaller than the e_1 component SF. With increasing scale size, the exponent shows the same behavior as that with the corresponding SFs in the *i* and *j* directions. However the switch to significant difference with respect to direction is not

achieved as prominently. The inflection of these curves occurs between for exponent values between 0 and 0.5.

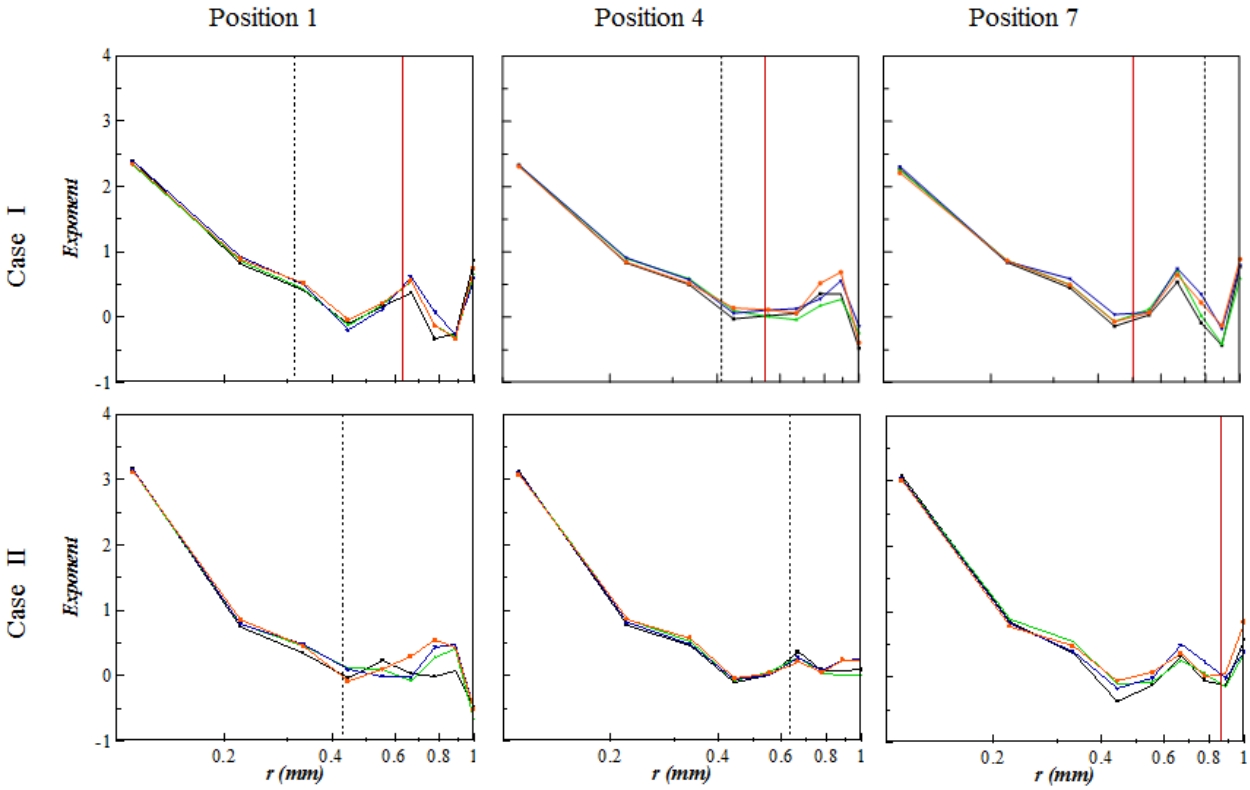

Figure 5.11: Log derivative of second-order structure function in streamwise and wall-normal direction. Black square represents $\zeta_{e_1e_1}$, green triangle represents $\zeta_{e_2e_1}$, blue inverted triangle represents $\zeta_{e_1e_2}$, and orange circle represents $\zeta_{e_2e_2}$. Red solid line corresponds to Taylor micro-scale, λ while black dash line corresponds to $L_{S,\varepsilon}$

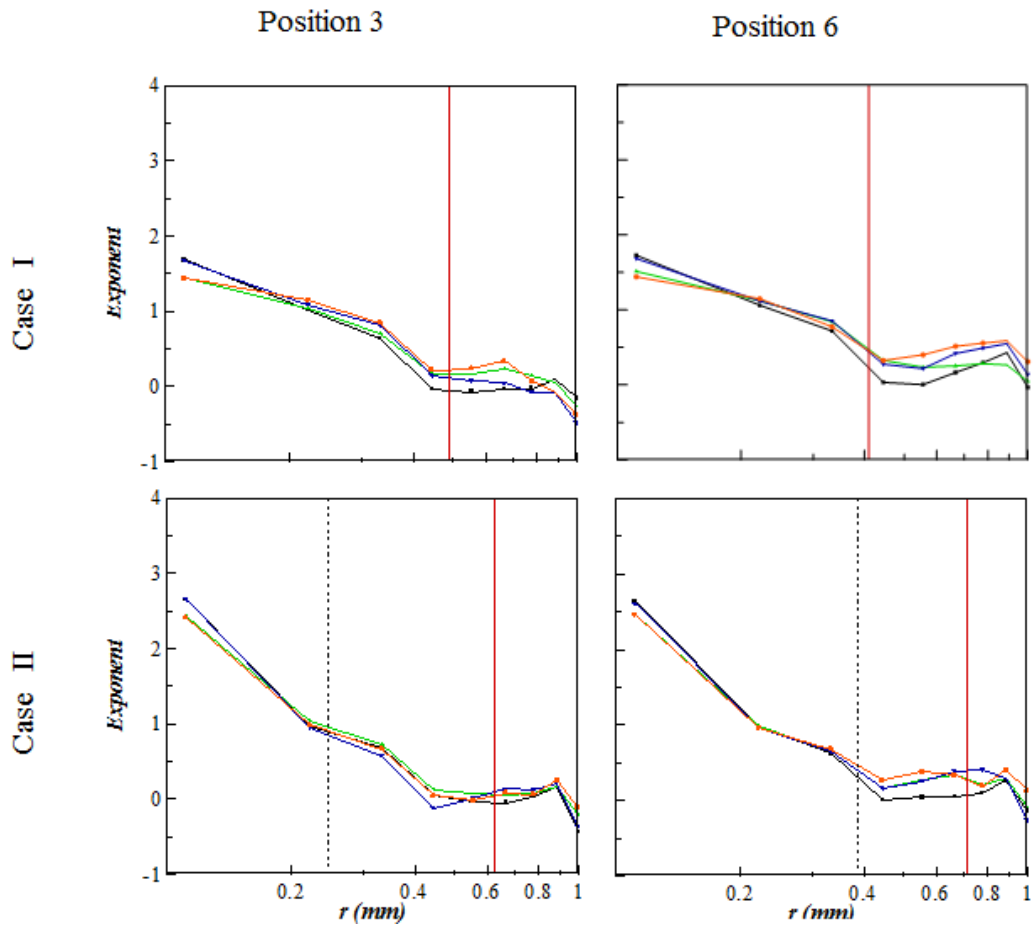

Figure 5.12: Log derivative of second-order structure function in streamwise and wall-normal direction. Black square represents $\zeta_{e_1e_1}$, green triangle represents $\zeta_{e_2e_1}$, blue inverted triangle represents $\zeta_{e_1e_2}$, and orange circle represents $\zeta_{e_2e_2}$. Red solid line corresponds to Taylor micro-scale, λ while black dash line corresponds to $L_{S,\varepsilon}$

5.3.3 SFs & their exponents of points in the separated vortex

Figure 5.4 shows the *i* and *j* direction SFs of the streamwise and wall-normal velocity components for points 2 and 5 that are located within the separated region of flow downstream of the backward facing step. The SF at point 2 has similar characteristics at the small-scales to the functions in the free stream. However for scales greater than 1mm the functions begin to depart from the behavior

seen in the free stream. The SFs in the wall-normal direction have distinct peaks as they traverse through the strong shear layer. The streamwise SFs do not have peaks but show a concave up profile. The wall-normal SF at point 5 has similar characteristics with the distinct peak corresponding to the shear layer location. The peak is broader, consistent with the broader shear layer. The streamwise SFs do not appear concave up as those for point 2. Comparison of the corresponding SF exponent (Figure 5.10) shows that the small-scale structure at point 2 is similar to that in the free stream. However the SF exponent profile for point 5 shows similarity to the small-scale structure within the shear layer. This is evident from the significantly lower magnitude of the exponent and the characteristically similar profile of the exponent profile at point 5, which is similar to that at point 6.

Figure 5.7 shows the e_1 and e_2 direction SFs at points in the separated vortex region. The SFs at point 2 are all concave up. SF at point 5 has a peak corresponding to the traversing of the shear layer. Again, exponent behavior of these SFs (Figure 5.10) confirms stronger shear influences at point 5.

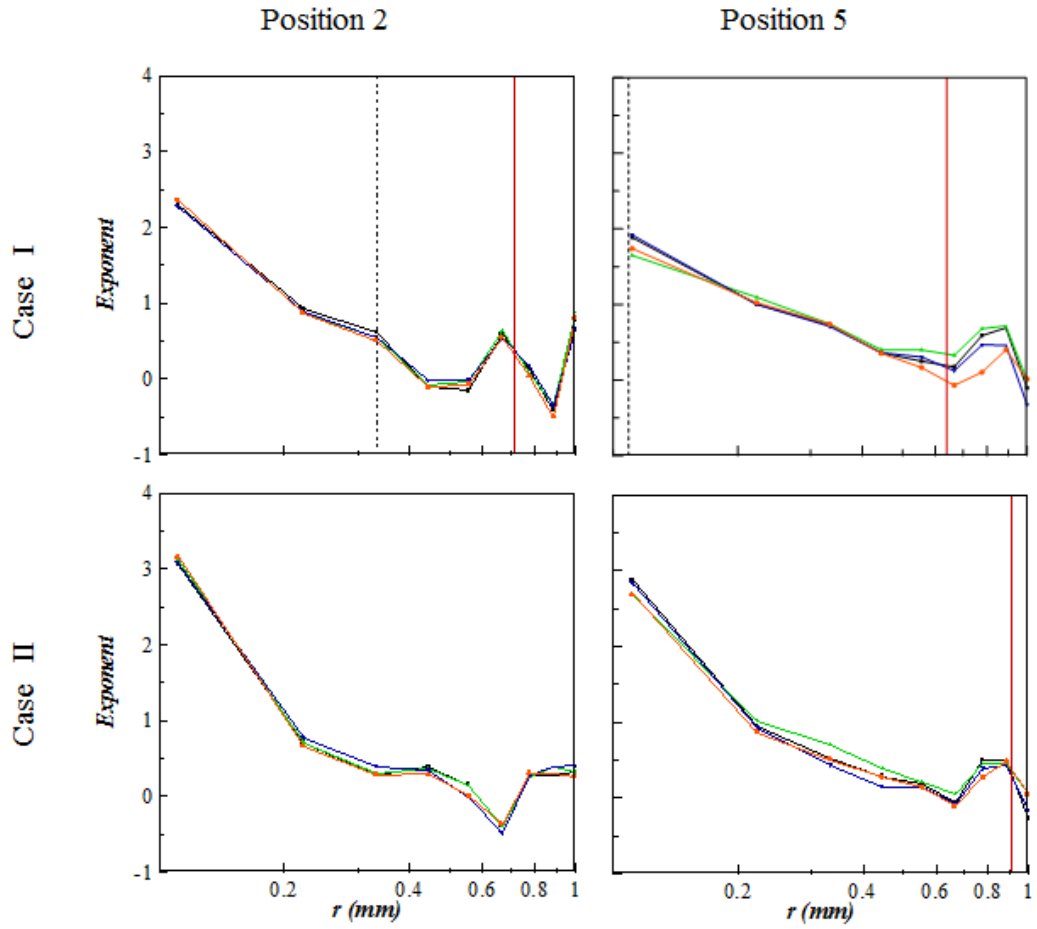

Figure 5.13: Log derivative of second-order structure function in streamwise and wall-normal direction. Black square represents $\zeta_{e_1e_1}$, green triangle represents $\zeta_{e_2e_1}$, blue inverted triangle represents $\zeta_{e_1e_2}$, and orange circle represents $\zeta_{e_2e_2}$. Red solid line corresponds to Taylor micro-scale, λ while black dash line corresponds to $L_{S,\varepsilon}$

5.4 Second order structure functions in 360° directions

Second order structure functions in r and θ directions are shown respectively in figure 5.14 and figure 5.15. Structure functions were normalized with their initial turbulent kinetic energy, k. Turbulent kinetic energy can be represented as $k = \frac{1}{2}\left(\langle u'(\vec{p})\rangle^2 + \langle v'(\vec{p})\rangle^2\right)$, where u' and v' are the fluctuation velocity in the x and y direction respectively. Principal axis of stretching and

contraction were also plotted at each interrogation position. Contours at individual positions were plotted only in the dissipative regions. Direction of principal axis and magnitude of Taylor micro scale, λ can be found in chapter 4. Contours scales for both r and θ directions are the same. At two interrogation positions located in the strong shear region (position 3 and position 6), it was observed that contours level are not circular, rather their shape is elliptical. Whereas three interrogation positions located in the free stream (position 1, position 4 and position 7), indicates that difference between major and minor axis of contours level decreases, hence shapes tends to be circular. These infer that in the strong shear flow is not isotropic even in the dissipative range, this is mere contrast with Kolmogorov's local isotropy hypothesis(A. Kolmogorov, 1941). In the free stream where magnitude of mean shear is relatively lower, flow is close to homogeneous isotropic turbulence expectations (Khandakar Niaz Morshed, Subhas Karan Venayagamoorthy, et al., 2013). SFs contours are connected in the dissipative region and in non-dissipative regions they are not connected. Smallest ellipse are aligned with principal axes, the deviation from the principal axis of larger ellipses are obvious in presence of strong mean shear. A similar pattern was observed for both r and θ directions. Comparing with contours in r and θ directions, they are orthogonal with each other.

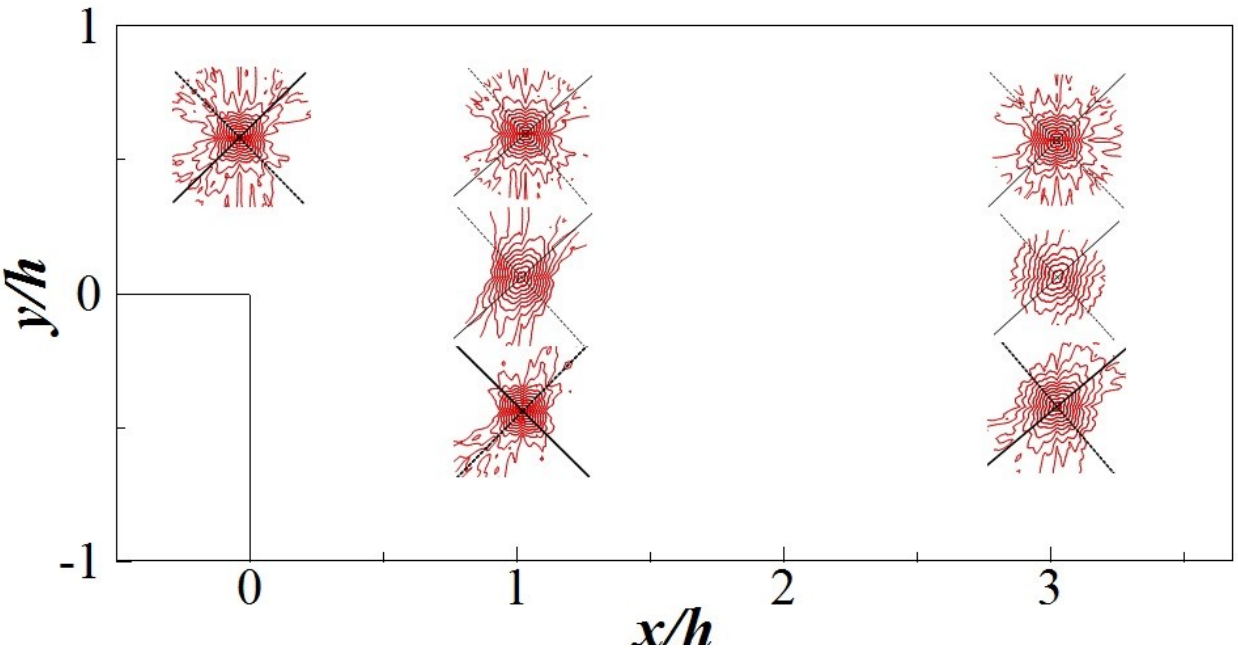

Figure 5.14: Second order velocity structure function of $\langle \Delta u'^2_{r\beta} \rangle(m)$, where β range from 0°to 360° and r indicates parallel direction of β. Solid line indicates principal axis along stretch direction while dashed line indicates principal axis contraction direction.

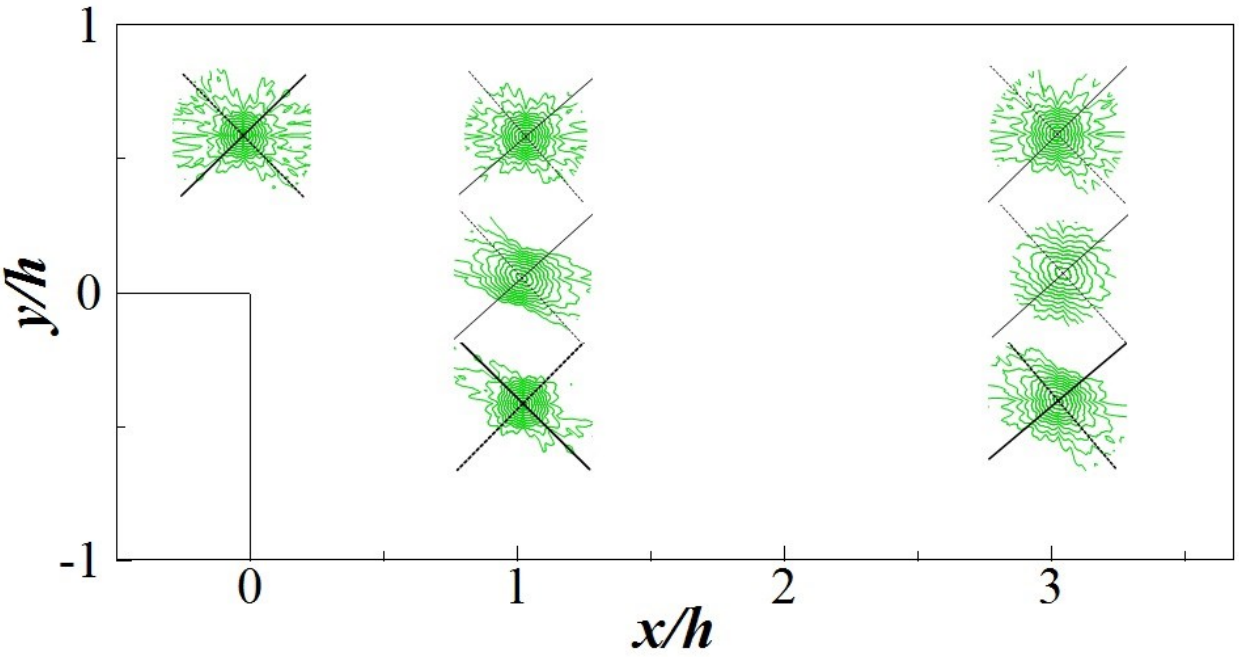

Figure 5.15: Second order velocity structure function of $\langle \Delta u'^2_{\theta\beta} \rangle(m)$, where β range from 0°to 360° and θ indicates perpendicular direction of β. Solid line indicates principal axis along stretch direction while dashed line indicates principal axis contraction direction

5.5 Two point correlation functions in 360° directions

Two point correlation functions in r and θ directions are plotted in figure 5.16 and figure 5.17 respectively. Correlation functions were normalized with their individual coefficient, c. Coefficient can be represented as $\frac{\langle u'(\vec{p}).u'(\vec{p}+m\hat{e}_\beta)\rangle}{\langle u'^2(\vec{p})\rangle^{1/2}.\langle u'^2(\vec{p}+m\hat{e}_\beta)\rangle^{1/2}}$. Contours of the two point correlation functions were also plotted only in the dissipative region. Solid line indicates the stretch direction while dashed line indicates contraction directions. Contours of two point correlation functions are connected in the dissipative regions and not connected in the non-dissipative regions. In the free stream regions (position 1, position 4 and position 7) contours looks like circular, with very subtle difference between major and minor axis. Elliptical contour shapes were observed at position 3 and position 6, these positions experiences strong mean shear. Smallest ellipse are aligned with principal axis for all locations, this alignment differ in presence of strong shear. While comparing the contours of two point correlation at r and θ directions, they are orthogonal to each other.

An additional position, position 8 was considered closer to the backward step. Position 8 is located in between the backward step and position 3. y position is same for both position 3 and position 8. Position 8 is $h/2$ distance (x direction) downstream from the tip of backward facing step. Position 8 experiences higher magnitude of shear than position 3. Figure 5.18 shows two point correlation function at 360° directions for position 8 and position 3 in r direction. Likewise previous figures the contours are showing only in the dissipative regions. Contours are elliptical in the for position 8, similar observation with other positions with strong mean shear.

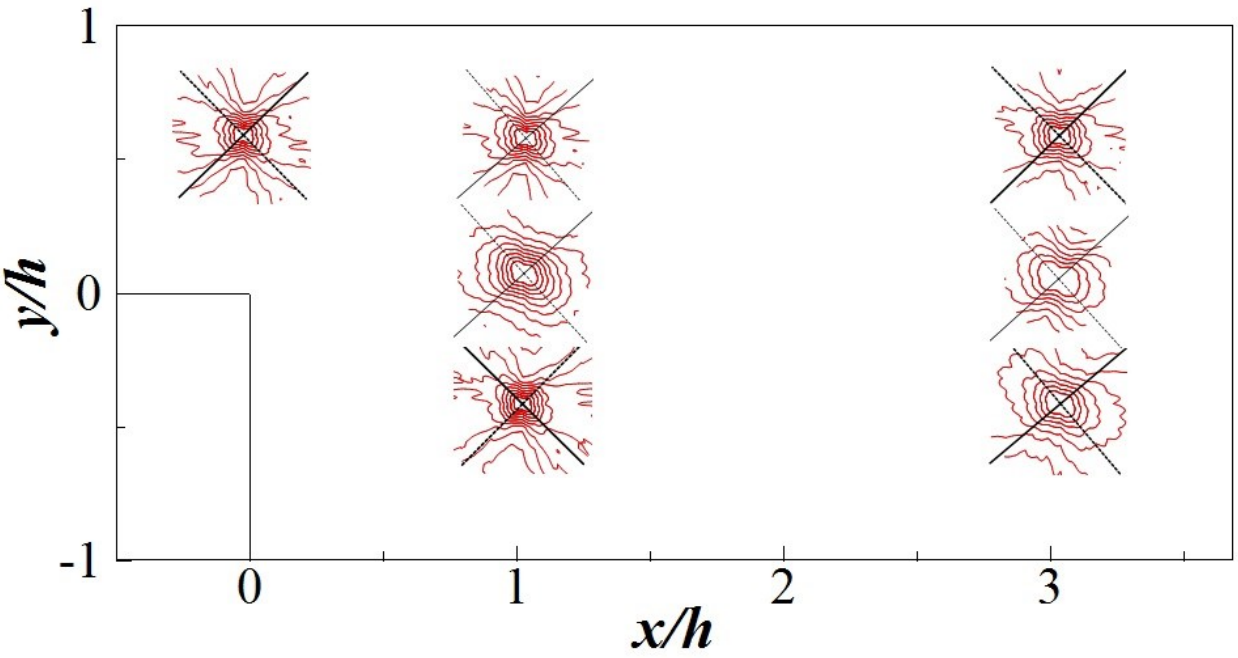

Figure 5.16: Two point correlation function of $\rho_{r\beta}(m)$, where β range from 0°to 360° and r indicates parallel direction of β. Solid line indicates principal axis along stretch direction while dashed line indicates principal axis contraction direction.

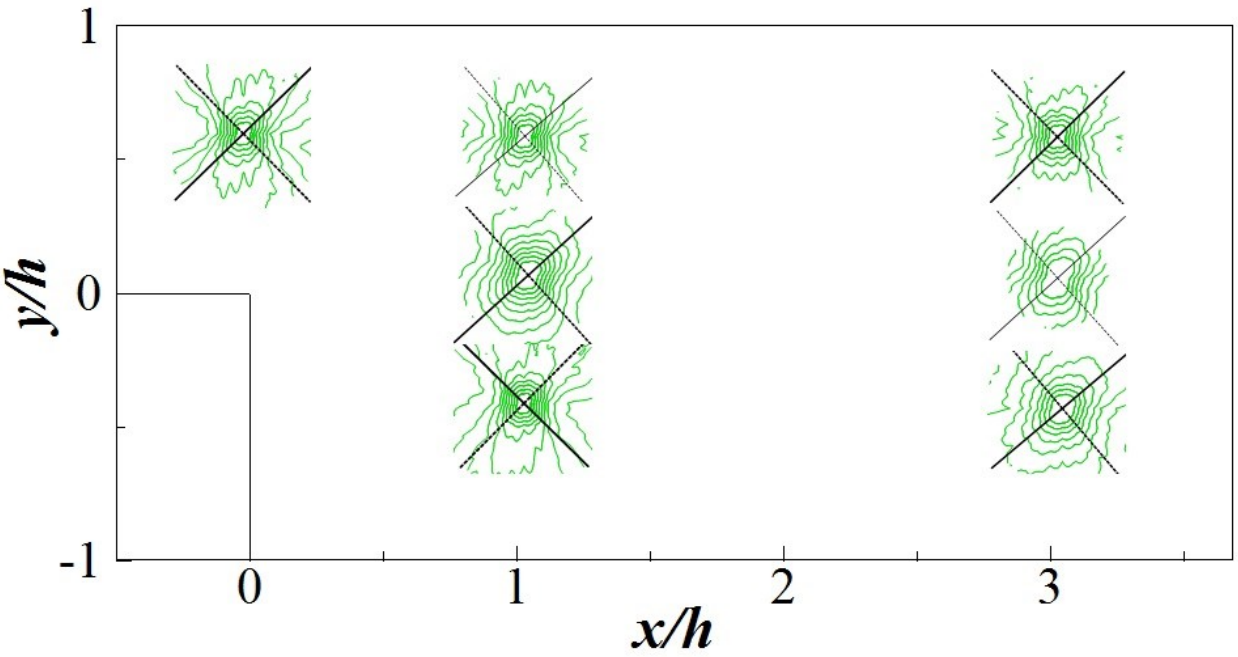

Figure 5.17: Two point correlation function of $\rho_{\theta\beta}(m)$, where β range from 0°to 360° and θ indicates perpendicular direction of β. Solid line indicates principal axis along stretch direction while dashed line indicates principal axis contraction direction.

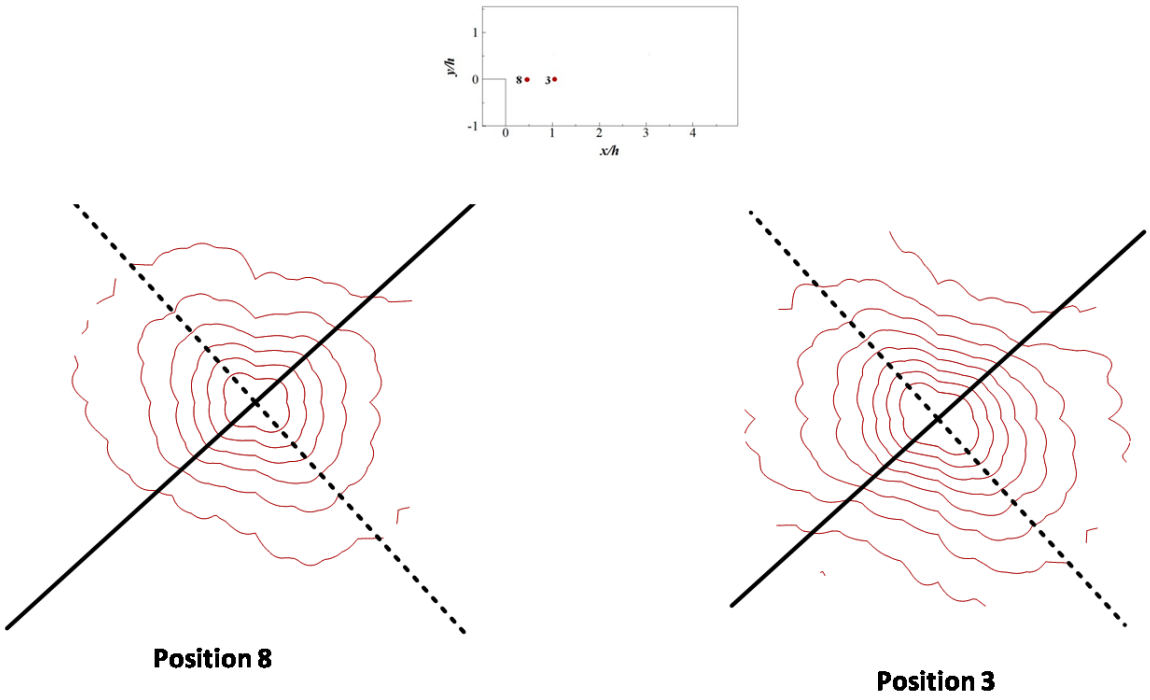

Figure 5.18: Two point correlation function of $\rho_{r\beta}$ (m), where β range from 0°to 360° and r indicates parallel direction of β for position 8 and position 3. Solid line indicates principal axis along stretch direction while dashed line indicates principal axis contraction direction.

5.6 Summary

Normalized probability density functions of velocity components were observed. PDFs are normally distributed for both Reynolds number cases. A subtle difference was observed in PDFs in relation to the skewness in the tails. Second order structure functions and their exponents were calculated in four different directions. From SFs it was observed that at dissipative regions they remain unchanged at low shear, but with increase of shear the changes can be noticed. Streamwise SFs show higher magnitude compared to SFs in wall normal directions. Exponents of second order SFs saturated in the non-dissipative region in presence of strong mean shear. Second order

structure functions in 360° directions reveal that in dissipative region SFs contours are influenced by presence of strong mean shear, similar phenomenon was observed investigating two point correlation functions in 360° directions.

Chapter 6

INTERMITTENCY AND DISSIPATIVE SCALE

6.1 Introduction

Instantaneous velocity gradients are highly intermittent both in spatial and temporal direction for turbulent flows. This hints about highly intermittent nature of instantaneous turbulent kinetic energy dissipation. In this chapter lacunarity analysis was discussed to describe the intermittency nature of dissipation rate signal. Probability density functions of dissipative scale, $Q(\eta/\eta_0)$ was calculated to understand the anisotropic behavior in presence of strong mean shear. The backward facing step flow is an anisotropic turbulent flow with a strong free shear region presumably devoid of the peculiar characteristics of coherent structures found in the near wall channel flow turbulence. A family of universal forms for $Q(\eta/\eta_0)$ was proposed in this chapter that can be parameterized by a local mean shear-dissipation Reynolds number defined as $\langle\varepsilon\rangle/(S^2\nu)$. Also, physical reasoning to support this argument was described. In this chapter analysis was performed only for higher Reynolds number case i.e. Case I. Position 1 was omitted from consideration as position 4 and position 7 both represent free stream location.

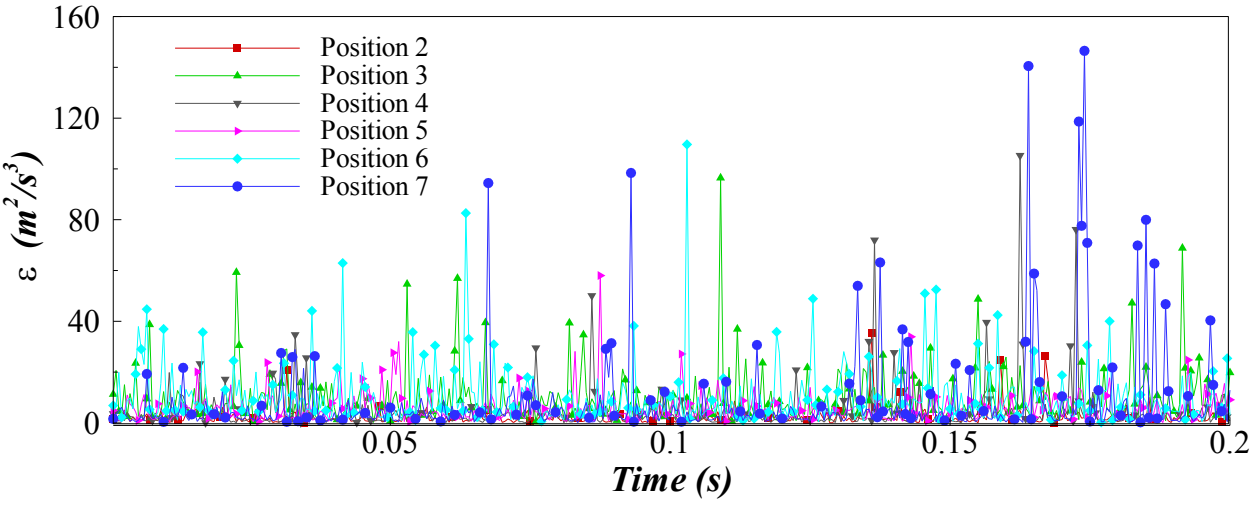

Figure 6.1: Instantaneous turbulent kinetic energy dissipation rate, ε over time at higher Reynolds number case (Case I) for six interrogation positions.

6.2 Intermittency

Lacunarity of the instantaneous dissipation rate signals at the six interrogation points was calculated. Instantaneous ε was calculated using the two-dimensional surrogate approach described in Ref. (Tanaka & Eaton, 2007) as $\varepsilon = \langle 3\nu(s_{11}^2 + s_{11}^2) = 12\nu s_{12}^2 \rangle$, with the isotropic assumptions $\langle s_{13}^2 \rangle = \langle s_{23}^2 \rangle = \langle s_{12}^2 \rangle$ and $\langle s_{33}^2 \rangle = 0.5(\langle s_{11}^2 \rangle + \langle s_{22}^2 \rangle)$. Figure 6.1 shows Instantaneous turbulent kinetic energy dissipation rate, ε for case one at six interrogation positions. From the plots assumptions can be made about the intermittency nature of the dissipation signal. Lacunarity is a fractal measure that characterizes the temporal homogeneity in a multi-fractal signal. It is particularly sensitive to the pattern of intermittent signal bursts occurring at varying time scales, see Refs. (L. P. Dasi, Schuerg, & Webster, 2007; Plotnick et al., 1996). First, the raw dissipation signal is converted into a binary signal via a pre-set threshold. Given a window size

(time scale) λ, the mass signal is obtained as the integral of the binary signal within the window. As the window slides across the entire time-series, the mass signal fluctuates. Lacunarity (λ) is then evaluated using Equation 3.4. Physically, $\Lambda(\lambda)$ reflects the level of inhomogeneity and intermittency in the signal. Figure 6.2 shows the lacunarity of ε for three different thresholds namely $\langle\varepsilon\rangle$, $\langle\varepsilon\rangle + \sigma$ and $\langle\varepsilon\rangle + 2\sigma$ for each of the six locations, where σ is the standard deviation of the fluctuating dissipative scale ε. The lacunarity functions have been shifted up by one decade up for $\langle\varepsilon\rangle + \sigma$ and two decades up for$\langle\varepsilon\rangle + 2\sigma$. The graphs show that the dissipation rate lacunarity for position 3 and position 6 is consistently lower than at other locations that have lower local mean shear. Lower lacunarity implies that the mass signal fluctuates less relative to its mean. This translates to smaller but more frequent bursts in the dissipation rate signal. This is in stark contrast with the large but not so frequent bursts measured at the low mean shear locations. Notice how this is true at all time scales, λ. The above fractal analysis shows a measurable shift in the geometric properties of the dissipation rate signal with increasing shear. Gaps between bursts are smaller with increasing shear and the bursts are not so large relative to the mean (although the average dissipation rate is higher). Strikingly, these are the same conclusions from the dissipation statistics analyzed within the strong shear dominated near wall region of pipe flow DNS study(P. E. Hamlington et al., 2012).

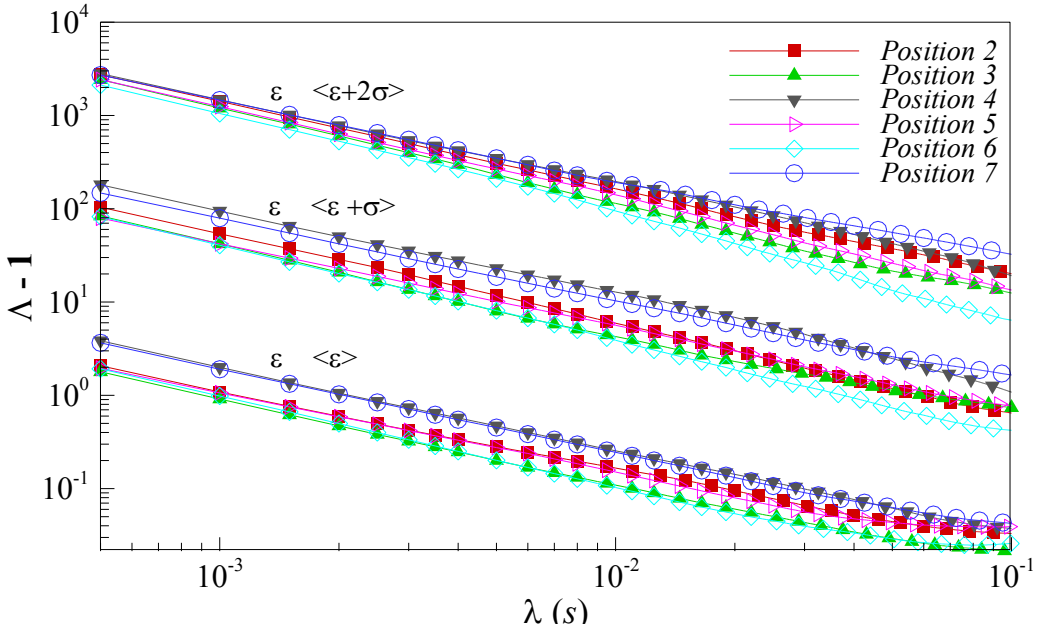

Figure 6.2: Lacunarity of the instantaneous dissipation rate signal measured at each of the six positions downstream of the backward step for three threshold levels. The data corresponding to thresholds of 1 and 2 standard deviations above the mean have been shifted up by 1 and 2 decades, respectively.

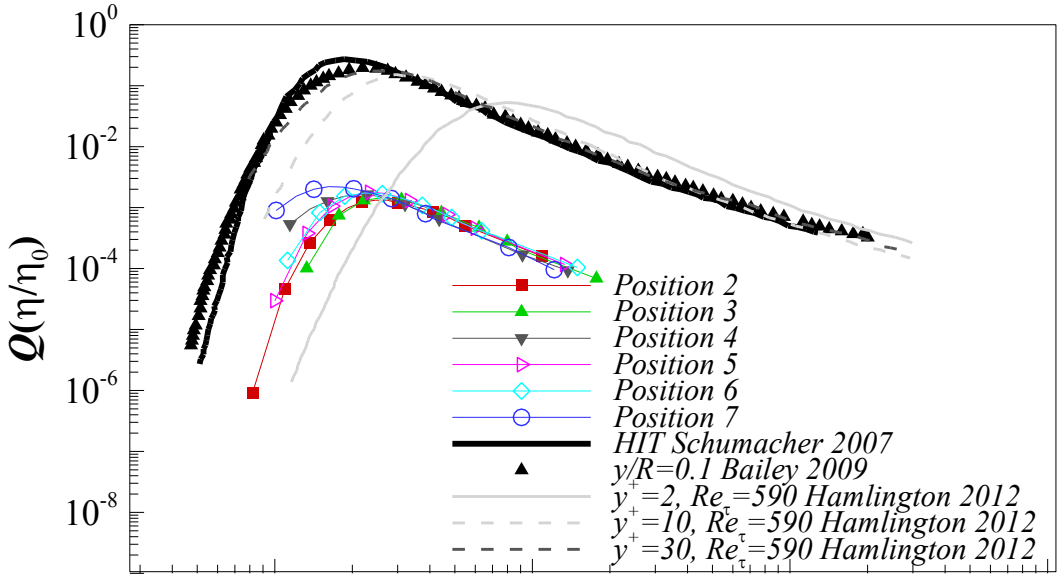

Figure 6.3: Local dissipation scale PDF $Q(\eta/\eta_0)$ measured at each of the six positions downstream of the backward step Data points have been shifted down by 2 decades to aid comparison with previously reported $Q(\eta/\eta_0)$ in HIT, (Schumacher, 2007) and wall bounded flows. (Bailey, Hultmark, Schumacher, Yakhot, & Smits, 2009; P. E. Hamlington, D. Krasnov, T. Boeck, & J. Schumacher, 2012) $(\eta/\eta_0)_{peak}$ plotted as a function of Re_S for each of the six positions downstream of the backward step

6.3 Dissipative scale PDFs

Probability density functions of the local dissipation scale, $Q(\eta)$ was calculated for each of the six interrogation points. The approach is identical to that described in Refs. (Bailey et al., 2009; P. E. Hamlington et al., 2012; Q. Zhou & Xia, 2010) was described more details in chapter 3. Figure 7.3 shows $Q(\eta/\eta_0)$ for the six locations along with previously published results of Refs.(Bailey et al., 2009; P. E. Hamlington et al., 2012; Schumacher, 2007). From the figure, it is clear that the peak location for position 3 and position 6 in the intense shear layer significantly shifts to values higher than that for the case of HIT (shown more clearly in Figure 6.4). The location of the peak appears similar to those in Ref. (P. E. Hamlington et al., 2012) for 30 < y+ < 90 at Re_τ = 590. To confirm that these shifts are indeed significant, uncertainty in the PDFs was calculated. Given that the PDF is derived from the histogram of the occurrence of η, and that the measured variable in the above inequality is $\delta_n u$, it is straightforward to propagate the percent error in the instantaneous velocity of the PIV measurements to the uncertainty in the PDF. Our uncertainty of 2.5% in velocity translates to an uncertainty of 2.8% in $\delta_n u$. Given that the inequality is the only qualifying criteria, the uncertainty in the PDF may be achieved by perturbing the upper and lower limits of the inequality. To be conservative, the PDFs by incorporating a 10% variation in the limits was recalculated and found that the resulting PDFs with this additional 10% uncertainty in $\delta_n u$ insignificantly influenced the shape and position of the peak (same histogram bin with maximum counts). The error in η_0 was estimated at 2.5% based on statistical convergence. Thus, the overall error in the normalized peak location is roughly 2.5%.

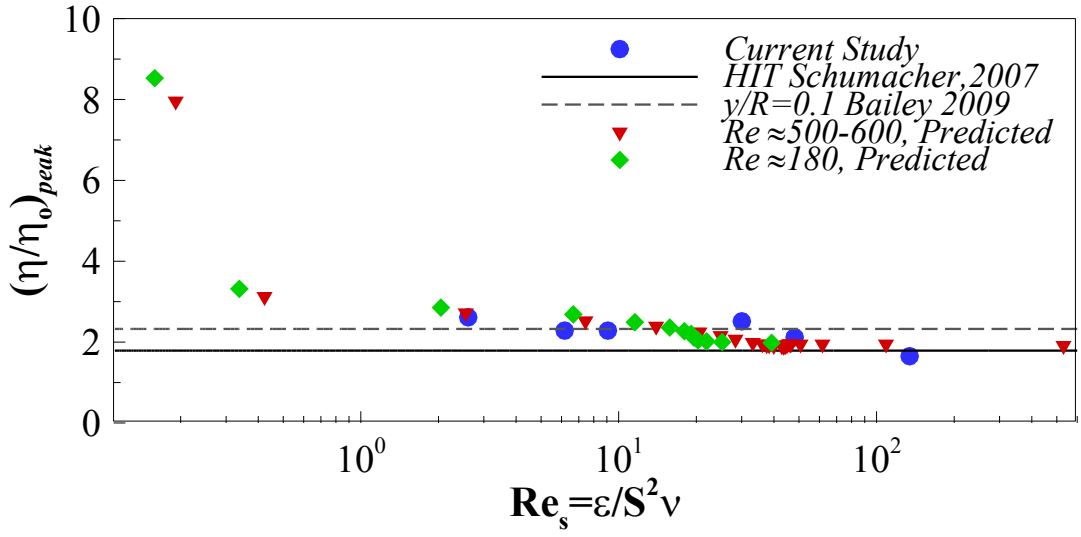

Figure 6.4: $(\eta/\eta_0)_{peak}$ is being compared to the corresponding relationship in channel flows at two different Reynolds numbers. $(\eta/\eta_0)_{peak}$ for HIT (Schumacher, 2007) and pipe flow y/R = 0.1 (Bailey et al., 2009) are depicted as constant levels.6.4 Influence of mean shear

As seen in both Figures 6.2 and 6.3, the intermittent fluctuations of ε and the corresponding distribution of η are clearly dependent on the strong mean shear. While this does not debunk the notion of universality of small-scale turbulent fluctuations, it does indicate the need to refine the description of the small-scale structure by including local anisotropy parameters to further refine the theoretical model of the distribution of η. In this direction, here we provide dimensional arguments to elucidate how strong mean shear can physically alter the small-scale structure. Given that mean shear S regulates turbulence production, it must define a range of production length scales that represent the injection of turbulent kinetic energy or stirring. These production length scales ranging from the large-scale to the smallest scale may be defined as:

$$L_{S,\varepsilon} = (\langle\varepsilon\rangle/S^3)^{1/2} \tag{6.1}$$

$$L_{S,\nu} = (\nu/S)^{1/2} \tag{6.2}$$

While $(\langle\varepsilon\rangle/S^3)^{1/2}$ is a turbulent length scale, which phenomenologically represents the cut-off representing the dominance of mean shear driven energy production as opposed to the transfer via the energy cascade, $(\nu/S)^{1/2}$ is not. Physically, given a stationary mean shear flow, $(\nu/S)^{1/2}$ gauges the size of a ball surrounding a point in the fluid domain whose Reynolds number is one. Thus, it is the dissipative scale, similar to the definition of η, but of the mean flow. Another physical interpretation is that it is the length scale across which the turbulent dissipation rate at that length scale $\sim \nu^3/L_{S,\nu}^4$ is equal to the viscous dissipation rate of the smooth mean flow, $\sim \nu S^2$.

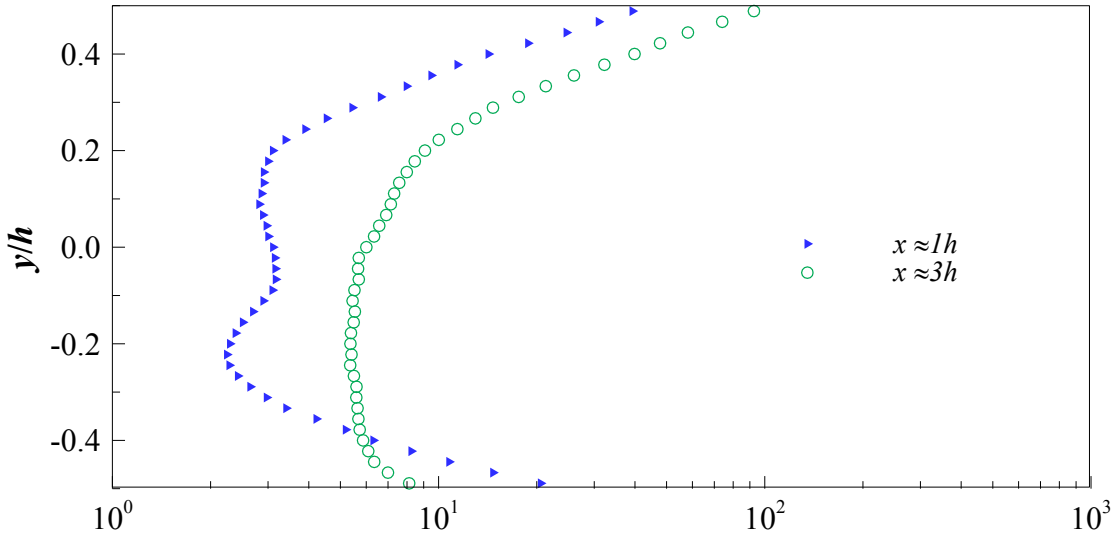

Figure 6.5: Profiles of Re_S along the wall normal direction y/h at two distances downstream of the backward step

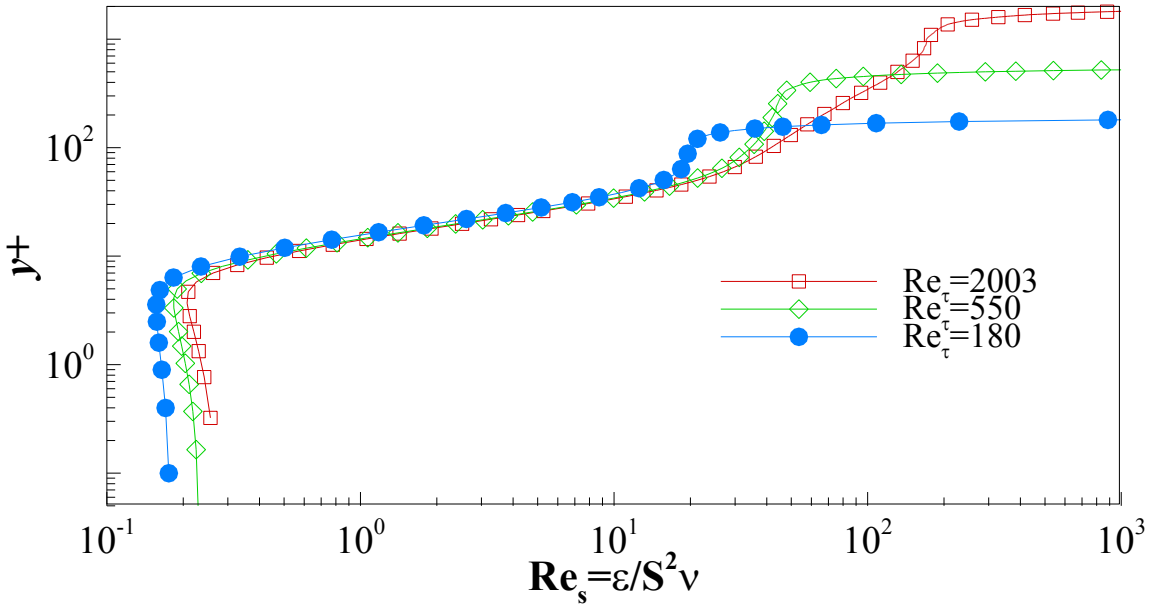

Figure 6.6: Representing Re_S profile along the wall normal direction y+ derived from channel flow DNS simulations (Hoyas & Jiménez, 2008) at three Reynolds numbers.

It is evident from these dimensional constructions that the above shear derived scales tend to infinity as S→0, indicating that production at low shear occurs at the large-scale. It also indicates that as the local shear magnitude increases, both $(\langle\varepsilon\rangle/S^3)^{1/2}$ and $(\nu/S)^{1/2}$ can begin to overlap with the range of the fluctuating η. Notice that the ratio of the squares of $(\langle\varepsilon\rangle/S^3)^{1/2}$ to $(\nu/S)^{1/2}$ defines the mean shear-dissipation Reynolds number Re_S given by,

$$Re_S = \langle\varepsilon\rangle/(S^2\nu) \tag{6.3}$$

which → 0 with increasing magnitude of *S*. It is also easy to see that the ratio of $(\langle\varepsilon\rangle/S^3)^{1/2}$ to the Kolmogorov scale is $Re_S^{3/4}$. Furthermore, Re_S can be either expressed in terms of the turbulence Reynolds number as $Re_S = Re_L(ST_L)^{-2}$, where $T_L = \frac{k}{\varepsilon}$ is the turbulence time scale, or in terms of the Kolmogorov time scale as $Re_S = (S\tau_n)^{-2}$, where τ_n is the Kolmogorov time scale $(\nu/\varepsilon)^{1/2}$. The dimensionless time-scale ratio ST_L thus emerges as being truly independent. Given that the

presence of mean shear adds an independent dimension to the dimensionless formulation of scales; the influence of mean shear may be hypothesized as:

(1) Shear flow turbulence can have the same structure and dynamics as isotropic turbulence provided both Re_L and Re_S are large (i.e., when $ST_L \rightarrow 0$);

(2) For large Re_L but Re_S of O(1) (i.e., $ST_L \gg 0$), the structure of turbulence significantly departs from the isotropic picture;

(3) There exists a family of universal structure of small-scale turbulence defined by the parameter Re_S or more independently by ST_L for very large Re_L.

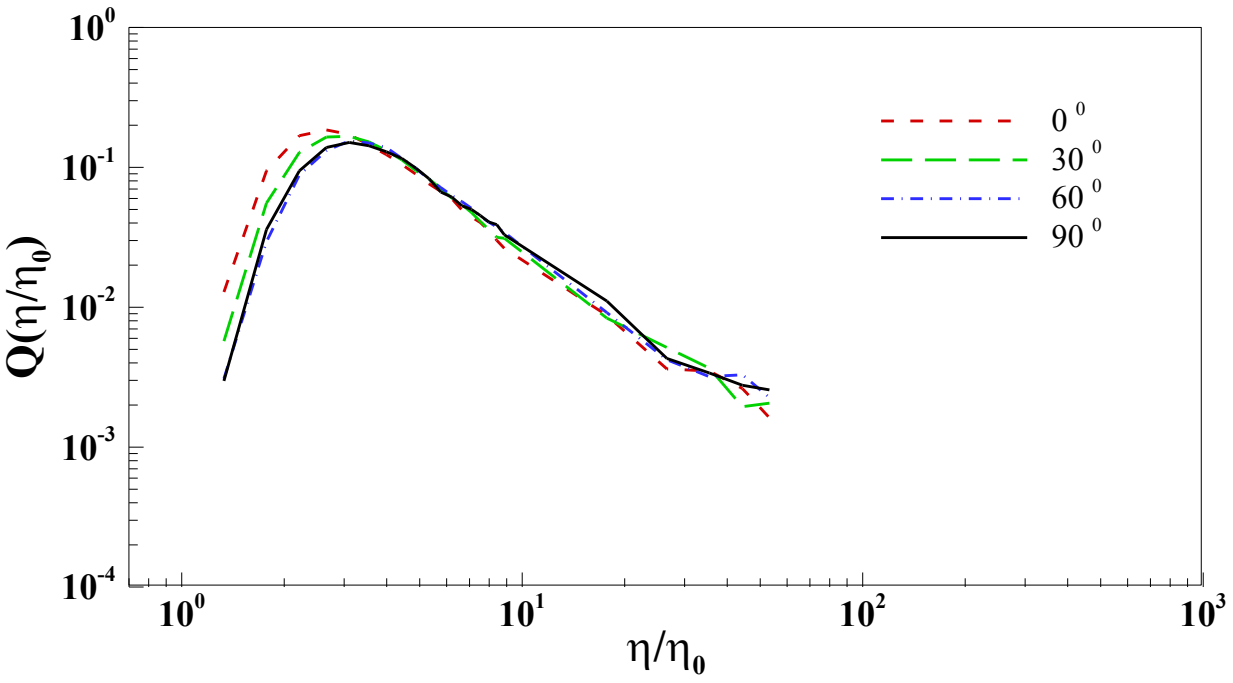

Figure 6.7: Local dissipation scale PDF $Q(\eta/\eta_0)$ measured at downstream of backward facing step at position 3 at various directions (angle ranging from 0° to 90°). Local dissipation scale was calculated from V_r , where r indicates parallel direction to β. β range from 0° to 90° (for this figure only, typically β range from 0° to 360°) . Red dash line represents $Q(\eta/\eta_0)$ at 0°, green long dash line represents $Q(\eta/\eta_0)$ at 30°, blue dash dot line represents$Q(\eta/\eta_0)$ at 60° and black line represents $Q(\eta/\eta_0)$ at 90°.

6.5 Dissipative scale PDFs in 360° directions

Probability density functions of local instantaneous dissipation scale at position 3 are calculated and shown in figure 6.7. Position 3 located in the strong mean shear region. $Q(\eta)$ is normalized with η_0. $Q(\eta/\eta_0)$ distributions are plotted for four different directions (i.e. 0°, 30°, 60° and 90°) for V_r velocity component, where *r* indicates the parallel direction to β. β range from 0° to 90°. Similar kind of distribution pattern was observed at four different directions, with extended right tail. This is comparable with previous study of $Q(\eta/\eta_0)$ (Bailey et al., 2009; Peter E. Hamlington, Dmitry Krasnov, Thomas Boeck, & Jörg Schumacher, 2012; Khandakar Niaz Morshed, Subhas Karan Venayagamoorthy, et al., 2013; Schumacher, 2007; Q. Zhou & Xia, 2010) at different turbulent flows. However, the peak location of $Q(\eta/\eta_0)$shifted toward rightward from 0° to 60° directions. But for 90° direction $Q(\eta/\eta_0)$slightly offset left from 60° direction. Figure 6.8 shows $Q(\eta)$distribution at all directions (angle ranging from 0° to 360°) for position 3. $Q(\eta)$ was normalized with η_0. Figure shows V_r velocity component, where *r* indicates the parallel direction to β. β range from 0° to 360°. Contours of the plots is colored by $Q(\eta)$, with $Log\ \eta_x/\eta_0$ in the *x*-axis, $Log\ \eta_y/\eta_0$ in the *y*-axis and $Log\ Q(\eta/\eta_0)$in the *z*-axis. Distribution of local instantaneous dissipation scale has similar type of pattern observed earlier with extended right tail. If we observe the peak location at varying directions their shape looks like ellipse. This type of behavior can be observed more clearly in figure 6.9, shows the PDFs of $Q(\eta/\eta_0)$ at all seven interrogation positions at all directions (angle ranging from 0° to 360°). Distribution of velocity component is plotted for V_r velocity component. Peak locations of $Q(\eta/\eta_0)$distribution at position 1, 4 and 7 (located in the free stream region) are circular shape, while peak location of $Q(\eta/\eta_0)$distribution at position 3 and 6 (located in the strong mean shear region) are elliptical shape and peak location of

$Q(\eta/\eta_0)$distribution at position 2 and 5 (located in the recirculation region) are almost circular shape. Although, position 5 located in the recirculation zone but this position experience higher magnitude of shear comparing with position 2. Peak location shape stands between circular and elliptical shape for position 5. Comparing with position 3 and position 6, position 3 has larger major and minor axis comparing with position 6. Figure 6.10 shows the $Q(\eta/\eta_0)$ distributions for all seven interrogation positions for V_θ, where θ indicates the perpendicular direction to β. β range from 0° to 360°. Likewise V_r distributions, in the strong mean shear region (position 3 and position 6) the peak shapes of peak locations are elliptical, whereas in the free stream and recirculation region the peak shapes look from circular to almost circular. To understand the influence of mean shear one additional position (i.e. position 8) was interrogated. Position 8, located *h/2* closer to the backward facing step and experience much stronger shear than position 3. *y* locations are similar for both position 3 and position 8. Figure 6.11 shows $Q(\eta/\eta_0)$ distributions for position 3 and position 8 at all directions (angle ranging from 0° to 360°) for V_r velocity component. As predicted, the peak shape of $Q(\eta/\eta_0)$ distributions look elliptical. While comparing with position 3, the major and the minor axis of the ellipse formed by the peak location is bigger than position 8. Similar phenomenon was observed, while comparing $Q(\eta/\eta_0)$ distributions at position 3 and position 6. Position 3 experiences stronger mean shear comparing with position 6. Ellipse formed by the peak locations of position 3 has larger major and minor axis comparing with ellipse formed by the peak locations of position 6.

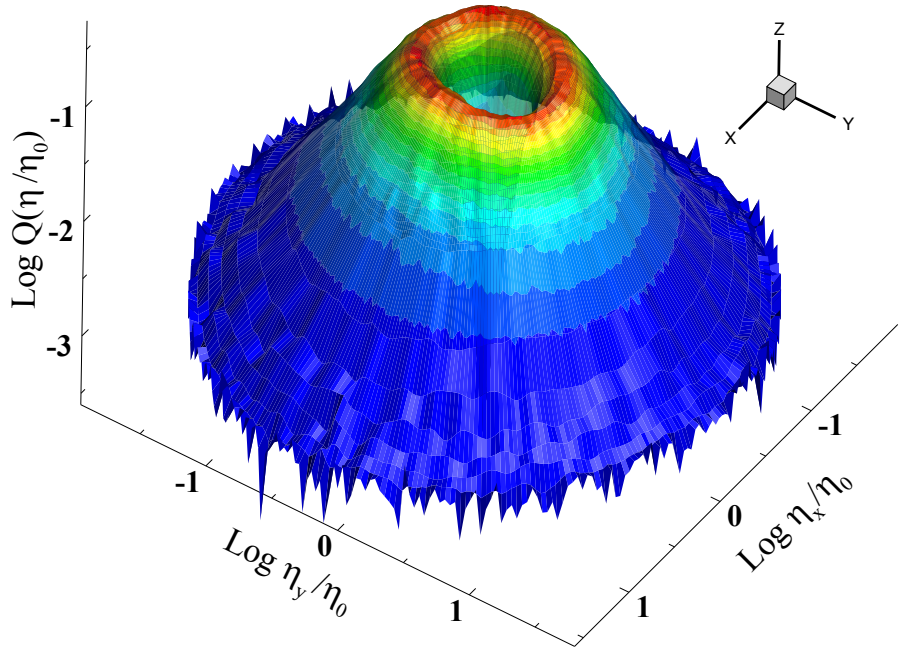

Figure 6.8: Local dissipation scale PDF $Q(\eta/\eta_0)$ measured at downstream of the backward facing step at position 3 at all directions (angle ranging from 0° to 360°). Local dissipation scale was calculated from V_r , where r indicates parallel direction to β. β range from 0° to 360°.

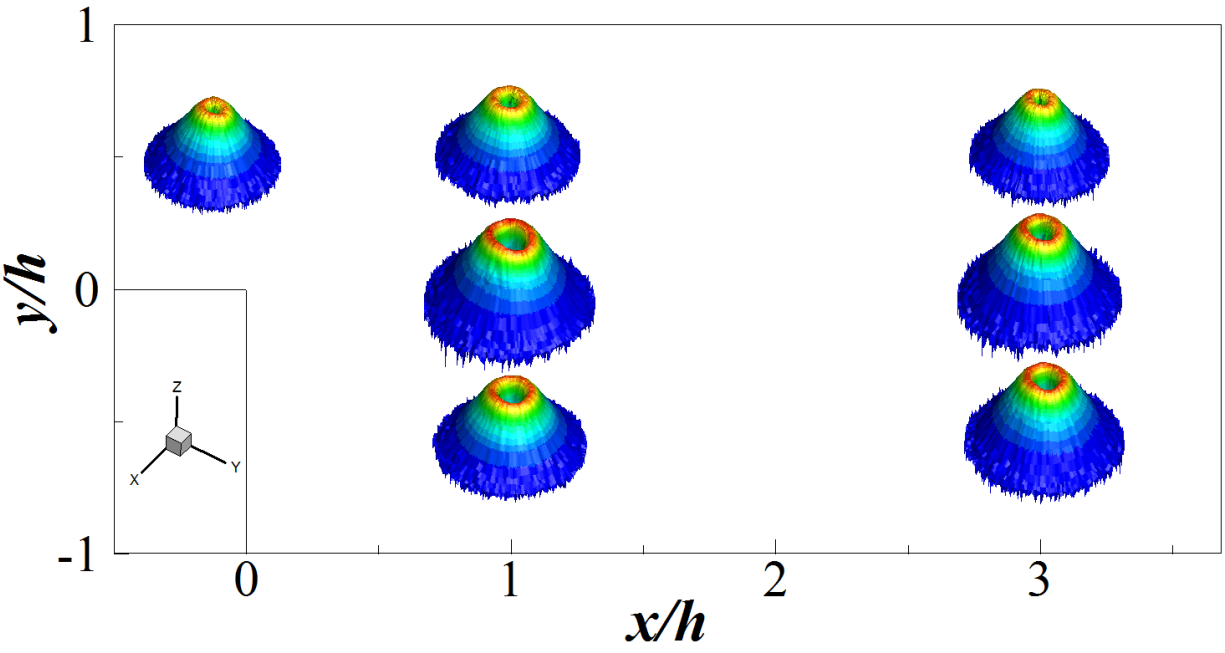

Figure 6.9: Local dissipation scale PDF $Q(\eta/\eta_0)$ measured at downstream of backward facing step at seven positions at all directions (angle ranging from 0° to 360°). Local dissipation scale was calculated from V_r , where r indicates parallel direction to β. β range from 0° to 360°.

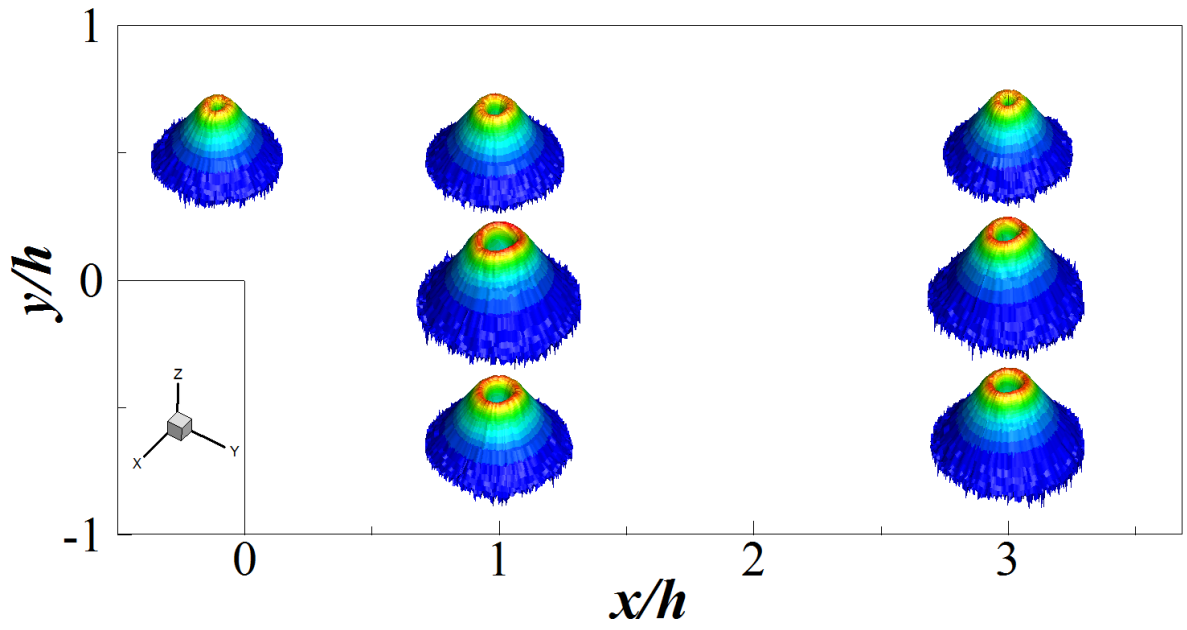

Figure 6.10: Local dissipation scale PDF $Q(\eta/\eta_0)$ measured at downstream of the backward facing step at seven positions at all directions (angle ranging from 0° to 360°). Local dissipation scale was calculated from V_θ , where θ indicates perpendicular direction to β. β range from 0° to 360° .

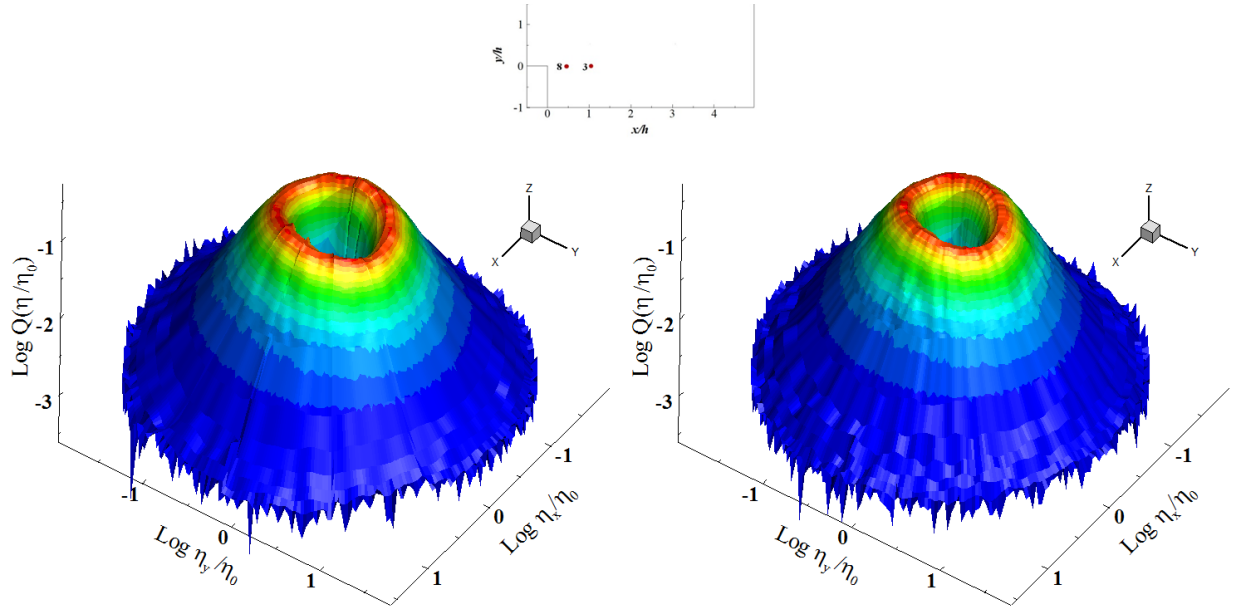

Figure 6.11: Local dissipation scale PDF $Q(\eta/\eta_0)$ measured at downstream of the backward facing step at position 8 and position 3 at all directions (angle ranging from 0° to 360°). Local dissipation scale was calculated from V_r , where r indicates parallel direction to β. β range from 0° to 360° . Position 8 has higher magnitude of shear comparing with position 3.

We measured 2.5% uncertainty in velocity measurement and 2.8% uncertainty in $\delta_\eta u$. 2.5% error was estimated in $\eta_0$calculation based on statistical convergence. These all translate that, roughly there is 2.5% overall uncertainty in each normalized positions. From the $Q(\eta)$ distribution with η_0 normalization, it was obvious that mean shear, *S* has strong influence on distribution of small scale. This may disprove the universality of small-scale turbulent fluctuations. Therefore, a new normalization factor $\eta_{peak}$was introduced. Figure 6.12 shows $Q(\eta)$ distribution at position 3 in all directions for V_r velocity component. In this figure normalization factor $\eta_{peak}$was used instead of η_0. η_{peak} was calculated for individual $Q(\eta)$ at all directions. Previously it was observed at position 3 peak locations form elliptical shape, however with new normalization parameter no elliptical shape was observe. Figure 6.13 and 6.14 shows distribution of dissipation scales $Q(\eta)$ at all seven positions in all directions for V_r and V_θ velocity component respectively, normalized with η_{peak}. From this two figures it can be observe clearly that all the peak locations form circular shape, irrespective of presence of strong mean shear. An addition position (position 8) was taken to examine the influence of stronger shear. Position 8 is located *h/2* closer to the step, therefore experiences stronger mean shear than position 3. Distribution of dissipation scales of position 3 and position 6 are shown in figure 6.15. The peak locations shape look circular for both the PDFs with almost no difference. Therefore it can be propose η_{peak} as normalization parameter for calculating local instantaneous dissipation scales distribution $Q(\eta)$.

Figure 6.16 shows contours of two point correlation functions (in red) for all seven positions in *r* direction. Contours of $Q(\eta)$ was plotted on the top of the two point correlation functions contours shown in black. From the contours of $Q(\eta)$ at position 3 and position 6 it is obvious that major and minor axis of $Q(\eta)$ does not coincide with abscissa and ordinate, neither with principal axes.

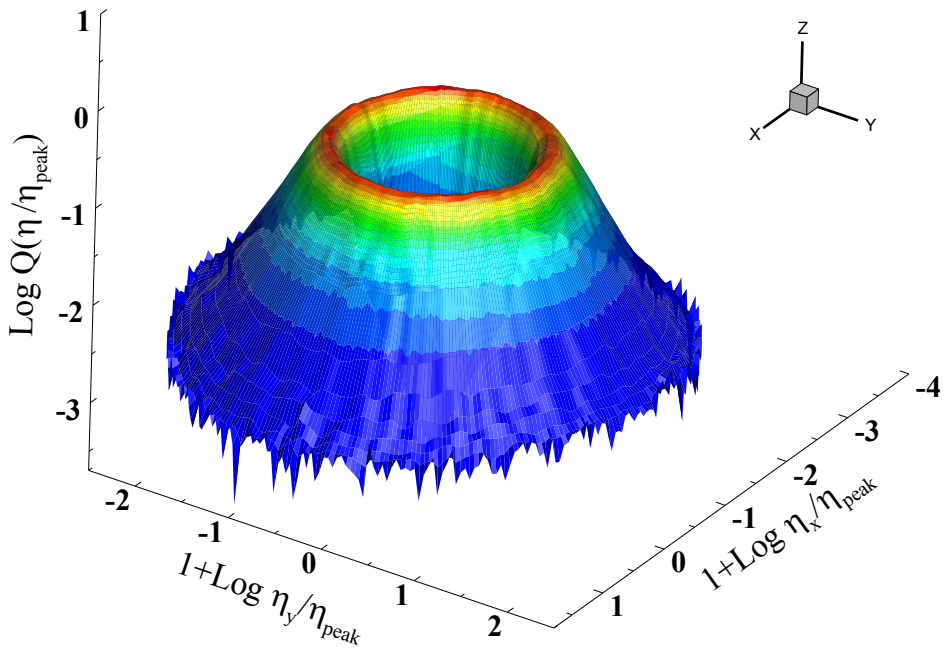

Figure 6.12: Local dissipation scale PDF $Q(\eta/\eta_{peak})$ measured at downstream of the backward facing step at position 3 at all directions (angle ranging from 0° to 360°). Local dissipation scale was calculated from V_r , where r indicates parallel direction.

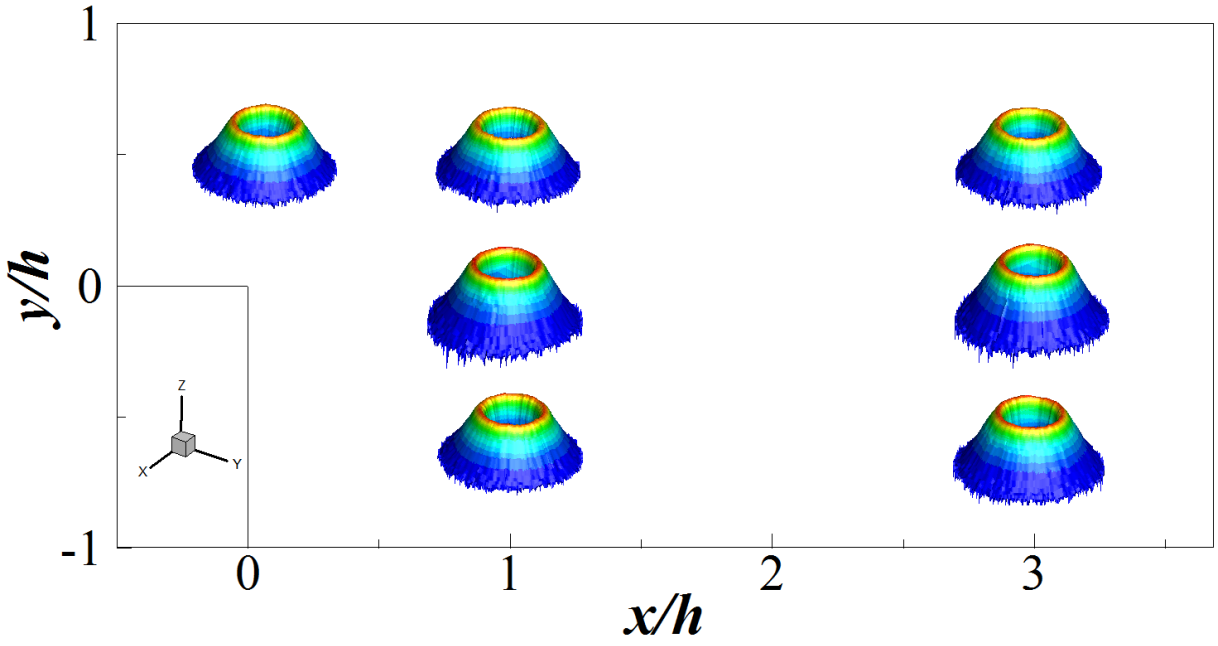

Figure 6.13: Local dissipation scale PDF $Q(\eta/\eta_0)$ measured at downstream of the backward facing step at seven positions at all directions (angle ranging from 0° to 360°). Local dissipation scale was calculated from V_r , where r indicates parallel direction.

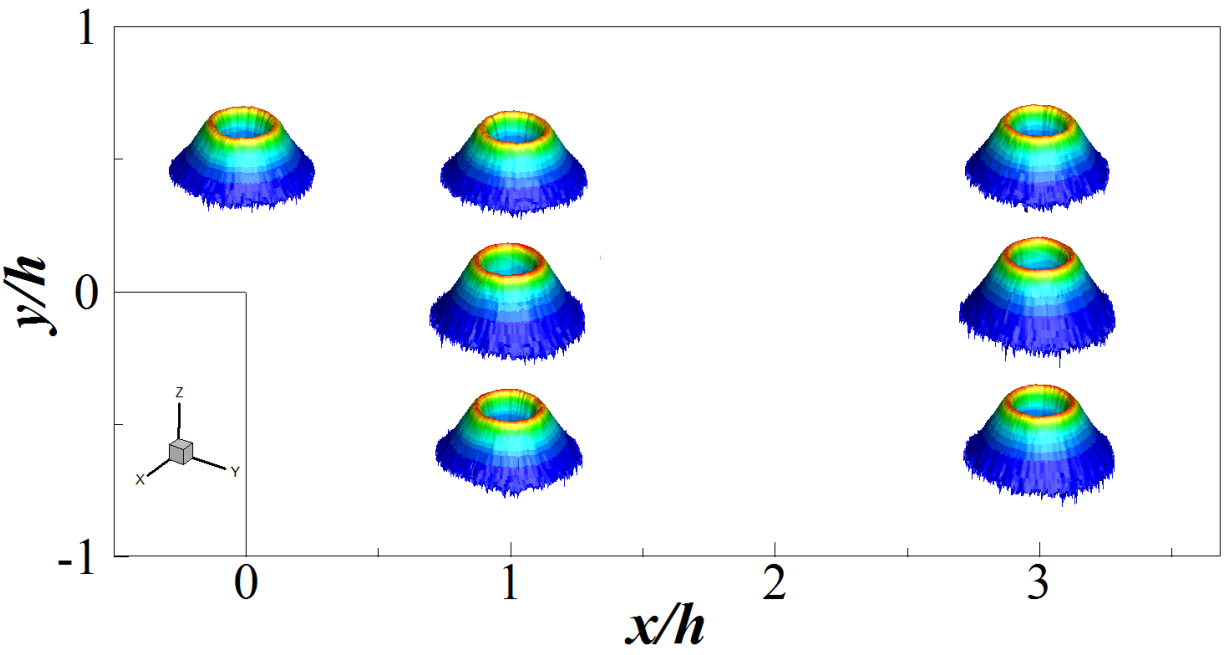

Figure 6.14: Local dissipation scale PDF $Q(\eta/\eta_{peak})$ measured at downstream of the backward facing step at seven positions at all directions (angle ranging from 0° to 360°). Local dissipation scale was calculated from V_θ , where θ indicates perpendicular direction.

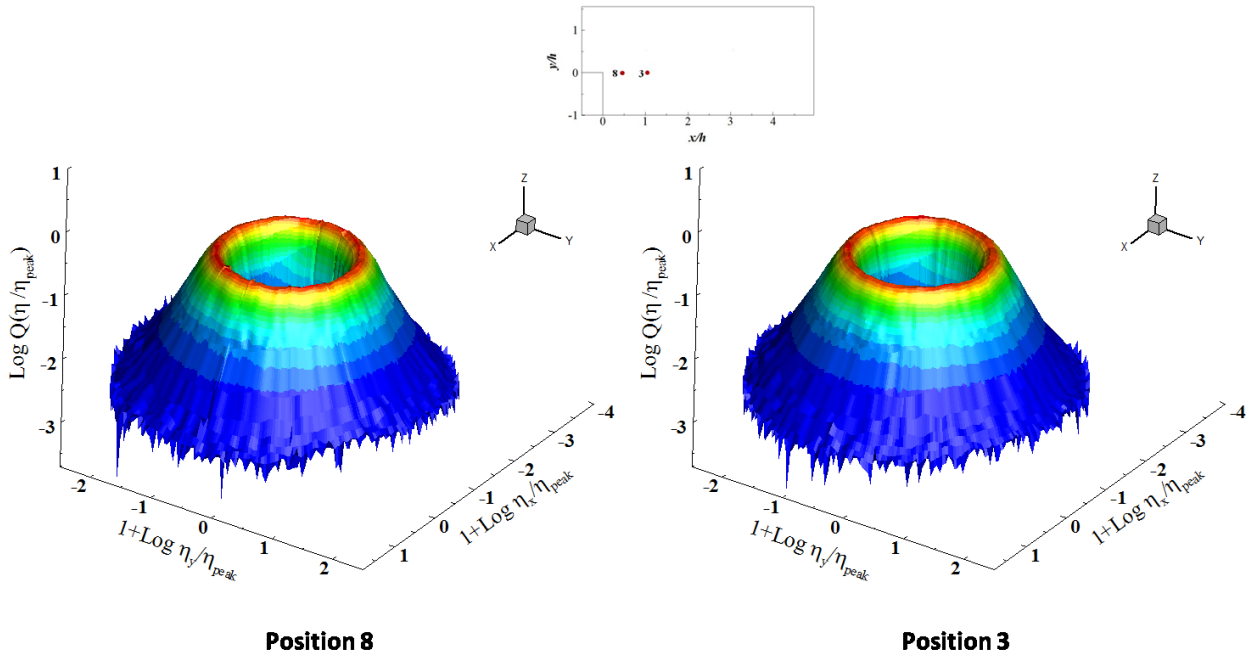

Figure 6.15: Local dissipation scale PDF $Q(\eta/\eta_{peak})$ measured at downstream of the backward facing step at position 3 and position 8 at all directions (angle ranging from 0° to 360°). Local dissipation scale was calculated from V_r , where r indicates parallel direction. Position 8 has higher magnitude of shear comparing with position 3.

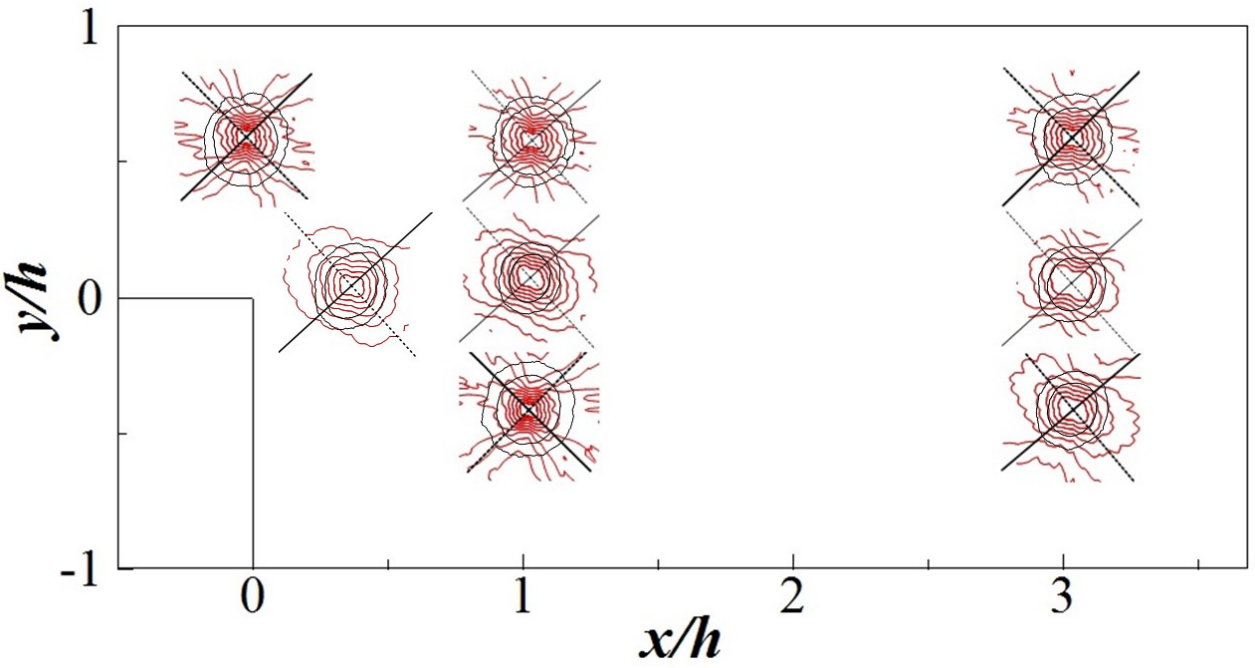

Figure 6.16: Red contours indicates two point correlation function of $\rho_{r\beta}(m)$, where β range from 0°to 360° and r indicates parallel direction of β. Solid line indicates principal axis along stretch direction while dashed line indicates principal axis contraction direction. Contours of Q(η) are shown in black for V_r velocity component at all seven positions.

6.5 Analytical derivation of *Q(η)*

In this section theoretical derivation of *Q(η)* will be provided for both homogeneous isotropic turbulence (HIT) and inhomogeneous anisotropic turbulence (IHAT) and an expression of η_{peak} will be provided as well. Let's assume a fluctuating turbulent velocity field in an Eulerian frame of reference. For a given position and direction $\hat{r}$, the integral length scale L, the directional gradient to quantify local large scale inhomogeneity γ and kinematic viscosity ν.

$$\gamma = \frac{du\prime}{dr} \tag{6.3}$$

$$Re_L = \frac{u'L}{\nu} \tag{6.4}$$

$$C_I = \frac{\gamma L}{u'} \tag{6.5}$$

Where Re_L is the local turbulence Reynolds number and $C_I$is the dimensionless local inhomogeneity parameter. Analytical distribution of *Q(η)* can be expressed as function of above non-dimensional parameters and can be expressed as follows:

$$Q(\eta) = F(\eta, Re_L, C_I) \tag{6.6}$$

Now analytical form of *F* can be derived assuming the Eulerian fluctuating velocity signals are Gaussian (L Biferale, 2008; Yakhot, 2006). With Gaussian assumptions velocity distribution $\delta_\eta u$, simplified to normally distributed and variance is equal to:

$$u'^2(\vec{x} + \eta\hat{r}) + u'^2(\vec{x}) - 2\rho u'(\vec{x} + \eta\hat{r})u'(\vec{x}) \tag{6.7}$$

For homogeneous isotropic turbulence (HIT), the variance can be simplified to:

$$2u'^2(1 - \rho) \tag{6.8}$$

With following assumption (equation 6.9), the folded Gaussian distribution can be express using equation 6.10

$$\frac{2u'^2}{\gamma^2} = \frac{Re_L^2}{L^2} \tag{6.9}$$

$$f\left(\left|\frac{\delta_\eta u\ \eta}{\gamma}\right|; \frac{\eta}{L}\right) = \frac{1}{Re_L\sqrt{\pi(1-\rho)}}\ \frac{L}{\eta}\ e^{-\frac{\left|\frac{\delta_\eta u\ \eta}{\gamma}\right|^2}{4Re_L^2(1-\rho)(\frac{\eta}{L})^2}} \tag{6.10}$$

By considering the profile only at $|\delta_\eta u|\eta/\nu = 1$, assuming *C* as an appropriate normalization parameter the final form of the analytical *Q(η)* distribution for homogenous isotropic turbulence (HIT) can be expressed as :

$$Q\left(\frac{\eta}{L}\right) = \frac{C}{Re_L\frac{\eta}{L}\sqrt{(1-\rho)}} e^{-\frac{1}{4Re_L^2(\frac{\eta}{L})^2(1-\rho)}} \tag{6.11}$$

The longitudinal two point correlation function ρ for small η can be obtained as follows:

$$\rho = \frac{\overline{u+\eta\frac{du}{dr}}}{\sqrt{u^2}\sqrt{(u+\eta\frac{du}{dr})^2}} \tag{6.12}$$

Applying homogeneity the above equations can be simplified as:

$$\rho = \frac{1}{\sqrt{1+(\frac{\eta}{\lambda_r})^2}} \tag{6.13}$$

Where λ_r is a generalization of the Taylor micro-scale which closely relates to the classical Tylor micro-scale λ_g as $\lambda_r = \lambda_g/2$ for the case of homogeneous isotropic turbulence (HIT).

Equation 6.11 and 6.13 are the analytical form respectively for *Q(η)* and ρ for homogeneous isotropic turbulence (HIT), with similar assumptions this derivation can be extended for inhomogeneous anisotropic turbulence (IHAT). Again considering the local fluctuating velocity in an Eulerian frame of reference and assuming the velocity signals are Gaussian, the variance of velocity increments $\delta_\eta u$ given by similar as equation 6.7. This can be simplified by expressing $u(\vec{x}+\eta\hat{r})$ with its first order Taylor approximation $u(\vec{x})(1+\frac{\eta}{L}C_I)$. The variance equation for inhomogeneous anisotropic turbulence becomes:

$$u'^2\left[(2-2\rho)\left(1+\frac{\eta}{L}C_I\right)+(\frac{\eta}{L}C_I)^2\right] \tag{6.14}$$

The analytical distribution for *Q(η)* for the inhomogeneous anisotropic turbulence (IHAT) can be expressed as:

$$Q\left(\frac{\eta}{L};C_I\right)=\frac{C*(\frac{\eta}{L})^{-1}}{Re_L\sqrt{(2-2\rho)\left(1+\frac{\eta}{L}C_I\right)+(\frac{\eta}{L}C_I)^2}}e^{-\frac{1}{2Re_L^2(\frac{\eta}{L})^2\left[(2-2\rho)\left(1+\frac{\eta}{L}C_I\right)+(\frac{\eta}{L}C_I)^2\right]}} \tag{6.15}$$

The two point correlation function corresponds to inhomogeneous anisotropic turbulence (IHAT) using Taylor approximation for small η can be simplified as:

$$\rho=\frac{1+\frac{\eta}{L}C_I}{\sqrt{1+2\frac{\eta}{L}C_I+(\frac{\eta}{\lambda})^2}} \tag{6.16}$$

When there is no inhomogeneity is turbulence (or $C_I=0$), equation 6.16 can be decomposed to equation 6.13, two point correlation function expression for homogeneous isotropic turbulence (HIT) . Expression for η_{peak} using equation 6.15 can be obtained as follows:

$$\eta_{peak}=\frac{L}{Re_L\sqrt{(2-2\rho)\left(1+\frac{\eta}{L}C_I\right)+(\frac{\eta}{L}C_I)^2}} \tag{6.17}$$

Comparing the above equation with $\eta_{peak}=LRe_L^{-\alpha}$ the exponent $\alpha=\frac{\log(\eta_{peak}/L)}{\log(Re_L)}$.

6.6 Summary

From lacunarity analysis of the instantaneous dissipation rate signal, lower lacunarity was observed at higher shear positions (position 3 and position 6). Lower lacunarity indicates that the mass signal fluctuates less relative to its mean. PDFs of instantaneous dissipation rate indicate peak shifted towards right in presence of strong mean shear. Hamlington et al. (P. E. Hamlington et al., 2012) observed similar kind of shift in near wall of channel flow DNS study. Three hypotheses were proposed by observing influence of shear on local dissipative scales. PDFs at

360° directions of instantaneous dissipation scale shows that positions located in the strong mean shear exhibit elliptical peak shape, while positions located at relatively lower mean shear exhibit circular peak shape. A new normalization parameter η_{peak} was proposed to normalize the distribution of instantaneous dissipation scale, η. Analytical derivation for $Q(\eta)$ and η_{peak} was shown for homogeneous isotropic turbulence (HIT) and inhomogeneous anisotropic turbulence (IHAT).

Chapter 7

DISCUSSION & CONCLUSION

7.1 Summary

Second order structure functions and log derivative of second order structure functions were evaluated in four different directions (streamwise and wall normal directions and principal axis directions) in a channel flow with backward facing step. Interrogation positions were chosen such that they represent free stream region, shear zone and separated region. Anisotropic characteristics effect of both dissipative scales and non-dissipative scales were discussed in this study. Magnitude of exponent decreases with increase of Reynolds number, indicating intermittency effect due to increased shear at higher Reynolds number. Some interesting phenomenon regarding separation of exponents in both dissipative and non-dissipative scales observed due to increased shear was discussed in details in this chapter. Three hypotheses that were proposed in chapter 7 were validated with experimental evidence and previously published papers in this chapter.

7.2 Mean flow & Anisotropy

In what follows the variations in the small-scale structure of turbulence in the presence of strong anisotropy has been elucidated based on current observations outlined in the chapter 6. This is done at the smallest resolvable scale (the dissipative scale) and the intermediate scales (non-dissipative scales). It should be noted that this study is not an attempt to test the validity of the scaling behavior predicted by the refined similarity hypothesis. While from the turbulence theory

standpoint, knowledge of the applicability of the similarity hypothesis or the multi-fractal framework is important, it is also important to understand how large-scale anisotropy affects the local structure from the mechanistic perspective. The second order SF is closely related to the power spectrum as is implied in the classical turbulence theory and therefore the results and insights presented here are relevant to spectral filter modeling of anisotropic separated turbulent flows. Previous studies similar to this exercise include Toschi (Toschi et al., 1999) who studied the variations in scaling exponents in a channel flow. The present study is a more robust test of conclusions drawn previously as the flow has a free shear region embedded within the channel flow through the placement of the backward facing step. Therefore the physical mechanics between wall-generated turbulence are presumed to be different than that in free shear.

7.2.1 Effect of shear on the small-scale structure

The data presented in this work includes a collection of SFs and their exponent profiles in a turbulent shear flow at points experiencing varying levels of anisotropy through the non-homogenous mean shear imposed by the backward facing step geometry. Points 1, 4, and 7 (Figure 3.6) lie in the free stream with relatively mild levels of mean shear as evident from the deformation eigen value magnitudes presented in Table 4.1. Points 3 and 6 however lie in an intense free shear layer, while points 2 and 5 lie in the separated vortex with mean deformation directions characteristically different (see Figure 4.7 and Table 4.2). Effects of these anisotropic characteristics on the SFs in the dissipative scales (smallest resolved scales, < Taylor micro-scale) and the non-dissipative scales (> Taylor micro-scale) are presented below:

7.2.2 Reduction in exponent magnitude with increasing shear

As seen in Figures 5.2 and 5.3, all the $u'^2_{\alpha\beta}$ profiles show a significant reduction in magnitude (so called saturation of exponent) throughout the dissipative scales for regions corresponding to high shear (points 3, and 6). Some of these reductions are also noticeable at point 5 that lies within the edge of the diffusing shear layer. The exponent however does not appreciably change in the non-dissipative scales. This is consistent with many of the previous findings that correlate intermittency in the dissipative scales with decreased or saturated scaling exponents(K. R. Sreenivasan & Antonia, 1997; Yakhot & Sreenivasan, 2005). The results also show a Reynolds number dependent reduction in the exponent magnitude. In particular the exponent is lower with increasing Reynolds number. These results clearly implicate an increase in intermittency in the dissipative regime due to the large-scale shear with increasing Reynolds number. They also show that the effects of large-scale are more pronounced in the dissipative scales as opposed to the non-dissipative scales.

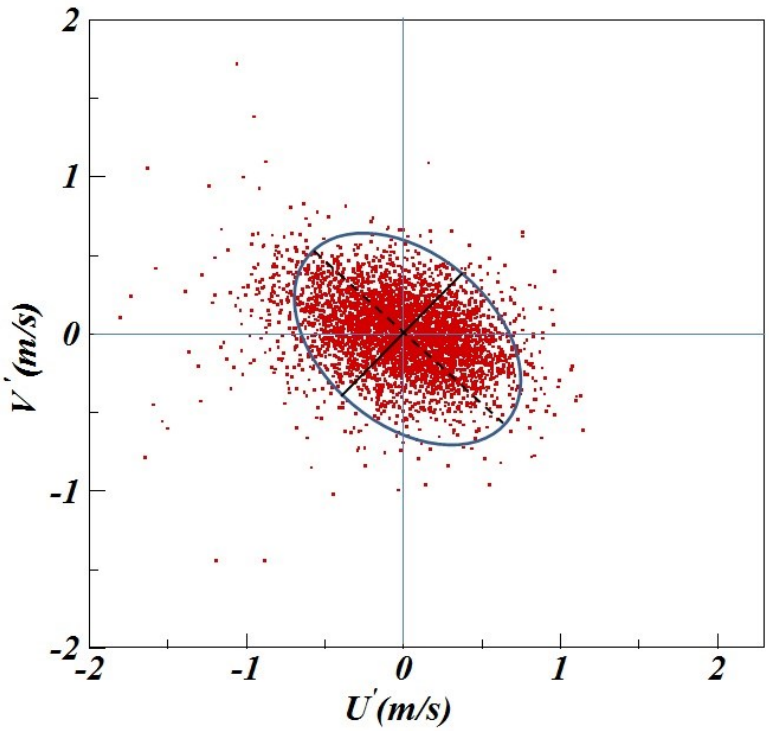

Figure 7.1: Scatter plots of fluctuation velocity at position 3

As seen in Figure 5.4(b) the exponents in the dissipation regime differ with respect to the velocity component utilized in the SF. The wall-normal velocity component SF has an exponent significantly higher than the streamwise velocity component SF irrespective of the SF direction. Increase in Reynolds number appears to pronounce this effect as seen in the Figure. The same observation also goes with the SFs along the principal directions (seen in Figure 5.5b). Here the SF exponent of velocity component along the mean stretch direction (e_1) is higher than that corresponding to the e_2 direction. These observations show that the anisotropic effects on dissipative scaling characteristics occur through the anisotropic nature of velocity fluctuations. A

picture of the scatter plot of the velocity fluctuation at point 3, representing a point in the shear layer is shown in Figure 7.1. As can be seen, the *i* component of the velocity is expected to have a greater rms than the *j* component. While in the e_1 and e_2 direction, it can be noted that the e_2 component of the velocity has a greater rms than the e_1 component. This can be inferred as the scatter plot of velocity may be also regarded as the relative lagrangian displacement of fluid elements per unit time, thus justifying the superposition of the SF directions onto the scatter plot. Combining this observation with that seen in Figures 5.4b and 5.5b, it may be inferred that saturation of the scaling exponent profile is higher corresponding to the velocity component with the greater rms magnitude (regardless of what direction the SF is in).

7.2.4 Separation of exponent in the non-dissipative scales with increasing shear

As seen again in Figure 5.4(b), the exponents in the non-dissipative scales differ with respect to SF direction. This is in contrast to the separation of exponents with respect to velocity component in the dissipative regime. The wall-normal direction SFs has a lower exponent magnitude than the streamwise direction SF irrespective of the velocity component. This observation shows a clear directional dependence of SFs in scales above the dissipative scales. This is consistent with some observations related to transverse SFs in literature reported and discussed in Ref.(Dhruva, Tsuji, & Sreenivasan, 1997) about reduced magnitudes of exponents of SFs in the transverse directions. With respect to e_1 and e_2 directions, Figure 5.3(b) however shows that this separation in exponent in the non-dissipative scales is greatly diminished. This combined observation shows that the exponent magnitude above the dissipative scales is sensitive to shear along a given direction. Given that by construction, e_1 and e_2 are directions where shear vanishes and the deformation is purely

stretch or contraction, the difference in exponents is insignificant. This can be observed in the agreement of exponents seen in Figure 5.5(a-c).

7.3 Dissipative Scale

Three hypotheses have been presented in chapter 6 that describes the influence of mean shear on dissipative scales. Hypotheses (1) and (2) were in fact anticipated by Corrsin (Corrsin, 1958) who argued on the basis of competition between the local energy transfer time scale and the normalized mean shear time scale captured by $S\tau_n$. It was also noted that the above dimensional arguments can also be formulated on the fluctuating turbulent velocity field. It is easy to see that Re_S can be expressed in terms of the fluctuating dissipation scale η as $Re_S \sim \langle (S\eta^2/\nu)^{-2} \rangle$ Thus, one may pose the same arguments as above without invoking dimensional analysis, by defining an alternative shear-dissipation scale Reynolds number as a moment defined over $Q(\eta)$ given by $\int_0^L (S\eta^2/\nu) Q(\eta) d\eta$. Thus, the local dissipation dynamics departs from the isotropic expectation if instantaneously the number $S\eta^2/\nu \gg 1$. Physically, this represents the cut-off where locally $S_\eta \gg \delta_n u$. With regards to hypothesis (3), it indicates the possible existence of a more general universality class for the small-scale structure of turbulence that is applicable for all shear flows as long as the mechanism of turbulence production is purely shear driven, and that the classical picture is only a special case when shear vanishes. Now, the existence of a universal structure that is shear dependent may sound like an oxymoron given that mean shear has classically been associated with the large-scale. But it could be true if and only if the very mechanism of shear driven turbulence production itself were to be universal. In other words, the turbulent production mechanisms in the strong shear region of a free jet is statistically identical to turbulent production

in a mixing layer or even a boundary layer provided the relevant dimensionless numbers (i.e., Re_L and Re_S as suggested above) are matched. Combining this notion of a universal turbulence production structure with the underlying universal multi-fractal structure, the nature of the small-scale structure is hypothesized to obey a new class of universality that is dependent on precisely the relative position of the production scales (defined by Re_S) with respect to the separation of turbulent scales. These ideas extend the classical notion of universality, which still holds as a special case at vanishing shear and, as discussed in the context of the data presented in the remainder of this letter, remains to be a very good approximation for $Re_S \geq 40$.

Using current data and previously published data, a preliminary test for hypothesis (1) through (3) was performed. This was done by recasting both our data and the shear flow data from Refs. (Bailey et al., 2009; P. E. Hamlington et al., 2012) to analyze the departure of $Q(\eta/\eta_0)$from the HIT expectation as a function of Re_S. Figure 6.4 shows a plot of the peak location of $Q(\eta/\eta_0)$, $(\eta/\eta_0)_{peak}$ as a function of Re_S for the six locations. The figure also shows the predicted curves for turbulent channel flows for $Re_\tau \sim 550$ and $Re_\tau \sim 180$. These predictions were based on $(\eta/\eta_0)_{peak}$ presented in Ref. (P. E. Hamlington et al., 2012) combined with $\langle\varepsilon\rangle/(S^2\nu)$ calculated from the freely distributed channel flow data of Ref.(Hoyas & Jiménez, 2008). Pipe flow data at y/R = 0.1 in Ref. (Bailey et al., 2009) is also included, along with the level corresponding to HIT. It is clear from this composite data-set that at large Re_S, $(\eta/\eta_0)_{peak}$ approaches the HIT level, partially supporting hypothesis (1). The data also show a significant departure for $Re_S < 40$ with $(\eta/\eta_0)_{peak}$ increasing in magnitude. There appears to be an inflection for $Re_S \sim 1$ and a rapid increase in (η/η_0) peak for $Re_S < 1$. The significant deviation from HIT for $Re_S < 40$ supports hypothesis (2). All the data show reasonable collapse. The significantly higher $(\eta/\eta_0)_{peak}$ for Re_S ~30 in the PIV data was examined closer, and can be explained through the inherent limitation of

defining the integral length scale in strongly anisotropic flows (which is the next challenge to address before testing these hypotheses in much stronger anisotropic flows). This data point corresponds to position 2, which lies within the separated zone. The point is within 0.3 mm of the strong shear layer and thus, the longitudinal two-point correlation function inevitably traverses from low to high shear. It can be noted that if the position of this data point recalculated by revising the mean shear at this location as the average over the integral length scale, the data point shifts to the left and exactly falls in line further improving the collapse of data. It was also observed here that the $(\eta/\eta_0)_{peak}$ level corresponding to pipe data at $y/R = 0.1$ (Bailey et al., 2009) agrees more with the collapsed data than the HIT prediction. All of these observations with a reasonable data collapse seem to support hypothesis (3) with respect to the existence of a family of universal structures of turbulence. However, more studies are necessary to study this behavior in multi-directional anisotropy with a more general definition of integral length scale. To illustrate how Re_S significantly varies in space and can therefore play a significant role in the variation in local structures, Figure 6.5 shows profiles of Re_S as a function of y/h at $x \approx h$ and $x \approx 3h$. From this figure, it is clear that the shear layer indeed significantly reduces Re_S particularly along $y/h = 0$. Figure 6.6 shows profiles of Re_S as a function of y^+ in channel flows based on Ref. (Hoyas & Jiménez, 2008) for very high Re_τ. This figure clearly shows that roughly at $y^+ \sim 90$, $Re_\tau \sim 40$. This further explains the departure of $Q(\eta/\eta_0)$ from the HIT behavior for $y^+ < 90$.6 It also explains the departure observed in our data for regions with large mean shear in the free shear layer downstream of the backward step.

7.4 Dissipative scales, SFs and TPCFs at 360°

Distribution of dissipation scales $Q(\eta)$ at the different interrogation positions with varying shear intensity indicate that when normalized by η_0, results show that they are greatly influenced by the intensity and the direction of local mean shear. Contour lines corresponding to the peak of $Q(\eta)$ look elliptical for strong shear, while the shape is more circular for low shear intensity. A new normalization parameter $\eta_{peak}$was proposed in this paper. After using this new normalization parameter, no difference was observed in the peak location shapes between low shear positions and high shear positions.

The Major and the minor axis of elliptical shape contours indicate that velocity fluctuation correlations are more correlated along the minor axis and less correlated along the major axis. When their difference between major and minor axis decreases and contours looks like circular, indicating velocity fluctuation relations are similar in both directions. Non-connected contours in the non-dissipative region are due to negative correlations between two successive positions, while in dissipative regions successive values are close to each other. Contours in the strong shear position is sandwiched (or contracted), while moving towards the downstream less evidence of contraction, that means as shear decreases the velocity fluctuation correlations tends to be similar in all directions.

7.4 Conclusion

Second-order SFs in a strongly anisotropic flow was studied, namely the canonical backward facing step using time-resolved particle image velocimetry technique. The large-scale anisotropic field presented is non-monotonic with an intense shear layer embedded between a free stream channel flow and a separated vortex. The second-order SFs were observed to be highly impacted by the non-monotonic variations in turbulence intensities. These impacts could be traced down to the dissipative regime through analysis of the logarithmic derivatives of second-order SFs. It was shown that presence of shear separates the exponent profile in the dissipative regime with respect to anisotropic fluctuations of the velocity component. Specifically, the velocity component that fluctuates most corresponds to saturated exponent in the dissipation regime while not necessarily saturating the exponent in the non-dissipative regime. Another key observation is that the scaling exponents for SFs along the principal directions of deformation do not separate with respect to SF direction. Thus the transverse scaling exponent would be saturated if it is not oriented along the principal axis of mean flow deformation.

The above observations are unique and provide more insight into the mechanism of how anisotropy can impact SF scaling behavior. It was also shown that the kinematic deformation of the mean flow, characterized through the principal axis of deformation, present varying levels of mean shear influence with respect to the direction of the SF as well as the velocity component of the SF.

This study has shown the relevance of considering local anisotropic parameters such as the mean shear in tackling the problem of understanding the departure of small-scale structure of turbulence in strongly anisotropic yet high Reynolds number flows from that observed for the case of HIT. Through physical arguments, it was proposed that there may exist a family of universal structures

of turbulence through the introduction of the mean shear Reynolds number Re_S or equivalently the ratio of mean shear time scale to turbulence time scale ST_L. Alternatively, it can also be described by the Reynolds number $\int_0^L (S\eta^2/\nu)Q(\eta)d\eta$. Our high-resolution PIV measurements in the backward facing step not only shows that the fluctuation in dissipation rate becomes relatively less intermittent in the presence of strong shear (through fractal analysis), but also that the peak location of $Q(\eta/\eta_0)$ shifts to the right. This shift is consistent with near wall $Q(\eta/\eta_0)$ in channel flows where mean shear is high. By combining current data and performing meta-analysis of previous data in channel flow turbulence, it was shown that Re_S <40 significantly marks the shift for the small-scale structure from HIT behavior. Partial evidence was shown that this shift may still be universal as current data, which consist of free-shear turbulence, agree with the wall-bounded turbulence and HIT when parameterized with Re_S. However, further detailed investigations of increasingly complex anisotropic turbulent flows with strong principal shear as well as a generalized definition of integral length scale independent of the two-point correlation functions are needed.

Probability density functions of the instantaneous dissipative scales at 360° directions indicates that local mean shear dominate the peak locations shape when $Q(\eta)$ was normalized with η_0. While introducing new normalization parameter η_{peak}, shear dominances in peak locations can be overcome. Therefore, probability density functions of the instantaneous dissipative scale can be universal. However, more investigation is required.

Chapter 8

ORIGINAL CONTRIBUTION

8.1 Journal Papers

1. Khandakar Morshed, David Bark Jr.,Marcio Forleo, Lakshmi Dasi (2014), “Theory to Predict Shear Stress on Cells in Turbulent Blood Flow”. PLOS ONE. DOI: 10.1371/journal.pone.0105357 (Khandakar Niaz Morshed, Bark Jr, Forleo, & Dasi, 2014)
2. Khandakar Morshed, Subhas K Venayagamoorthy, Lakshmi P Dasi (2013) "Intermittency and local dissipation scales under strong mean shear ". Physics of Fluids, Volume 25, 011701, DOI: 10.1063/1.4774039 (Khandakar Niaz Morshed, Subhas Karan Venayagamoorthy, et al., 2013)
3. Khandakar Morshed, Lakshmi P Dasi (2013) “Effect of strong anisotropy on the dissipative and non-dissipative regimes of the second order structure function”. Experiments in Fluids, Volume 54, Issue 5, DOI: 10.1007/s00348-013-1521-7 (K. N. Morshed & L. P. Dasi, 2013)
4. Ian May, Khandakar Morshed, Subhas Venoyagamoorthy, and Lakshmi Dasi, (2014) “On the universality of local dissipation scales in turbulent flows” (under review)
5. Khandakar Morshed, Lakshmi Dasi, “Alignment of two-point statistics in anisotropic turbulent flows” (to be submitted)

8.2 Conference Papers

1. Lakshmi Prasad Dasi, Khandakar Niaz Morshed, Marcio Forleo (2013) “Phenomenology of hemolysis in turbulent flows”, Proceedings of the ASME 2013 Summer Bioengineering Conference SBC2013, Sunriver, Oregon, USA (June 26-29, 2013) (Lakshmi Prasad Dasi, Morshed, & Forleo, 2013)

8.3 Conference Presentations

1. Ian May, Khandakar Morshed, Subhas Venoyagamoorthy, and Lakshmi Dasi, (2014) “On the universality of local dissipation scales in turbulent flows” 67th Annual Meeting, Division of Fluid Dynamics, American Physical Society, San Francisco, California, USA. (November 23-25, 2014) (May, Morshed, Venayagamoorthy, & Dasi, 2014)
2. Khandakar Morshed, and Lakshmi Dasi, (2014) “Local dissipation scales in strongly inhomogeneous turbulent shear flows” 67th Annual Meeting, Division of Fluid Dynamics, American Physical Society, San Francisco, California, USA. (November 23-25, 2014) (K. Morshed & Dasi, 2014)
3. Khandakar Morshed, Lakshmi Dasi (2013) " Alignment of two-point statistics with respect to mean deformation field in anisotropic turbulent flows" 66th Annual Meeting, Division of Fluid Dynamics, American Physical Society, Pittsburgh, Pennsylvania, USA. (November 24-26, 2012) (K. Morshed & L. Dasi, 2013)
4. Khandakar Morshed, Subhas Venayagamoorthy, Lakshmi Dasi (2012) "Mean shear regulates the intermittency of energy dissipation rate " 65th Annual Meeting, Division of

Fluid Dynamics, American Physical Society, San Diego, California, USA. (November 18-20, 2012) (K. Morshed, Venayagamoorthy, & Dasi, 2012)

8.4 Poster Presentations

1. Kandakar Niaz Morshed, Marcio Forleo, Lakshmi Prasad Dasi, "Phenomenology of hemolysis in turbulent flows", ASME 2013 Summer Bioengineering Conference SBC2013, Sunriver, Oregon, USA (June 26-29, 2013) (Lakshmi Prasad Dasi et al., 2013)
2. Kandakar Niaz Morshed, Marcio Forleo, Lakshmi Prasad Dasi, "Understanding shear induced hemolysis in turbulent flows", Colorado State University Research Colloquium 2013, Fort Collins, Colorado, USA (April 4-5, 2013) (Kandakar Niaz Morshed, Forleo, & Dasi, 2013)

REFERENCES

Adrian, R. J. (2005). Twenty years of particle image velocimetry. *Experiments in Fluids, 39*(2), 159-169.

Adrian, R. J. (2007). Hairpin vortex organization in wall turbulence. *Physics of Fluids, 19*, 041301.

Alam, M. F., Walters, D. K., & Thompson, D. S. (2011). *A new hybrid RANS/LES modeling methodology for CFD applications*. Paper presented at the ASME-JSME-KSME 2011 Joint Fluids Engineering Conference.

Albrecht, H.-E. (2003). *Laser Doppler and phase Doppler measurement techniques*: Springer Verlag.

Allain, C., & Cloitre, M. (1991). Characterizing the lacunarity of random and deterministic fractal sets. *Physical Review A, 44*(6), 3552-3558.

Arad, I., Dhruva, B., Kurien, S., L'Vov, V. S., Procaccia, I., & Sreenivasan, K. R. (1998). Extraction of anisotropic contributions in turbulent flows. *Physical Review Letters, 81*(24), 5330-5333. doi: 10.1103/PhysRevLett.81.5330

Armaly, B., Li, A., & Nie, J. (2003). Measurements in three-dimensional laminar separated flow. *International journal of heat and mass transfer, 46*(19), 3573-3582.

Armaly, B. F., Durst, F., & Pereira, J. C. F. (1983). Experimental and theoretical investigation of backward-facing step flow. *Journal of Fluid Mechanics, 127*, 473-496.

Bailey, S., Hultmark, M., Schumacher, J., Yakhot, V., & Smits, A. (2009). Measurement of Local Dissipation Scales in Turbulent Pipe Flow. *Physical Review Letters, 103*(1), 4-4. doi: 10.1103/PhysRevLett.103.014502

Batchelor, G. K. (1953). *The theory of homogeneous turbulence*: Cambridge university press.

Benzi, R., Biferale, L., & Toschi, F. (2003). Intermittency in Turbulence: Multiplicative random process in space and time. *Journal of Statistical Physics, 113*(5-6), 783-798.

Bi, W. T., & Wei, Q. D. (2003). Scaling of longitudinal and transverse structure functions in cylinder wake turbulence. *Journal of Turbulence, 4*.

Biferale, L. (2008). A note on the fluctuation of dissipative scale in turbulence. *Physics of Fluids, 20*, 031703.

Biferale, L., Calzavarini, E., Lanotte, A. S., Toschi, F., & Tripiccione, R. (2004). Universality of anisotropic turbulence. *Physica a-Statistical Mechanics and Its Applications, 338*(1-2), 194-200. doi: 10.1016/j.physa.2004.02.041

Biferale, L., Lohse, D., Mazzitelli, I. M., & Toschi, F. (2002). Probing structures in channel flow through SO(3) and SO(2) decomposition. *Journal of Fluid Mechanics, 452*, 39-59. doi: 10.1017/s0022112001006632

Bradshaw, P., & Wong, F. (1972). The reattachment and relaxation of a turbulent shear layer. *Journal of Fluid Mechanics, 52*(01), 113-135.

Castaing, B., Gagne, Y., & Hopfinger, E. (1990). Velocity probability density functions of high Reynolds number turbulence. *Physica D: Nonlinear Phenomena, 46*(2), 177-200.

Chandrasuda, C. (1975). *A reattaching turbulent shear layer in incompressible flow.* Imperial College London (University of London).

Chandrsuda, C., Mehta, R., Weir, A., & Bradshaw, P. (1978). Effect of free-stream turbulence on large structure in turbulent mixing layers. *Journal of Fluid Mechanics, 85*(4), 693-704.

Chen, S., Sreenivasan, K. R., Nelkin, M., & Cao, N. (1997). Refined similarity hypothesis for transverse structure functions in fluid turbulence. *Physical Review Letters, 79*(12), 2253.

Citriniti, J. H. (2000). Reconstruction of the global velocity field in the axisymmetric mixing layer utilizing the proper orthogonal decomposition. *Journal of Fluid Mechanics, 418*(2000), 137.

Corrsin, S. (1958). *Local isotropy in turbulent shear flow*: National Advisory Committee for Aeronautics.

Dasi, L. P., Morshed, K. N., & Forleo, M. (2013). *Phenomenology of Hemolysis in Turbulent Flows*. Paper presented at the ASME 2013 Summer Bioengineering Conference.

Dasi, L. P., Schuerg, F., & Webster, D. R. (2007). The geometric properties of high-Schmidt-number passive scalar iso-surfaces in turbulent boundary layers. *Journal of Fluid Mechanics, 588*(-1), 253-277.

De Karman, T., & Howarth, L. (1938). On the statistical theory of isotropic turbulence. *Proceedings of the Royal Society of London. Series A, Mathematical and Physical Sciences, 164*(917), 192-215.

Dhruva, B., Tsuji, Y., & Sreenivasan, K. R. (1997). Transverse structure functions in high-Reynolds-number turbulence. *Physical Review E, 56*(5), R4928-R4930.

Eaton, J., & Johnston, J. (1981). A review of research on subsonic turbulent flow reattachment. *AIAA journal, 19*(9), 1093-1100.

Eaton, J. K., & Johnston, J. (1980). *Turbulent flow reattachment: an experimental study of the flow and structure behind a backward-facing step*: Stanford University.

Favre, A., Gaviglio, J., & Dumas, R. (1967). Structure of Velocity Space-Time Correlations in a Boundary Layer. *Physics of Fluids, 10*, S138.

Garg, S., & Warhaft, Z. (1998). On the small scale structure of simple shear flow. *Physics of Fluids, 10*(3), 662-673. doi: 10.1063/1.869592

Gefen, Y., Meir, Y., Mandelbrot, B. B., & Aharony, A. (1983). Geometric implementation of hypercubic lattices with noninteger dimensionality by use of low lacunarity fractal lattices. *Physical Review Letters, 50*(3), 145-148.

Goldstein, R. J. (1996). *Fluid mechanics measurement*: CRC PressI Llc.

Gotoh, T., Fukayama, D., & Nakano, T. (2002). Velocity field statistics in homogeneous steady turbulence obtained using a high-resolution direct numerical simulation. *Physics of Fluids, 14*, 1065.

Gualtieri, P., Casciola, C., Benzi, R., Amati, G., & Piva, R. (2002). Scaling laws and intermittency in homogeneous shear flow. *Physics of Fluids, 14*, 583.

Gurvich, A., & Yaglom, A. (1967). Breakdown of eddies and probability distributions for small-scale turbulence. *Physics of Fluids, 10*, S59.

Hamlington, P. E., Krasnov, D., Boeck, T., & Schumacher, J. (2012). Local dissipation scales and energy dissipation-rate moments in channel flow. *Journal of Fluid Mechanics, 701*, 419-429. doi: 10.1017/jfm.2012.170

Hamlington, P. E., Krasnov, D., Boeck, T., & Schumacher, J. (2012). Statistics of the energy dissipation rate and local enstrophy in turbulent channel flow. *Physica D: Nonlinear Phenomena, 241*(3), 169-177. doi: http://dx.doi.org/10.1016/j.physd.2011.06.012

Holmes, P. J., Lumley, J. L., Berkooz, G., Mattingly, J. C., & Wittenberg, R. W. (1997). Low-dimensional models of coherent structures in turbulence. *Physics Reports, 287*(4), 337-384.

Hoyas, S., & Jiménez, J. (2006). Scaling of the velocity fluctuations in turbulent channels up to Re= 2003. *Physics of Fluids, 18*, 011702.

Hoyas, S., & Jiménez, J. (2008). Reynolds number effects on the Reynolds-stress budgets in turbulent channels. *Physics of Fluids, 20*(10), 101511-101511. doi: 10.1063/1.3005862

Huang, Y., Schmitt, F., Lu, Z., Fougairolles, P., Gagne, Y., & Liu, Y. (2010). Second-order structure function in fully developed turbulence. *Physical Review E, 82*(2).

Huang, Y. X., Schmitt, F. G., Lu, Z. M., Fougairolles, P., Gagne, Y., & Liu, Y. L. (2010). Second-order structure function in fully developed turbulence. *Physical Review E, 82*(2). doi: 10.1103/PhysRevE.82.026319

Hussain, A. F. (1983). Coherent structures—reality and myth. *Physics of Fluids, 26*, 2816.

Ishihara, T., Kaneda, Y., Yokokawa, M., Itakura, K., & Uno, A. (2007). Small-scale statistics in high-resolution direct numerical simulation of turbulence: Reynolds number dependence

of one-point velocity gradient statistics. *Journal of Fluid Mechanics, 592*, 335-366. doi: 10.1017/s0022112007008531

Jiménez, J. (2000). Intermittency and cascades. *Journal of Fluid Mechanics, 409*(1), 99-120.

Jiménez, J. (2007). *Intermittency in turbulence.* Paper presented at the Extreme Events: Proc. 15th ‘Aha Huliko ‘a Hawaiian Winter Workshop, Honolulu, HI, US Office of Naval Research, the School of Ocean and Earth Science and Technology, and the Department of Oceanography, University of Hawaii at Manoa.

Jiménez, J., & Wray, A. A. (1998). On the characteristics of vortex filaments in isotropic turbulence. *J. Fluid Mech, 373*, 255-285.

Jovic, S., & Driver, D. (1994). Backward-Facing Step Measurements at Low Reynolds Number, Reh= 5000. *Nasa Technical Memorandum*(February).

Jovic, S., & Driver, D. (1995). Reynolds number effect on the skin friction in separated flows behind a backward-facing step. *Experiments in Fluids, 18*(6), 464-467.

Kailasnath, P., Sreenivasan, K., & Stolovitzky, G. (1992). Probability density of velocity increments in turbulent flows. *Physical Review Letters, 68*(18), 2766.

Kaneda, Y., & Ishihara, T. (2009). Universality in Statistics at Small Scales of Turbulence: A Study by High Resolution DNS. In M. Deville, T. H. Le & P. Sagaut (Eds.), *Turbulence and Interactions* (Vol. 105, pp. 55-76).

Kasagi, N., & Matsunaga, A. (1995). Three-dimensional particle-tracking velocimetry measurement of turbulence statistics and energy budget in a backward-facing step flow. *International journal of heat and fluid flow, 16*(6), 477-485.

Kaye, B. H. (1989). A random walk through fractal dimensions.

Kendall, M., & Stuart, A. (1977). The Advanced Theory of Statistics (4th edn.) Griffin. *New York*.

Kim, J., Moin, P., & Moser, R. (1987). Turbulence statistics in fully developed channel flow at low Reynolds number. *Journal of Fluid Mechanics, 177*(1), 133-166.

Kline, S., Reynolds, W., Schraub, F., & Runstadler, P. (1967). The structure of turbulent boundary layers. *Journal of Fluid Mechanics, 30*(04), 741-773.

Kolmogorov, A. (1941). The Local Structure of Turbulence in Incompressible Viscous Fluid for Very Large Reynolds' Numbers. *Doklady Akademiia Nauk SSSR*.

Kolmogorov, A. N. (1962). A refinement of previous hypotheses concerning the local structure of turbulence in a viscous incompressible fluid at high Reynolds number. *J. Fluid Mech, 13*(1), 82-85.

Kostas, J., Soria, J., & Chong, M. (2002). Particle image velocimetry measurements of a backward-facing step flow. *Experiments in Fluids, 33*(6), 838-853.

Kovasznay, L. S., Kibens, V., & Blackwelder, R. F. (1970). Large-scale motion in the intermittent region of a turbulent boundary layer. *J. Fluid Mech, 41*(2), 283-325.

Kurien, S., & Sreenivasan, K. R. (2001). Dynamical equations for high-order structure functions, and a comparison of a mean-field theory with experiments in three-dimensional turbulence. *Physical Review E, 64*(5), 056302.

Le, H., Moin, P., & Kim, J. (1997). Direct numerical simulation of turbulent flow over a backward-facing step. *Journal of Fluid Mechanics, 330*, 349-374. doi: 10.1017/s0022112096003941

Liepmann, H. W. (1952). Aspects of the turbulence problem. *Zeitschrift für Angewandte Mathematik und Physik (ZAMP), 3*(6), 407-426.

Lin, B., & Yang, Z. (1986). A suggested lacunarity expression for Sierpinski carpets. *Journal of Physics A: Mathematical and General, 19*(2), L49.

Lohse, D., & Grossmann, S. (1993). Intermittency in turbulence. *Physica A: Statistical Mechanics and its Applications, 194*(1), 519-531.

Longmire, E. K., & Eaton, J. K. (1992). Structure of a particle-laden round jet. *Journal of Fluid Mechanics, 236*, 217-257. doi: doi:10.1017/S002211209200140X

Mandelbrot, B. B. (1974). Intermittent turbulence in self-similar cascades- Divergence of high moments and dimension of the carrier. *Journal of Fluid Mechanics, 62*(2), 331-358.

Mandelbrot, B. B. (1983). *The fractal geometry of nature*: Times Books.

May, I., Morshed, K., Venayagamoorthy, K., & Dasi, L. (2014). *On the distribution of local dissipation scales in turbulent flows.* Paper presented at the Bulletin of the American Physical Society.

Mei, R. (1996). Velocity fidelity of flow tracer particles. *Experiments in Fluids, 22*(1), 1-13. doi: 10.1007/bf01893300

Meneveau, C., & Sreenivasan, K. (1991). The multifractal nature of turbulent energy dissipation. *Journal of Fluid Mechanics, 224*(429-484), 180.

Morshed, K., & Dasi, L. (2013). *Alignment of two-point statistics with respect to mean deformation field in anisotropic turbulent flows.* Paper presented at the Bulletin of the American Physical Society.

Morshed, K., & Dasi, L. (2014). Local dissipation scales in strongly inhomogeneous turbulent shear flows. *Bulletin of the American Physical Society, 59*.

Morshed, K., Venayagamoorthy, S., & Dasi, L. (2012). *Mean shear regulates the intermittency of energy dissipation rate.* Paper presented at the Bulletin of the American Physical Society.

Morshed, K. N. (2010). Experimental and numerical investigations on aerodynamic characteristics of Savonius wind turbine with various overlap ratios.

Morshed, K. N., Bark Jr, D., Forleo, M., & Dasi, L. P. (2014). Theory to Predict Shear Stress on Cells in Turbulent Blood Flow. *PloS one, 9*(8), e105357.

Morshed, K. N., & Dasi, L. P. (2013). Effect of strong anisotropy on the dissipative and non-dissipative regimes of the second-order structure function. *Experiments in Fluids, 54*(5), 1-19.

Morshed, K. N., Forleo, M., & Dasi, L. P. (2013). Understanding shear induced hemolysis in turbulent flows.

Morshed, K. N., Rahman, M., Molina, G., & Ahmed, M. (2013). Wind tunnel testing and numerical simulation on aerodynamic performance of a three-bladed Savonius wind turbine. *International Journal of Energy and Environmental Engineering, 4*(1), 1-14.

Morshed, K. N., Venayagamoorthy, S. K., & Dasi, L. P. (2013). Intermittency and local dissipation scales under strong mean shear. *Physics of Fluids, 25*(1), 011701.

Moser, R. D., Kim, J., & Mansour, N. N. (1999). Direct numerical simulation of turbulent channel flow up to Re= 590. *Physics of Fluids, 11*, 943.

Mouri, H., Takaoka, M., Hori, A., & Kawashima, Y. (2002). Probability density function of turbulent velocity fluctuations. *Physical Review E, 65*(5). doi: 10.1103/PhysRevE.65.056304

Mouri, H., Takaoka, M., Hori, A., & Kawashima, Y. (2003). Probability density function of turbulent velocity fluctuations in a rough-wall boundary layer. *Physical Review E, 68*(3), 036311.

Novikov, E. (1971). Intermittency and scale similarity in the structure of a turbulent flow. *Journal of Applied Mathematics and Mechanics, 35*(2), 266-277.

Obukhov, A. (1962). Some specific features of atmospheric turbulence. *Journal of Geophysical Research, 67*(8), 3011-3014.

Paladin, G., & Vulpiani, A. (1987). Anomalous scaling laws in multifractal objects. *Physics Reports, 156*(4), 147-225.

Piirto, M., Karvinen, A., Ahlstedt, H., Saarenrinne, P., & Karvinen, R. (2007). PIV measurements in square backward-facing step. *TRANSACTIONS-AMERICAN SOCIETY OF MECHANICAL ENGINEERS JOURNAL OF FLUIDS ENGINEERING, 129*(8), 984.

Piirto, M., Saarenrinne, P., Eloranta, H., & Karvinen, R. (2003). Measuring turbulence energy with PIV in a backward-facing step flow. *Experiments in Fluids, 35*(3), 219-236. doi: 10.1007/s00348-003-0607-z

Pilloni, M., Schram, C., & Riethmuller, M. (2000). *PIV and LDV measurements behind a backward facing step.* Paper presented at the International conference on air pollution.

Plotnick, R. E., Gardner, R. H., Hargrove, W. W., Prestegaard, K., & Perlmutter, M. (1996). Lacunarity analysis: a general technique for the analysis of spatial patterns. *Physical Review E, 53*(5), 5461.

Plotnick, R. E., Gardner, R. H., & O'Neill, R. V. (1993). Lacunarity indices as measures of landscape texture. *Landscape Ecology, 8*(3), 201-211.

Pope, S. B. (2000). *Turbulent flows*: Cambridge university press.

Raffel, M., Willert, C. E., & Kompenhans, J. (1998). *Particle Image Velocimetry: A Practical Guide*: Springer.

Reynolds, O. (1883). An experimental investigation of the circumstances which determine whether the motion of water shall be direct or sinuous, and of the law of resistance in parallel channels. *Proceedings of the Royal Society of London, 35*(224-226), 84-99.

Reynolds, O. (1895). On the dynamical theory of incompressible viscous fluids and the determination of the criterion. *Philosophical Transactions of the Royal Society of London. A, 186*, 123-164.

Richardson, L. (1922). Weather prediction by numerical process Cambridge University Press. *Cambridge, England*, 219.

Schumacher, J. (2007). Sub-Kolmogorov-scale fluctuations in fluid turbulence. *Europhysics Letters (EPL), 80*(5), 54001-54001. doi: 10.1209/0295-5075/80/54001

She, Z.-S., & Orszag, S. A. (1991). Physical model of intermittency in turbulence: Inertial-range non-Gaussian statistics. *Physical Review Letters, 66*(13), 1701-1704.

Smyth, R. (1979). Turbulent flow over a plane symmetric sudden expansion. *J. Fluids Eng.;(United States), 101*(3).

Sreenivasan, K. R. (1998). An update on the energy dissipation rate in isotropic turbulence. *Physics of Fluids, 10*, 528.

Sreenivasan, K. R. (1999). Fluid turbulence. *Reviews of Modern Physics, 71*(2), S383.

Sreenivasan, K. R., & Antonia, R. A. (1997). The phenomenology of small-scale turbulence. *Annual Review of Fluid Mechanics, 29*, 435-472.

Sun, C., Ren, L.-Y., Song, H., & Xia, K.-Q. (2005). Heat transport by turbulent Rayleigh-Bénard convection in 1 m diameter cylindrical cells of widely varying aspect ratio. *Journal of Fluid Mechanics, 542*, 165-174.

Tabeling, P., Zocchi, G., Belin, F., Maurer, J., & Willaime, H. (1996). Probability density functions, skewness, and flatness in large Reynolds number turbulence. *Physical Review E, 53*(2), 1613.

Tanaka, T., & Eaton, J. K. (2007). A correction method for measuring turbulence kinetic energy dissipation rate by PIV. *Experiments in Fluids, 42*(6), 893-902. doi: 10.1007/s00348-007-0298-y

Taylor, G. I. (1935). Statistical theory of turbulence. *Proceedings of the Royal Society of London. Series A, Mathematical and Physical Sciences, 151*(873), 421-444.

Tinney, C., & Ukeiley, L. (2009). A study of a 3-D double backward-facing step. *Experiments in Fluids, 47*(3), 427-438.

Toschi, F., Amati, G., Succi, S., Benzi, R., & Piva, R. (1999). Intermittency and Structure Functions in Channel Flow Turbulence. *Physical Review Letters, 82*(25), 5044-5047.

Tsuji, Y. (2003). Large-scale anisotropy effect on small-scale statistics over rough wall turbulent boundary layers. *Physics of Fluids, 15*(12), 3816-3828. doi: 10.1063/1.1622395

Walters, D., Bhushan, S., Alam, M., & Thompson, D. (2013). Investigation of a Dynamic Hybrid RANS/LES Modelling Methodology for Finite-Volume CFD Simulations. *Flow, turbulence and combustion, 91*(3), 643-667.

Yakhot, V. (2001). Mean-field approximation and a small parameter in turbulence theory. *Physical Review E, 63*(2), 026307.

Yakhot, V. (2006). Probability densities in strong turbulence. *Physica D: Nonlinear Phenomena, 215*(2), 166-174. doi: http://dx.doi.org/10.1016/j.physd.2006.01.012

Yakhot, V. (2008). Dissipation-scale fluctuations and mixing transition in turbulent flows. *Journal of Fluid Mechanics, 606*(1), 325-337.

Yakhot, V., & Sreenivasan, K. R. (2005). Anomalous Scaling of Structure Functions and Dynamic Constraints on Turbulence Simulations. *Journal of Statistical Physics, 121*(5-6), 823-841. doi: 10.1007/s10955-005-8666-6

Zagarola, M. V., & Smits, A. J. (1998). Mean-flow scaling of turbulent pipe flow. *Journal of Fluid Mechanics, 373*(1), 33-79.

Zhou, Q., & Xia, K.-Q. (2010). Universality of Local Dissipation Scales in Buoyancy-Driven Turbulence. *Physical Review Letters, 104*(12), 7-10. doi: 10.1103/PhysRevLett.104.124301

Zhou, T., & Antonia, R. A. (2000). Reynolds number dependence of the small-scale structure of grid turbulence. *Journal of Fluid Mechanics, 406*, 81-107.